EPFL

Thèse n° 8212

‘Green’ Cr(III)-based electrodeposition of stainless steel-like FeCrNi: synthesis, mechanisms, material properties of films and micro-nanocomponents for bio-medical applications

Présentée le 10 juillet 2020

à la Faculté des sciences et techniques de l’ingénieur
Groupe SCI STI SM
Programme doctoral en science et génie des matériaux

pour l’obtention du grade de Docteur ès Sciences

par

Enrico BERTERO

Acceptée sur proposition du jury

Prof. P. Hoffmann, président du jury
Dr S. Mischler, Dr L. V. S. Philippe, directeurs de thèse
Dr P. Schmutz, rapporteur
Prof. H. Terryn, rapporteur
Prof. R. Spolenak, rapporteur

École
polytechnique
fédérale
de Lausanne

2020

Acknowledgements

First of all, I would like to thank my Ph.D. supervisors Laetitia Philippe and Stefano Mischler for allowing me to learn and work in their laboratories, and for their precious help. I am grateful to Johann Michler, who gave me the opportunity to join his laboratory. I would also like to thank the members of my Ph.D. jury: Prof. Ralph Spolenak, Dr. Patrik Schmutz, Prof. Terryn Herman and Prof. Patrik Hoffmann.

All the work done during this Ph.D. would have not been possible without the input from many people I have met along my doctoral studies, especially I am grateful to all authors who contributed on the articles we have published and the ones yet to come. I want to immensely thank all my current/former colleagues from Empa Thun, in particular: Madoka who taught me a great deal about electrochemistry and Cristina for her unfailing support, organisation skills and friendship, Patrik, Petai, Maxime and the rest of the electrochemistry group. As well, Laszlo, Carlos, Xavier, Luisa, Jakub, Nicolò, Daniele, Tatiana, Cinzia, Nadia, Jérémie, Thomas, Barbara, Krzysztof, Caroline, Raj, Manish, Emese, Kevin, James, Johannes, Cédric, Mikhail, Mikko, Gerhard, the amazing secretaries (Eveline and Katrin), the rest of Empa staff and all the Ph.D./Master students and guest researchers I cannot mention all here. I am deeply grateful to all of them for their positive attitude, their resourceful help, their way to make you feel home, their making every moment enjoyable, and lastly for their sincere friendship.

Additionally I want to thank my Horizon 2020 ITN network (SELECTA), in particular Eva Pellicer and Jordi Sort (UAB Barcelona), Henrikas Cesiulis and Natalia Tsyntsaru (Vilnius University). I am also grateful to all the people from my EPFL group in Lausanne, in particular Anna Igual for her precious support.

Finally, I want to say a big 'grazie' to everyone supporting me from Italy: my best friends (Daniele, Lorenzo, Andrea, Marika), close friends and relatives, and most importantly my unique family (my parents Anna and Arturo, my sister family Elisa, Silvio and Alice, my brother family Roberto and Martina) for their endless encouragements, constant support and trust. I cannot say thank you enough.

Even though some things could have been done differently, I would not change a moment of this journey: the people I encountered, the work environment, the research, everything I have experienced. I am extremely grateful to have been part of all this.

Thank you! Merci! Grazie!

Bern, June 2020 E. B.

Abstract

The electrodeposition (ED) of stainless steel (SS) -like FeCrNi alloys for miniaturised devices is appealing for bio-medicine as it would allow combining excellent material properties (*e.g.* corrosion resistance, hardness, bio-compatibility) at low-cost.
However, conventional baths often contain hazardous Cr(VI). Alloys ED from environmentally friendly Cr(III) electrolytes is crucial for facilitating the transition towards sustainable and ecological production. Still, this process was not comprehensively studied. ED from Cr(III)-based aqueous electrolytes leads to impurities incorporated in films, hydrogen evolution reaction (HER) and side-effects. The role of both electrolyte composition, containing organic additives (*e.g.* glycine), and deposition parameters on material properties was not clear. Moreover, passing from films to micro-nanocomponents (M-NEMS) *via* ED was not properly investigated when dealing with more complex Cr(III)-based alloys.
The aim of this thesis has been to study the ED of FeCrNi coatings and M-NEMS using a 'green' Cr(III)-glycine electrolyte, understanding better the relations between ED mechanisms, deposition parameters and material properties, as well as their variation due to miniaturisation.
Novel information was attained for all-aqueous electrolytes by investigating: films microstructure evolution (amorphous-nanocrystalline) in correlation to their composition and elemental 3D distribution, influence of Cr(III)-glycine in terms of coatings at%, together with a thorough analysis on metals speciation/complexation in the baths. These results allowed to propose various Cr(III)-based ED mechanisms.
The material properties of the as-deposited films were evaluated in dependence of morphology and composition variations, then compared to the standard metallurgical ones. FeCrNi electrodeposits showed good passivation and bio-compatibility comparable to AISI SS, and tuneable soft-magnetism. However, tribological tests revealed that the material was hard but brittle. The main issues were correlated to HER leading to low deposition efficiency, material brittleness and porosity.
To overcome these issues, a mixed-solvent electrolyte composed of ethylene glycol (EG) has been investigated and compared to the all-aqueous one, showing similar Cr(III)-glycine complexation, but higher deposition efficiency (decrease in HER). EG-based electrolyte was found to be an effective solution for obtaining FeCrNi M-NEMS *via* template assisted ED. Nanotubes (NTs) and nanowires (NWs) have been achieved *via* ED into AAO templates: high currents resulted in

NTs, whereas low ones in compact NWs. Micro-pillars have been created *via* ED into UV-LIGA moulds, combining EG-based electrolyte and a CV-like deposition, avoiding moulds delamination caused by HER and under-deposition.
A comparison of the material properties was pursued for FeCrNi electrodeposits as-deposited (amorphous) and annealed (nanocrystalline) for both studied electrolytes. This investigation correlated electrolyte type, material composition/microstructure/morphology, *vs.* other material properties *i.e.* corrosion resistance, bio-compatibility, magnetic and mechanical properties.
In conclusion, this research studied in depth Cr(III)-based ED, achieving improvements and giving useful guidelines for applying this process for creating SS-like coatings and M-NEMS for advanced bio-medical applications.

Key words: 'green' Cr(III) electrolyte, FeCrNi alloy, electrodeposition, deposition mechanisms, material properties, miniaturisation, bio-medical applications

Abstract

L'elettrodeposizione (ED) di leghe FeCrNi simili all'acciaio inox (SS) sono interessanti per ottenere dispositivi miniaturizzati nell'ambito bio-medicale in quanto combinerebbero eccellenti proprietà (*e.g.* anti-corrosione, durezza e bio-compatibilità) a basso costo.
Tuttavia, elettroliti tradizionali fanno uso di Cr(VI) che è tossico. L'ED a partire da un elettrolita non dannoso contenente Cr(III) è un'alternativa ecologica e fondamentale per facilitare la transizione verso produzioni verdi e sostenibili. Eppure questo processo richiede uno studio approfondito, che ad oggi manca. L'ED da soluzioni Cr(III) acquose comporta: impurità incorporate nei film, reazione d'evoluzione d'idrogeno (HER) ed effetti secondari.
Il ruolo della composizione dell'elettrolita (contenente additivi come la glicina) e dei parametri di ED in funzione delle proprietà del materiale non erano chiare. Inoltre, il passaggio da film a micro-nanocomponenti (M-NEMS) *via* ED non è stato propriamente investigato, soprattutto nello studio di leghe complesse a base Cr(III).
Lo scopo di questa tesi è stato di studiare l'ED di FeCrNi film e M-NEMS usando un elettrolita ecologico a base Cr(III)-glicina, approfondendo le relazioni tra meccanismi di ED, parametri di ED e proprietà del materiale, ed anche le loro variazioni legate alla miniaturizzazione. Nuove informazioni sono state ottenute per elettroliti acquosi analizzando: evoluzione della microstruttura di film (da amorfo a nanocristallino) in relazione alla loro composizione e distribuzione degli elementi, influenza di Cr(III)-glicina rispetto a composizione di film, analisi completa delle reazioni di speciazione/complessazione negli elettroliti. Questo ha permesso di proporre dei meccanismi sull'ED a base Cr(III). Le proprietà del deposito sono state valutate in funzione di variazioni morfologiche/microstrutturali, poi comparate con referenze metallurgiche. Film di FeCrNi hanno mostrato ottime proprietà di passivazione e di bio-compatibilità simili ad AISI SS, e soft-magnetismo. Tuttavia, test tribologici hanno rivelato un materiale duro ma fragile. I principali problemi erano correlati con HER, quindi bassa efficienza di ED, fragilità e porosità del materiale. Per ovviare a queste difficoltà, un elettrolita a solvente misto acqua e glicole etilenico (EG) è stato investigato e confrontato con il caso solo-acqua, mostrando simili complessazioni Cr(III)-glicina, ma efficienza maggiore (diminuzione di HER). L'elettrolita a base EG è stato identificato come valida alternativa per ottenere FeCrNi M-NEMS *via* ED assistita dentro forme. Nanotubi (NT) e nanofili (NW) sono stati ottenuti tramite ED dentro modelli AAO, invece micro-pilastri dentro forme UV-LIGA, combinando l'elettrolita a

base EG ad una deposizione ciclica, permettendo di evitare la delaminazione delle forme causata da HER. Il raffronto delle proprietà del materiale è stato attuato per film depositati (amorfi) e poi temprati (nanocristallini) ottenuti da entrambi gli elettroliti. Questa investigazione ha correlato: tipo di elettrolita e composizione/microstruttura/morfologia dei depositi, rispetto ad altre caratteristiche *i.e.* anti-corrosione, bio-compatibilità, proprietà magnetiche e meccaniche. In conclusione, questa ricerca ha permesso di studiare a fondo l'ED a base Cr(III)-glicina, ottenendo miglioramenti e dando elucidazioni su come ottenere film e M-NEMS tipo SS per applicazioni nell'ambito bio-medicale.

Parole chiave: elettrolita a base Cr(III), leghe FeCrNi, elettrodeposizione, mecchanismi di deposizione, proprietà del materiale, miniaturizzazione, applicazioni bio-medicali

Contents

List of Figures

List of Tables

Nomenclature

O_x oxidised species during RedOx process

R_{ed} reduced species during RedOx process

n number of exchanged electrons during RedOx process

E^0 electrode potential (V vs. SHE)

E_{rev} reversible potential (V vs. SHE)

a activity of electroactive species (-)

R universal gas constant (8.3145 J mol^{-1} K^{-1})

ΔG Gibbs free energy (J mol^{-1})

F Faraday's constant (96485.3 C mol^{-1})

η overpotential (V vs. SHE)

i_0 exchange current density (A cm^{-2})

α transfer coefficient (-)

β_c, β_a Tafel coefficients (-)

i_L limiting current density (A cm^{-2})

D diffusion coefficient of species at the electrode surface (cm^2 s^{-1})

c_b concentration of species in the bulk (mol cm^{-3})

c_0 concentration of species at the electrode surface (mol cm^{-3})

δ Nernst diffusion layer thickness (µm)

M molar mass (g mol^{-1})

ν kinematic viscosity (cm^2 s^{-1})

ω angular rotation rate of the RDE (rad s^{-1})

i_K kinematic controlled current density (A cm^{-2})

ρ density (g cm^{-3})

M_S saturation magnetisation (emu cm^{-3})

F_N normal load (mN)

R_a mean roughness (nm)

μ friction coefficient (-)

ν Poisson ratio (-)

I ionic strength (M)

List of Abbreviations

SS stainless steel

HER hydrogen evolution reaction

AISI American Iron and Steel Institute

Cr(VI) hexavalent chromium ion

Cr(III) trivalent chromium ion

EU European Union

LIGA Lithographie, Galvanoformung, Abformung (Lithography, Electroplating, Moulding)

AAO anodic aluminium oxide

redox reduction and oxidation

EDL electric double layer

IHP inner Helmholtz plane

OHP outer Helmholtz plane

RE reference electrode

WE working electrode

CE counter electrode

SHE standard hydrogen electrode

E^0 standard electrode potential

List of abbreviations

OCP open-circuit potential

SR scan rate

AR aspect ratio

AAD active area density

PP pulse plating

PRP pulse reverse plating

NW nanowire

NT nanotube

CNT carbon nanotube

RPM revolutions per minute

PGMEA propylene glycol methyl ether acetate

RDE rotating disk electrode

LSV linear sweep voltammetry

RTA rapid thermal annealing

SEM scanning electron microscopy

XRD X-ray diffraction

XRF X-ray fluorescence

XPS X-ray photoelectron spectroscopy

EDX energy dispersive X-ray

ERDA elastic recoil detection analysis

APT atom probe tomography

VSM vibrating sample magnetometer

DI water deionised water

EG ethylene glycol

FWHM full width half maximum

BE binding energy

R.S.F. relative sensitivity factor

C.E. current efficiency

PCD primary current distribution

DMEM Dulbecco's Modified Eagle Medium

LDH lactate dehydrogenase

Introduction

The success and widespread use of stainless steel (SS) stems from its combination of excellent properties: corrosion and wear resistances, hardness and strength. For these reasons, stainless steel alloys are one of the most exploited materials in a vast range of applications, from building to food processing and medical sectors [1]. There are hundreds of types/grades of SS which differ among each other for the various elements contained and their crystalline structure, which leads to diversified properties. The common denominator among all SS is the presence of iron as a major component and at least 10.5 wt% of chromium. Indeed, chromium is the key element allowing steel to form a thin passivation layer which endows the material with a high corrosion resistance. Austenitic AISI 304 (18Cr-10Ni) and AISI 316L are conventionally used stainless steels, often employed in biological and medical sectors for their low carbon content and superior bio-compatibility [2, 3]. In such alloys the iron austenitic crystalline phase is induced by the presence of nickel, making the material less brittle and also magneto-resistive for a wide range of temperatures.

The conventional method of producing stainless steel at large scales is from ore, through melting and casting. This process requires plants with high energy and maintenance costs. In contrast to large scale production, small scale and miniaturised SS components are nowadays in growing demand, because of the material's afore-mentioned advantageous properties, which can be applied to various fields such as micro-robotics, bio-medical, watch-making, etc. For these applications, many micro- nanofabrication techniques can be exploited, namely 3D printing using metal powder [4], laser ablation [5] and micro-powder injection moulding [6]. However, these processes are demanding in terms of running costs, lacking in precision and having very slow process times.

Electrodeposition is a well-known and established technique, which has mainly been employed for producing protective/decorative (*i.e.* anti-corrosion, wear resistant) coatings [7, 8]. In recent years, the interest for such processes has increased and shifted towards functional (*i.e.* hydrophobic, antifouling, self-cleaning) films [9,10] and micro- nanocomponents [11], because of this method's cost effectiveness and versatility.

Many metals/alloys can be grown by electrodeposition method, giving different properties depending mainly on film composition and microstructure. Hard-

chromium has been a common choice for obtaining hard coatings with optimal wear and corrosion resistances [12]. However, Cr(VI) (hexavalent chromium), which is commonly used in industry for the electrodeposition of chromium-based films (*e.g.* chrome plating) is highly carcinogenic and will soon be prohibited by many countries worldwide, in particular by EU [13]. Alternative electrodeposited films can be NiP, NiW, CoP or CoW, in which magnetic, corrosion and mechanical characteristics are mainly dictated by the amount of alloying elements present inside the deposits [14, 15].
However, none of the mentioned alloys meet the requirements for bio-medical applications. For these applications, good corrosion and wear resistance are necessary, but bio-compatibility is a must requirement. The metals which are employable in a biological environment are very few: Pd, Pt, Au, Ti, Mg, Zn, CrCo alloys and AISI 304/316L stainless steels [3]. Moreover, their use is often limited to specific purposes, and many of them are precious materials, expensive and difficult or even impossible to obtain through electrodeposition. Among them, stainless steel stands out for its overall good qualities, which have made it one of the most extensively used materials in the bio-medical field, and also because of the ability to deposit it by electroplating (*e.g.* as Fe-Cr-Ni alloy). Importantly, electrodeposition of stainless steel has proven possible from Cr(III) solutions. Cr(III) (trivalent chromium) is a 'green' alternative to Cr(VI), which is getting more and more attention in the electrochemistry sector.

The use of SS for creating micro- nanocomponents could be beneficial for obtaining outstanding bio-medical devices, such as micro-needles and drug-delivery components. For this purpose, electrodeposition can be combined with micro-nanomoulds obtained by lithographic routes or with nanotemplates, *e.g.* anodic aluminium oxide (AAO) nanoporous templates. The progress achieved in the last decades in lithographic technology [16], makes now feasible creating micro- nanomoulds with high-aspect ratios (*i.e.* LIGA) and sub-micron resolution features (*i.e.* two-photon lithography). Therefore, electroplating SS-like alloys inside 2D/3D miniaturised moulds/templates paves the way towards an economically viable, flexible and scalable method for achieving miniaturised advanced objects, suitable in the afore-mentioned contexts.

Thesis structure

Chapter 1 gathers the fundamentals of electrodeposition, a critical review of the most recent developments in the field of electrodeposition of FeCrNi -based alloys from trivalent chromium electrolytes, and the state-of-the-art in miniaturisation of stainless steel with a focus on electrochemistry routes. Afterwards, the scientific questions (*Statement of the problem*) and the thesis objectives (*Research objectives*) are highlighted. Chapter 2 is dedicated to the materials, the characterisation techniques and the set-up utilised during this thesis research. The following four chapters cover the results derived from the investigation on FeCrNi electrodeposition from a 'green' Cr(III)-based electrolyte. The understanding of the mechanisms involved in such complex process and how they are linked to composition, morphology and microstructure can be found in Chapter 3, which is followed by an analysis of the main material properties of coatings obtained from a pure aqueous electrolyte (Chapter 4). Then, improvement of the electrodeposition process have been further investigated by comparing aqueous and mixed-solvent electrolytes in order to be able to obtain miniaturised components (Chapter 5). Additional characterisations have been performed retrieving further knowledge of the material properties when using a mixed-solvent electrolyte (Chapter 6). Insights obtained through this study have become key factors for the production of FeCrNi using 'green' Cr(III)-based electrolytes, with applications in the field of bio-medical MEMS/NEMS.

1 Literature review

1.1 Fundamentals of electrodeposition

Electrodeposition is a well-known fabrication technique, which allows to grow a material (most often of metallic nature) on a conductive surface based on the redox (reduction and oxidation) concept. A potential (or current) needs to be applied between two conductive surfaces (called electrodes) immersed in an ionically conductive solution (named electrolyte). The electrolyte can be aqueous, organic, mixed or molten-salt -based. In this chapter, only aqueous -based solutions are considered. In the so-called cathodic electrodeposition, the metal ions (M^{z+}) present in the electrolyte are discharged *via* reduction process to form a deposit on the cathode and this can be represented by the following reduction equation

$$M^{z+}_{electrolyte} + ze^{-} \rightarrow M_{electrode} \tag{1.1}$$

Equation 1.1 is at the core of the electrodeposition process and entails various aspects: (1) metal-solution interface, (2) kinetics and (3) nucleation and growth. In this chapter, the fundamentals of these important aspects are outlined.

1.1.1 Metal-solution interface

As implicitly stated above, in order to perform electrodeposition, it is necessary to have an electrochemical cell which primary constituents are an electrolyte, two conductive electrodes and a power supply.

Regarding the electrolytes, the two main ingredients are the solvent (*e.g.* water molecules) and the solute (*e.g.* salts), which together yield a conductive ionic solution. A typical example of solute are salts, which are solid ionic compounds composed of positive and negative ions linked together by ionic bonds. Their dissolution (complete dissociation into positive and negative ions) in an aqueous medium depends on the solubility of such compounds in the solvent, which is related to solute/solvent concentration, pH-temperature of the solvent and pressure. Typically, metallic ions in solution (dissociated from metal salts) form metal complexes, which consist of a central metal ion bonded (*i.e.* covalent bond) to some surrounding molecules or ions (called ligands). These metal complexes can be overall charged. Another source of ions in solution are acids, which dissolution in the medium can be explained as a proton transfer reaction

(Brønsted–Lowry theory)

$$HA + B \rightleftharpoons A^- + HB^+ \tag{1.2}$$

In an acid-base reaction, the acid HA can deprotonate (lose a proton) becoming its conjugate base A^- and the base B can protonate (gain a proton) becoming its conjugate acid HB^+. Although water molecules are neutral (no overall charge), their uneven electron distribution makes them slightly polar, making water the perfect solvent for the creation of electrolytes[1].

In fact, inside pure water, charged molecules (*i.e.* ions from salts or acids, metal complexes) become completely surrounded by water molecules (hydration or solvation process). These surrounding water molecules are dipoles, which electrostatically orient themselves depending on the charge of the closest ion, forming an overall neutral shell, screening the inner ion from possible ion-ion interactions (Ion-Dipole model).

Electrodes are electrically conductive materials, typically a metal or an alloy.

When a metal is immersed in a solution containing its corresponding metal ions, excess of opposite charges are accumulated at the metal surface and in the solution (electrons at the electrode surface and metal cations from the solution next to it), forming a polarised metal-solution interface (with a charge concentration gradient), which is called electric double layer (EDL). Different theories have been developed to describe the EDL and the corresponding potential variation, in order of time: Helmholtz compact double-layer, Gouy-Chapman diffuse-charge, Stern, and Graham triple-layer models [17]. Graham triple-layer model seems the most valid matching theory with experimental findings. The basic idea behind this theory is that when the cation is attracted to the interface becomes dehydrated and thus can get closer to the electrode surface. Therefore, there are three different layers depending on the distance from the electrode into the electrolyte. At a distance x_1, called inner Helmholtz plane (IHP), partially or fully dehydrated adsorbed ions are present. Instead, fully hydrated ions cannot approach closer than a distance x_2 from the electrode, called outer Helmholtz plane (OHP). Afterwards, there is the diffuse double layer in which hydrated ions are becoming attracted towards the electrode due to the potential difference. Such behaviour is schematically depicted in Figure 1.1.

Electrode potential and thermodynamics

The dynamic equilibrium undergoing in the EDL between the electrode metal ($M_{electrode}$) and its corresponding ions in solution ($M^{z+}_{electrolyte}$), through electrons

[1] In pure water, also H_2O dissociates into H^+ and OH^- in very small concentrations ($1.0 \cdot 10^{-14}$ mol L^{-1} at 25 °C). The amount of H^+ (or OH^-) in a solution define how acidic (or basic) is the medium, which is measured using the pH scale (logarithmic and inversely related to H^+ concentration).

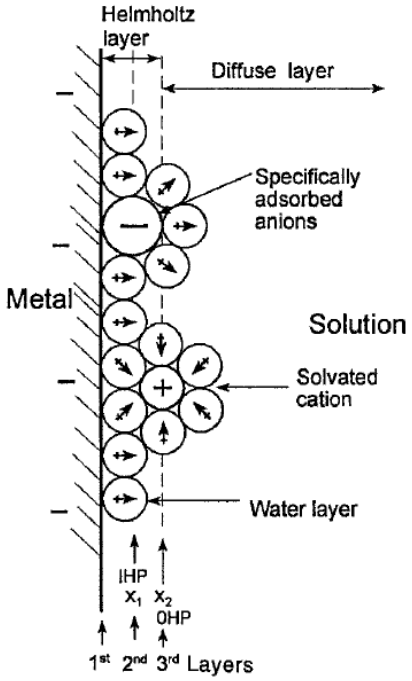

Figure 1.1 – Schematic of the electric double layer in Grahame triple-layer model[2], in which circles with arrows represent water dipoles (+ is the positive end).

exchange, can be described by the equilibrium reaction

$$M^{z+}_{electrolyte} + ze^- \rightleftharpoons M_{electrode} \tag{1.3}$$

Equilibrium is reached when the number of ions being adsorbed and reacted (reaction from left to right: Reduction) equals the number of ions leaving the surface (reaction from right to left: Oxidation).

The potential of such layer (electrode potential) cannot be measured directly. Another electrode, which will also have an EDL, needs to be employed as a reference. Therefore, only the potential difference between the two electrodes can be assessed. Such additional electrode is called reference electrode (RE) and together with the first one, a simple two-electrodes electrochemical cell is formed. ED metal potentials in literature are typically listed as reduction potentials with respect to the standard hydrogen electrode (SHE) used as RE, which is assumed to have zero potential. These reduction potentials are called standard electrode potentials (E^0) because they are measured at standard conditions (*i.e.* metals' activity to unity, pressure 1 atm and typically temperature at 25 °C).

If considering the following reduction/oxidation (RedOx) equilibrium reaction for

[2] adapted from Ref. [17]

a generic electrode (half-cell reaction)

$$O_x + ne^- \rightleftharpoons R_{ed} \tag{1.4}$$

where O_x is the oxidised species, R_{ed} is the reduced species and n is the number of exchanged electrons between O_x and R_{ed}. Then, the dependence of potential on the concentration of species is expressed by the Nernst equation

$$E = E^0 + \frac{RT}{nF} ln \frac{a(O)}{a(R)} \tag{1.5}$$

Here a is the activity of electroactive species (proportional to the species' concentration), R is the universal gas constant (8.3145 J mol^{-1} K^{-1}), T is the temperature (K) and E is the equilibrium potential or open-circuit potential (OCP) or reversible potential (E_{rev}) and it is measured between the electrode and the RE (*e.g.* SHE) when no net current is flowing (equilibrium). The Nernst equation is valid only for a reversible system (*i.e.* a system thermodynamically at equilibrium, with no net preferential reactions). If both the product and the reactant in a reaction at one electrode have unit activity, then the reduction potential becomes the standard electrode potential E^0. Typically, E_{rev} is plotted against pH for a half-cell reaction (Pourbaix diagram) showing the different oxidation states involved. Moreover, such reversible potential is related to the Gibbs free energy ΔG (J mol^{-1}) with the following relation

$$\Delta G = -nFE \tag{1.6}$$

where F is the Faraday's constant (96485.3 C mol^{-1}) and ΔG denotes if the reduction reaction is spontaneous (*i.e.* $\Delta G < 0$ which correspond to $E > 0$) or non-spontaneous and therefore, it needs an external energy source to be activated (*i.e.* $\Delta G > 0$ which correspond to $E < 0$).

1.1.2 Kinetics and fundamental equations

In order to separate reduction and oxidation from the same electrode, another electrode needs to be used in the electrochemical cell. The cathode is the working electrode (WE), where the main reactions take place (*e.g.* reduction of metal cations). Instead, the anode is the counter electrode (CE), which is a non-polarisable conductive material, meant to electrically close the cell formed by cathode and anode, therefore to balance the overall redox process (*e.g.* provided by oxidation of water molecules). The cell potential (full-cell reaction) is defined as the difference between the reduction potentials of cathode and anode and is expressed with the following convention

$$E_{cell} = E_{cathode} - E_{anode} \tag{1.7}$$

In this case, we are in a condition of non-equilibrium (flow of current between electrodes). Therefore, each electrode potential differs from its corresponding equilibrium one. This difference is called overpotential η (V *vs.* SHE) and is defined as

$$\eta = E(I) - E_{rev} \tag{1.8}$$

where $E(I)$ is the potential at the WE resulting in a net current I flowing through it towards the CE.
The overpotential is the potential needed to be overcome in order to have a non-spontaneous cell reaction occurring. It dictates the type of polarisation happening in the EDL at the electrode/electrolyte interface, consequently it determines the different electrode kinetics. There are four partial reactions/overpotentials/kinetics defining the rate control regime: charge transfer, diffusion, chemical reaction and crystallisation.

In case of small overpotentials close to the equilibrium potential ($|\eta|$ < 100 mV), the relation between current and overpotential follows a linear trend.
When the overpotential is larger ($|\eta| \geq$ 100 mV), the current depends exponentially on the overpotential and their relation is described by the Volmer-Butler equation. The total current density i [A cm^{-2}] is the sum of cathodic and anodic partial currents at the electrode

$$i = i_c + i_a \tag{1.9}$$

and the Volmer-Butler equations for cathodic and anodic processes are

$$i_c = -i_0 e^{\left(-\frac{\eta}{\beta_c}\right)} \tag{1.10a}$$

$$i_a = i_0 e^{\left(\frac{\eta}{\beta_a}\right)} \tag{1.10b}$$

i_0 is the exchange current density, which can be thought as the net electrode current at equilibrium, which means when η = 0, thus the partial currents balance each other (i_c = i_a) and consequently i = i_0. Typically this parameter can be derived graphically (Tafel experiment), by scanning 100/200 mV close to the reversible potential in both positive and negative directions, plotting the logarithmic current versus the potential, fitting the curve linearly from both sides of E_{rev} and then taking their intersection as i_0. α is the transfer coefficient, β_c and β_a are called Tafel coefficients and are defined as

$$\beta_c = \frac{RT}{\alpha n F} \tag{1.11a}$$

$$\beta_a = \frac{RT}{(1-\alpha)\, nF} \tag{1.11b}$$

Volmer-Butler equations (1.10) are only valid when charge-transfer is the rate-determining (slow) process. This current-overpotential range is called charge-transfer limited region (activation polarisation).

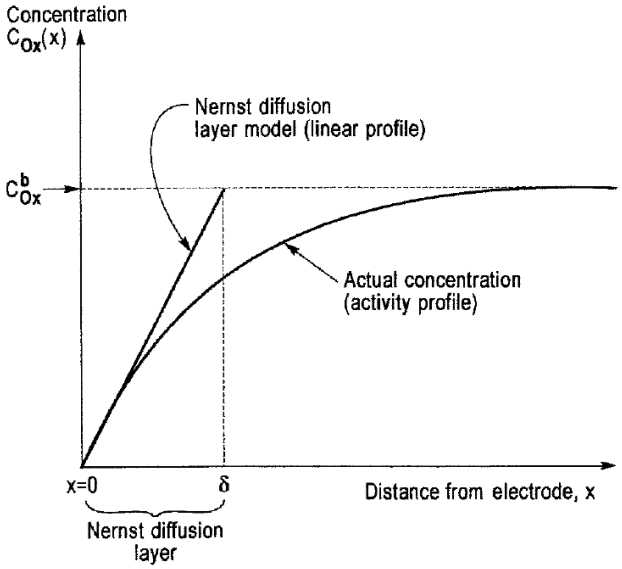

Figure 1.2 – Concentration variation of the reactant species in case of non-equilibrium condition in diffusion limited region, with x the distance from the electrode surface towards the bulk electrolyte[3].

For even larger overpotentials, the transport of charges from the bulk of the electrolyte to the electrode surface becomes the limiting factor in the current-potential relationship. In such case, the current reaches a limit i_L (limiting current density), which can be derived by Fick's first law. In the simplest case, in which transport of charges is only considered by diffusion, the limiting current density is given by

$$i_L = \frac{nFD}{\delta} c_b \tag{1.12}$$

where D (cm^2 s^{-1}) is the diffusion coefficient of the reducible species at the electrode surface, c_b (mol cm^{-3}) is the concentration of species in the bulk solution and δ (cm) is the Nernst diffusion layer thickness. The diffusion layer thickness is defined by the Nernst diffusion model (Figure 1.2), which assume that at limiting current conditions, the concentration of reactant species is null at the surface of the electrode and increases linearly reaching again the bulk concentration c_b at the diffusion distance δ. In this case, the current-overpotential region is said to be diffusion limited (concentration polarisation).
The four regions describing the kinetics, in terms of current *vs* overpotential, of a

[3] adapted from Ref. [17]

polarised electrode are depicted in Figure 1.3.

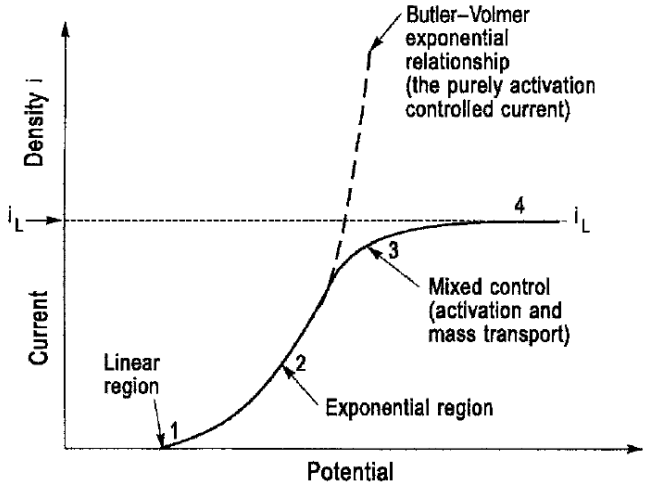

Figure 1.3 – Current-overpotential relation for a polarised electrode showing the different kinetics regions[4].

Faraday's law and current efficiency

The total charge Q (C) passing through an electrochemical cell is proportional to the amount of electrochemical reaction occurring at the electrode, according to Faraday's law

$$w = \left(\frac{Q}{F}\right)\left(\frac{M}{n_{mol}}\right) \tag{1.13}$$

where w [g] is the weight of the product in the reaction, M (g/mol) is the molar mass, n_{mol} is the number of displaced electrons per mole of product and F is Faraday constant. Since Q is defined as the product of current I (A) and time t (s)

$$Q = It \tag{1.14}$$

and $\frac{M}{n_{mol}}$ ratio can be rewritten in terms of equivalent weight w_{eq}

$$w_{eq} = \frac{A_{wt}}{n} \tag{1.15}$$

which is the ratio between atomic weight A_{wt} and the number of electrons involved in the reaction n. Then, equation (1.13) becomes

$$w = \left(\frac{It}{F}\right)\left(\frac{A_{wt}}{n}\right) \tag{1.16}$$

[4] adapted from Ref. [17]

If more reactions take place at the electrode, then it is possible to calculate the current efficiency (C.E.) of one particular reaction j either in terms of required charge for that reaction Q_j or from the weight of product for reaction j, which is w_j. The expression is then the following

$$C.E. = \frac{Q_j}{Q_{tot}} = \frac{w_j}{w_{tot}} \tag{1.17}$$

where Q_{tot} is the total passed charge and w_{tot} is the total weight, *i.e.* the weight when all the current would have been used for reaction j.

Cottrell equation

The Cottrell equation predicts the variation of current in time when a potential step is applied

$$i(t) = \frac{nFAc_b\sqrt{D}}{\sqrt{\pi t}} \tag{1.18}$$

where D is the diffusion coefficient of the analysed reducible species, A (cm^2) is the area of the electrode and c_b is the bulk concentration of the considered analyte electroactive species. This equation is only valid when in the studied electrochemical system the current is limited by diffusion, *i.e.* large overpotentials and unstirred solution are necessary requirements. Potential step methods, such as chronoamperometry, are typically used to determine the diffusion coefficient by applying Cottrell equation.

Rotating disk electrode (RDE) and Koutecký-Levich equation

Performing linear sweep voltammetry scans using a RDE set-up at different rotation speeds allows to obtain a precise solution flow at the electrode surface, resulting in a well-defined Nernst diffusion layer when the potential is in the diffusion limited region

$$\delta = 1.61\nu^{0.166}D^{0.33}\omega^{0.5} \tag{1.19}$$

where δ (cm) is the diffusion layer thickness, ν ($cm^2\ s^{-1}$) is the kinematic viscosity and ω (rad s^{-1}) is the angular rotation rate of the electrode.

In such electrochemical system, reactions at the electrode surface are mass-transport controlled, thus it can be assumed that at the electrode surface the concentration of electroactive species is zero (Nernst diffusion model), therefore, the limiting current is given by

$$i_L = nFD\frac{c_b}{\delta} \tag{1.20}$$

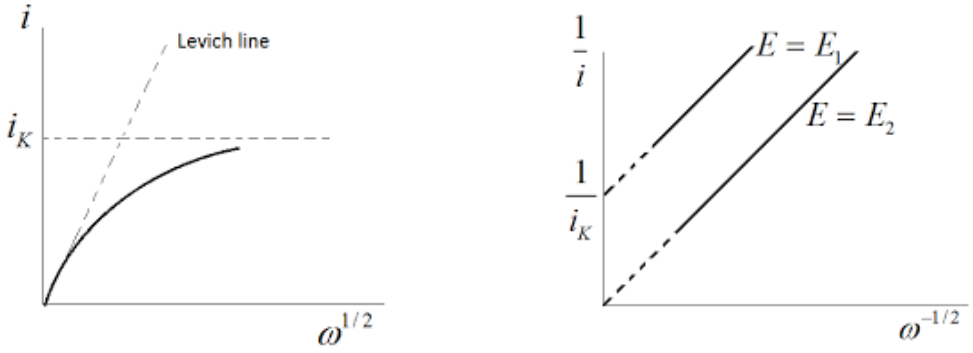

(a) (b)

Figure 1.4 – Koutecký-Levich plots in RDE experiment[5]: (a) current density i *vs.* $\omega^{0.5}$ and (b) $1/i$ *vs.* $\omega^{-0.5}$ for different potentials.

Combining equations (1.19) and (1.20) leads to Levich equation

$$i_L = 0.62nFD^{0.67}\nu^{-0.166}\omega^{0.5}c_b \tag{1.21}$$

which correlates the limiting current density to electrochemical kinetic parameters. For Levich equation, i_L is proportional to $\omega^{0.5}$. For electrochemically reversible systems (fast kinetics/electron transfer), the plot i_L *vs.* $\omega^{0.5}$ is a straight line intersecting the origin.

A deviation from such behaviour (Figure 1.4a) suggests that the system is kinetically limited (slow kinetics, *i.e.* electrochemically irreversible).

For these irreversible systems, the current variation in terms of rotation speed is described by Koutecký-Levich equation

$$\frac{1}{i} = \frac{1}{i_K} + \frac{1}{i_L} \tag{1.22}$$

where i_K is the kinetically controlled current density (for $\omega^{-0.5}$ = 0). This parameter ($1/i_K$) can be obtained graphically by plotting $1/i$ *vs.* $\omega^{-0.5}$ and taking the intercept at $\omega^{-0.5}$ = 0 (Figure 1.4b). Moreover, in the plot i *vs.* $\omega^{0.5}$, the slope of the fitted Levich line (Figure 1.4a) can be applied to Levich equation (1.21) to predict the diffusion coefficient D of the system.

1.1.3 Multistep reactions

In reality, many electrochemical processes proceed *via* a series of complex reactions, *e.g.* complexation of ions and hydrogen evolution reaction (HER) at the cathode.

[5] adapted from https://www.ohio.edu/engineering/ceer/research/upload/RDE-FEIV1.pdf

Electrodeposition from complexed ions
In such case, the metal ion is first chemically reacting with a ligand (or complexing agent) L inside the electrolyte and the new compound is called complexed ion. Then, the electrodeposition process at the cathode is typically associated with first the chemical dissociation reaction of the ligand

$$[ML_x]^{z+} \rightleftharpoons M^{z+} + xL \tag{1.23}$$

then followed by the electroreduction of the active metal ion M^{z+} as in Equation 1.1. Here, independently of the applied potential at electrode, the two rate constants for the chemical reactions 1.23 are defined as k_f (forward or dissociation constant) and k_b (backward or formation constant). Their ratio is the equilibrium or stability constant β, which describe the tendency of the reaction in the electrolyte to proceed more forward or more backward.
In this complexed ion situation, there are three contributions playing an important role in the overall electrodeposition reaction, and therefore each possibly being a rate-determining step. First, the transport (or diffusion) of the complexed species $[ML_x]^{z+}$ towards the electrode interface. Then, the chemical reaction following Equation 1.23. Finally, the transfer of electrons to the electro-active species M^{z+} following the reduction process in Equation 1.1.

Hydrogen evolution reaction (HER)
Concurrent HER at the cathode is a well know side-reaction affecting some electrodeposition systems in which the applied potential need to be rather high in order to have electroreduction of the active metal species (*e.g.* Cr ions). In acidic solution, the overall hydrogen reaction is the following

$$2H_3O^+ + 2e^- \rightarrow 2H_2O + H_2(g) \qquad E^0 = 0.00 \ - 0.059\, pH\ V\ vs.\ SHE \tag{1.24}$$

in which H_3O^+ is the hydrated form of the proton H^+. If considering hydrogen proton diffusion towards the interface and hydrogen gas evolution H_2(g) far from the cathode both as fast processes, then there are two main steps which can become the rate-determining steps in such system. First, charge transfer with formation of adsorbed hydrogen H_{ads}. Second, the combination of adsorbed hydrogen compounds forming H_2 at the cathode surface.

1.1.4 Nucleation and growth

Film formation *via* electrochemical route (electro-crystallisation) have been discussed extensively in literature [18–22]. Nucleation is the starting process for the formation of a monolayer. There are different theories explaining this process, but all have in common the same principles behind. Three main steps can be recognised during the electrodeposition of metals:

1. *Ionic migration*: hydrated metal ions/complexes migrate from the bulk electrolyte towards the cathode due to the potential gradient.

2. *Electron transfer*: these hydrated moieties enter the EDL. Here, they are reduced becoming neutral atoms (adatoms), and subsequently adsorbed at the surface.

3. *Incorporation*: adsorbed atoms diffuse towards the most energetically favourable active sites at the cathode, *i.e.* kinks and steps (Figure 1.5a) and they are incorporated in the material.

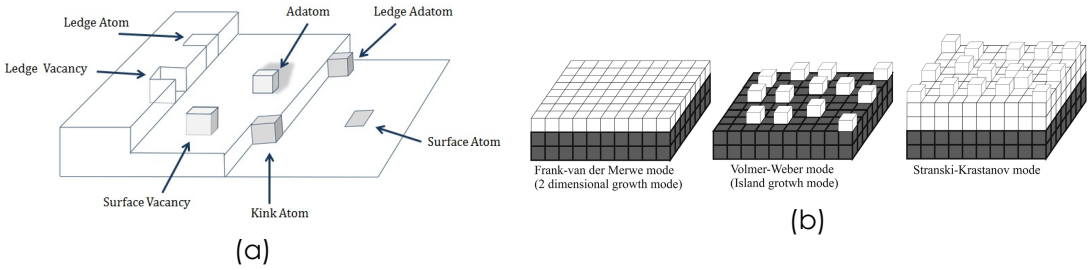

Figure 1.5 – (a) Nucleation schematic during electrodeposition process and (b) different mechanisms of film growth[6].

In addition, there are three main growth mechanisms explaining the formation of a coherent uniform deposit (Figure 1.5b): Volmer-Weber (V-W), Frank-van der Merwe (F-M) and Stranski-Krastanov (S-K). At low current densities (*i.e.* low overpotentials), the nucleation rate is small and nuclei start to grow only at active sites, leading to formation of less numerous nucleation sites (or crystal grains). These grains merge together as they grow in size (nucleation-coalescence process or V-W type), forming a film which is usually polycrystalline and with bigger grain size. Instead, increasing the overpotential typically leads to fast nucleation, which is not only limited to active sites, but it is starting all over the substrate surface. In this way, films with more refined grains are grown (F-M and S-K types).

[6](a) adapted from Ref. [22] and (b) adapted from Ref. [23]

1.1.5 Electrodeposition of alloys and deposition parameters

In general, electrodeposition of more than one metal at a time (codeposition of metals) is sought in order to achieve alloys with superior material properties than the ones obtained with only single metals. Moreover, depending on the composition range of each metal within the alloy, the material properties which can be assessed are different, such as density, hardness, strength, corrosion resistance, magnetic response, etc. In this way, it is clear that the combination of properties achievable by electrodepositing binary, tertiary or even more complex alloys with varying composition is infinite. In addition, in the electrodeposition process, there are some factors or deposition parameters (*e.g.* current density and distribution, temperature, pH, bath agitation) which play an important role in the final coatings characteristics, and they have to be considered and finely tuned in order to obtain optimal results.

Principles of codeposition of metals

Alloys can be electrodeposited by codepositing two or more metals at the same time, which means that the electrolyte has to contain each of the desired metal ions and their deposition potentials have to be close enough to make possible such codeposition. An example of polarisation scans (current density *vs.* applied potential) for the deposition of an alloy are plotted separately for two generic metals A and B in Figure 1.6a. Here, it is possible to observe that at potential V_1 there will be codeposition of metals A and B with a ratio A/B of j_1/j_2.

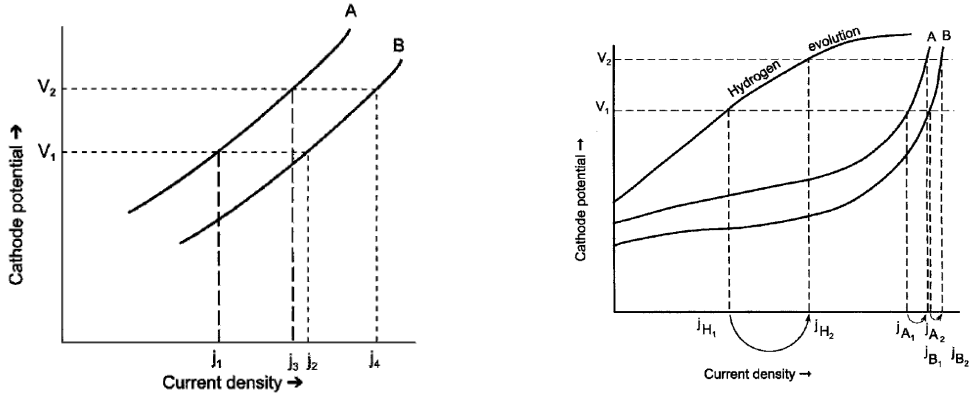

Figure 1.6 – Polarisation scans (current density *vs.* applied potential) of two generic metals A and B in the electrodeposition of an alloy[7]: (a) ideal case and (b) taking into account hydrogen evolution.

However, in principle, many metals cannot be simultaneously electroplated be-

[7] adapted from Ref. [17]

cause of their large differences in deposition potentials. In order to overcome this issue, the only way is to bring together enough the polarisation curves of these metals, by varying the activities (or concentrations) of the species inside the electrolyte. The ionic concentrations of such metals depend strongly on the ligands used to complex the metal ions: different complex ions have different stability constants, therefore different concentration inside the solution. In this way, even if the reversible potentials (E^0) of the metals are far apart, the change in activities due to the use of a different ligand can compensate this potential unbalance, resulting in deposition potentials (E) close to each other. This is valid only in case of no polarised electrodes, *i.e.* reversible system described by equation (1.5). Nevertheless, in practice, systems are irreversible, consequently an overpotential needs to be applied in order to have deposition. The overpotential, which is a measure of the irreversibility of the system, is a key parameter affecting the codeposition of metals. In fact, at lower polarisations, the more noble element will be deposited preferentially. Whereas, at higher polarisations, due to different deposition factors (*e.g.* high current density, low temperature and/or non-agitated solution, which lead to an increase of concentration polarisation), the less noble element will be favoured during plating. Another factor typically present in all electrochemical systems is hydrogen evolution and possibly hydrogen embrittlement, thus porosity. An example of polarisation scans, taking into consideration this side-reaction at the cathode, are depicted in Figure 1.6b. Here, there is little gain in current densities (j_{A2}/j_{A1} and j_{B2}/j_{B1}) passing from voltage V_1 to V_2 for metals A and B, with respect to the hydrogen evolution counterpart (j_{H2}/j_{H1}). At high overpotentials, metals are typically in the diffusion limited region or close by, therefore concurrent HER can become predominant, leading to no effective improvement in metals deposition efficiency.

Deposition parameters

Many factors are influencing the electrodeposition of metals and alloys [14, 17]

- *Current distribution*: *primary current distribution* is related to the transport of charged ions in the electrolyte due to the electric field applied between the electrodes (*i.e.* resistivity of the bath). Here, shape and dimensions of the electrodes are the main parameters dictating the deposition. Edges, corners and protrusions are subjected to higher fields, thus deposition is faster in such conditions. *Throwing power* is the term describing the property of an electrolyte to obtain homogeneous deposits despite the cathode is presenting surface irregularities. Instead, *secondary current distribution* is determined by the polarisation of the cathode, which depends on concentration of species and reactions at the electrode.

- Other main operation parameters are *current density*, *temperature*, *pH*, *bath agitation* and *concentration of electrolyte species*. The current den-

sity is directly linked to the overpotential. Higher current density means higher deposition rate, but also an increase in non-uniformities and in concurrent HER (thus in pH variation). Temperature increase leads to larger deposition rates due to an increase in diffusion and convection, which both augment the concentration of species at the cathode surface. However, this can result in poor surface quality and side-reactions. Instead, remaining at constant pH values is important to maintain the same reactions proceeding at the electrode surface during plating, without incurring in undesired reactions, such as hydrolysis, olation and polymerisation. Bath agitation is mainly affecting the Nernst diffusion layer thickness and therefore, the concentration of ions at the cathode-solution interface. Increase in agitation results in a thinner diffusion layer which means that the concentration at the cathode surface is higher and approaching the bulk one. Lastly, the concentration of ionic species is important to maintain fast electrode reactions and to have low ohmic drop. Moreover, the ionic concentration and type, together with the solvent used, are also affecting the viscosity of the bath and possibly the interactions solvent-solute and solute-solute.

- *Additives* are known to be very efficient for modifying the quality (*i.e.* surface morphology and uniformity) of the deposit [24, 25]. Typically, levellers are employed to decrease the non-uniformities during plating by levelling the current density distribution, whereas brighteners are used for improving the surface aspect of the deposits by grain refinement. Various additives are employed to affect other deposition parameters. Complexing agents are used to modify the ionic activities enhancing the deposition of a metal respect to another one and/or to improve the metals deposition efficiency. Supporting electrolytes are added salts which increase the ionic conductivity. Instead bufferers (such as boric acid [26]) are compounds able to decrease the effect of HER at the cathode surface, maintaining the pH constant. However, the use of additives is rather difficult to understand due to the complex mechanisms involved especially when more additives/metal species are involved, and because of the variety of results which depend on electrolyte composition and ionic species.

1.2 Coatings for bio-medical/micro-robotics applications

For a coating to be applied in the bio-medical and micro-robotics field, the following features should be fulfilled: corrosion and wear resistances, soft-magnetic properties, good mechanical properties (hardness and strength) and biocompatibility. These features can be found in various metals and alloys, depending mainly on the nature of the deposited elements, the coatings' microstructure and possibly on the material architecture.
Microstructure variation by grain size refinement is known to increase the strength in metals following the Hall-Petch relation, which is explained by grain boundaries blocking dislocation motion [27]. However, the increase in strength reaches a maximum for nanocrystalline materials with grain size between 20 to 100 nm (cross-over regime) and decreases again for amorphous films (inverse Hall-Petch), because of grain boundaries mediated mechanisms [28] (Figure 1.7).

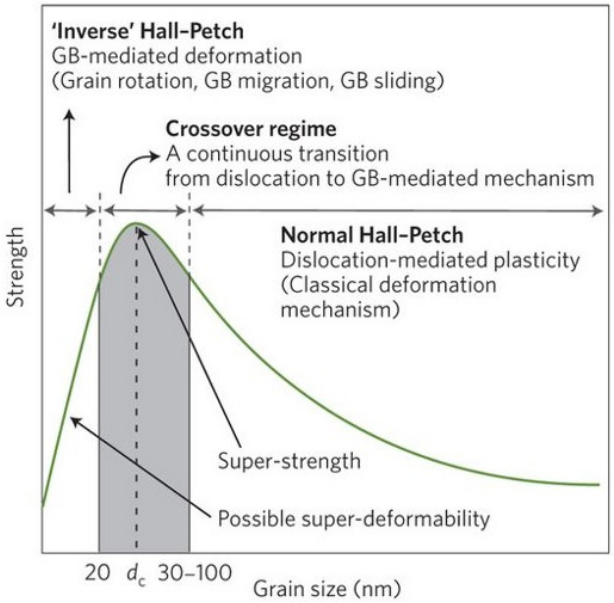

Figure 1.7 – Schematic of a Hall-Petch plot[8], relating material strength and grain size.

Moreover, microstructure plays a role also in corrosion [29]. The classical theory of corrosion states that large grains, which means low grain boundary density, contribute to reach better corrosion resistance in coatings. However, depending on the testing solution, some electrodeposited metals, which are metastable nanocrystalline or amorphous films, have shown to have comparable or even better anti-corrosion behaviour than the large grain counterparts. This fact can be explained from both better uniformity of the passive layer and absence of grain boundaries leading to localised corrosion and pitting [30–33].
Alloying is used to tune various material properties, for example ferro-magnetic

[8] adapted from Ref. [28]

elements (*i.e.* Fe, Co, Ni) show very high saturation magnetisation and coercivity [34], but not enough good mechanical and corrosion resistance features, thus these elements are typically alloyed. In general, the introduction of non-metal elements decreases the magnetic strength, consequently making these materials soft-magnetic. Another case is alloying metals for bio-medical applications. The biocompatibility of a material depends primarily on non-toxicity, corrosion and wear resistances, then also on its application environment, which outline the additional necessary requisites [3]. Such specific characteristics cannot be found in pure metals, therefore alloying is necessary.
Lastly, materials architecture can be classified depending on the design structure: one-dimensional (*i.e.* multilayers), two-dimensional and three-dimensional (*i.e.* composites). In such cases, size effects and interfaces play an important role and lead to enhanced properties respect to standard films [35].

As mentioned beforehand, coatings with some of the sought characteristics can be produced by electroplating. Hexavalent chromium (hard chromium) has been used extensively in industry for final surface finishing because of its very interesting features, which are mainly anti-corrosion and mechanical ones. However, worldwide and specifically in EU the use of such element in metal plating in industry is becoming forbidden, as it is highly toxic (*i.e.* carcinogenic substance) and its waste poses an environmental threat [13]. Similar materials are nickel-based and cobalt-based alloys with phosphorous or tungsten. Ni and Co are known for outstanding mechanical characteristics, P and W alloying elements allow to tune the microstructure and therefore to vary some properties such as corrosion resistance and magnetisation [14]. A 'green' alternative to hexavalent chromium is to use Cr(III) (trivalent chromium) electrolytes [36]. In case biocompatibility is sought, there are only few electrodeposited materials with this property, for example some stainless steels (*e.g.* AISI 300 series) and CoCr alloys are very interesting for their overall good features (*i.e.* corrossion resistance, mechanical properties, bio-compatibility) [37]. For the above mentioned reasons, coatings similar to austenitic stainless steel (*e.g.* FeCrNi) created by electrodeposition method meet all the requirements for producing micro- and nanocomponents for bio-medical/micro-robotics applications. However, a stainless steel-like material electroplated using a Cr(III)-based electrolyte need further investigation mainly due to the complexity of the system itself (*e.g.* Cr(III) chemistry has not been completely understood), affecting both plating of films and micro-nanostructures.

1.3 Stainless steel-like electrodeposition of coatings

Electroplating of FeCrNi -based alloys presents various challenges, mainly due to the electrolyte chemistry. So-called anomalous codeposition arises when iron is combined in the solution with other ferromagnetic elements, in this case nickel [14]. Another major issue is trivalent chromium in aqueous solutions, which forms very stable aqua-complexes that are almost impossible to deposit, even at high overpotentials, leading to various side-reactions [38].

1.3.1 FeNi anomalous codeposition

The conventional reduction steps for nickel and iron electrodeposition are the following:

$$Ni(II) \rightarrow Ni(0) \qquad E^0 = -0.25\ V\ vs.\ SHE \tag{1.25a}$$

$$Fe(II) \rightarrow Fe(0) \qquad E^0 = -0.44\ V\ vs.\ SHE \tag{1.25b}$$

However, iron-nickel codeposition from an electrolyte is called anomalous, because in contrast to the typical case, the less noble element (*i.e.* Fe) is deposited preferentially with respect to the more noble one (*i.e.* Ni) even if the Ni/Fe ion ratio inside the bath is greater than one [14]. Different mechanisms have been proposed for explaining such behaviour, mainly considering pH increase at the cathode as the key factor. Hydrogen evolution and thus a local pH increase favours the formation of metal hydroxides [39] or metal hydroxide ions [40]. The models state that iron molecules (hydroxide molecules or ions) are produced faster, hindering nickel molecules or ions deposition by reaching the cathode and being deposited in the metallic state. Matlosz [41] considers the kinetics to be more important than the chemical reactions that are claimed to dominate in the previous cases. In such a model, a two-step mechanism is assumed in which the M(II) (or M^{2+}) ionised metals are first reduced to M(I) (or M^{1+}) adsorbed ions at the cathode, secondly these intermediate ions are reduced to metallic atoms. It is the second step which controls the reduction process. In the iron-nickel case, Fe(I) has a higher reduction rate with respect to Ni(I), leading to the inhibition of nickel deposition.
Nevertheless, this codeposition has not been adequately studied for a system containing an additional element. Especially, in the case of a trivalent chromium bath with additives, no literature is available. In addition, incorporation of impurities is a major factor in Cr(III) electrodeposition, and the influence of FeNi anomalous codeposition on FeCrNi deposition has not been sufficiently investigated.

1.3.2 Trivalent chromium chemistry

Trivalent chromium chemistry in aqueous solution is so-called coordination chemistry. Cr(III) forms a very stable aqua-complex $[Cr(H_2O)_6]^{3+}$, which is thermody-

namically stable and kinetically inert. This close-ordered hexa-water structure makes substitution reactions and electron transfer of the central Cr(III) ion with the electrode surface extremely slow [38, 42, 43]. The electroreduction mechanism for trivalent chromium electrolytes has shown to follow a step-wise mechanism with the formation of rather stable Cr(II) compounds [42, 44–47]:

$$Cr(III) \rightarrow Cr(II) \qquad E^0 = -0.42\,V\ vs.\ SHE \tag{1.26a}$$

$$Cr(II) \rightarrow Cr(0) \qquad E^0 = -0.90\,V\ vs.\ SHE \tag{1.26b}$$

being step (1.26a) the limiting reaction in the Cr(III) to Cr(0) reduction process. Due to the highly negative reduction potential required for chromium deposition, a competing hydrogen evolution reaction (HER) is favoured at the cathode. For acidic solutions (pH < 7) the hydrogen reaction is as in Equation 1.24. HER mainly causes a local pH increase at the cathode surface (due to local shortage of H^+ ions), which leads to side-reactions (*i.e.* hydrolysis, olation and, ultimately, polymerisation [38]), limited chromium growth over time (*i.e.* lower current efficiency) and the formation of internal stresses/cracks and porosity of the coatings. Various mechanisms have been put forward in literature to describe some of these processes. Gabe [48] proposes that the rise of pH results in formation, incorporation and following decomposition of chromium hydrides (Cr-H) inside the deposit. Another explanation is through the generation of chromium hydroxides from hydrolysis reactions in the vicinity of the cathode because of higher pH values [49]. However, very few studies are actually available and a verification of these mechanisms is still missing.

The issues associated with trivalent chromium electrodeposition from an aqueous solution make it very challenging to produce thick, low residual stress and crack-free films. For this reason, the effective electroreduction potential of chromium must be decreased in order to deposit better films containing metallic chromium. One solution is to use a complexing agent whose role is to bind with the metal ions (*via* substitution of water coordination molecules), destabilising them and forming more reactive molecules having a lower kinetic stability than the aqua-complexes.

Various organic molecules have been considered and tested for Cr(III) electroplating, such as formate [43], oxalate [42], acetate [46] and glycine [43, 50]. In the case of FeCrNi -based alloys deposition, complexing agent candidates are formic acid [51], dimethylformamide (DMF) [52], glycine [53, 54] and citrate [55–57]. Glycine shows the best results for Cr(III) complexation in various electroplating systems containing Fe, Ni and Mo.

Glycine (NH_2CH_2COOH) is an organic amino acid that exhibits complexing properties, as well as bipolarity depending on the pH, endowing this molecule with strong buffering features. For these reasons, the Cr(III)-glycine chemistry and its role in the electrodeposition process is extremely complicated. Classical reports

state that the optimal Cr(III):glycine molar ratio is 1:1, with this ratio resulting in chromium electrodeposits with higher deposition rates, better quality and improved uniformity. In this case, the major compound present in the electrolyte is assumed to be the monoligand glycine-Cr complex [50]. However, there is a plethora of literature about trivalent chromium in combination with complexing agents, in particular glycine, with also contradictions in experimental findings due to the intricate chemistry involved. In fact, other side-reactions can take place depending on deposition parameters and electrolyte composition. For example, uncomplexed glycine can react with other elements inside the bath or both at anode and cathode due to this molecule bipolarity. In fact, oxidation of glycine at the anode has been observed to form byproducts such as formaldehyde, carbon dioxide and formic acid [58]. Nevertheless, no clear understanding of this system is evinced and the mechanisms and origins of incorporation of impurities in correlation with material properties are especially controversial and have not yet been verified.

Alternative baths to minimise or fully avoid these problems could be based on ionic liquids. The use of molten salts (with or without water) makes it possible to obtain films with higher deposition efficiencies and avoid concurrent HER [133–136]. However, these solutions are expensive, requiring the use of a glovebox and they are not always compatible with standard photoresists and other polymers used for micro- templating. Other disadvantages include high viscosity, low wettability and nucleation problems, hindering for example the electrodeposition into high aspect ratio templates [137].

Electrodeposition of coatings similar to austenitic stainless steel has not received particular attention in literature. Not many studies are reported about this topic, especially with regard to employing Cr(III) instead of toxic Cr(VI) in the process. Some binary to quaternary alloys have been produced by electroplating: FeCr [53], FeNiCr [52, 59–61], FeNiCrMo [56], but good and uniform characteristics were achieved only for thin films. The complexity of this ternary system needs further investigation in terms of influence of the alloying elements with respect to the final material properties and microstructure. Electrochemical mechanisms are not clear, principally because of the convoluted Cr(III)-glycine electrolyte behaviour during electroplating. Moreover, the role of these factors in the inclusion of impurities in the film is controversial and must be explored and verified.

1.4 Electrodeposition into miniaturised templates

The high demand of advanced MEMS/NEMS for specific applications results in a growing interest in new materials fabricated with techniques which are versatile and economically viable. Electrodeposition has gained great attention in this field because of several advantages over other growth methods, as this technique is cost-effective, scalable and versatile, enabling to deposit inside miniaturised moulds and allowing to have perfect control over both crystallographic structure and morphology. Microscale 2D moulds with high aspect ratio (AR) have been produced in the past decades using the consolidated UV-LIGA process and employed for successfully electroplating metals and alloys in such features [16,62–64]. More recently, two-photon lithography has been used, achieving sub-micron resolution 3D structures [65–68]. The use of this technique for creating moulds, together with electrodeposition, resulted in metallic or hybrid micro-components with complex geometries, *e.g.* nickel microsprings [66]. At the nanoscale, electrodeposition method has been used to grow highly ordered nanowires (NWs) and nanotubes (NTs) by plating mainly into anodic aluminium oxide (AAO) templates, because these membranes provide large pore density (10^{10} pores per cm^2) with high AR (up to 100 µm length) and ordered channels perpendicular to the substrate [69–74]. Efforts on electrodepositing metals and/or alloys into AAO membranes have been done in the past, mainly for Co, Ni, Fe and combinations thereof, as highly ordered nanostructures from these materials are sought when enhanced anisotropic magnetisation is of interest [75–79]. NWs of similar alloys have been achieved, typically by combining Co with Ni and/or Fe, *e.g.* CoNi [78], CoFe [80] and FeNiCo [75,81].

The use of chromium in both micro- and nanoscale systems has not gathered great interest, probably due to hexavalent chromium being extremely toxic and its trivalent chromium alternative having a rather complex electrochemistry. There are only few studies on Cr(III)-based electrodeposition of NWs [82–84]. Moreover, electroplating into miniaturised features relies greatly on experimental data and few studies on the involved mechanisms are present in literature, especially if considering binary to quaternary electrochemical systems. Another challenge which has not been properly explored is the effect of miniaturisation on material properties and microstructure.

1.4.1 Electrochemistry and kinetics inside moulds

The key factors to be considered when electroplating into a miniaturised template are mass-transport of ions and current density. In order to describe this system a model can be retrieved based on three different aspects [85]:

- *Primary current regime* represents the case in which charge transport induced by the electric field is limited only by the resistivity of the bath and not by electrode reactions. This point is important when dealing with com-

plex designs: edges and corners are deposited faster.

- In the *Secondary current regime* the dominating process is electrode reactions (charge transfer limited) and kinetics is described by the Volmer-Butler equations (1.10a),(1.10b). Highly concentrated electrolytes with strong convection leads the system to be in such a state and the deposition becomes independent of the mould design.
- In the *Tertiary current regime* low charge concentrations at the electrode surface are the limiting factor for the deposition process. This is a common problematic case present in high AR LIGA moulds and for non-agitated electrolytes. Here the diffusion layer thickness increases due to difficulties with convective flow [86,87].

The regime of an electrochemical process inside LIGA moulds can be determined by employing dimensionless quantities[9]. Depending on the regime, solving some of these electroplating-inside-moulds issues is possible. Following Mehdizadeh *et al.* [88] definition of active area density (AAD) and Drese's five rules of LIGA design [85], primary and tertiary current density influence on the system can be diminished by template design engineering and by applying shields in order to optimise the current distribution. Additives are commonly used for adjusting some electroplating conditions, for example the use of wetting agents decreases the contact angle between mould resist and electrolyte, thus obtaining a better electrolyte filling rate inside complex features [87]. Another possibility is the use of pulse plating (PP) electrodeposition technique. Here, the deposition occurs during an on-time which is then followed by an off-time period, allowing the electrolyte ions to diffuse and be replenished at the cathode, resulting in the relaxation of the diffusion layer. Another option is pulse reverse plating (PRP), which consist typically of a cathodic pulse (reduction process) followed by a short anodic pulse (oxidation process) which is meant to partially dissolve the material deposited during the previous deposition pulse. In this way, film distribution can be improved. Therefore PP and PRP can mitigate film non-homogeneities and allow for replenishment of species at the cathode surface [64].
Regarding nanoscale templates, it is possible to state that wetting of non-conductive walls, diffusion of electrolyte solutions inside cavities, nucleation and growth are even more complex than in case of LIGA microscale moulds. Most of the kinetic models for nanoporous templates systems agree on the presence of three electrodeposition regions (Figure 1.8) [70,89,90].
At the beginning, for a short time, diffusion of ions inside the pores is linear and time-dependant. In the second region, the current reaches a steady-state be-

[9] Wagner numbers (W_a, W_d) for differentiating between primary, secondary and tertiary regime; Reynolds number (Re) for discriminating the flow regimes; Peclet number (P_e) for characterising hydrodynamic transport of species; Sherwood number (S_h) for characterising mass transport of species

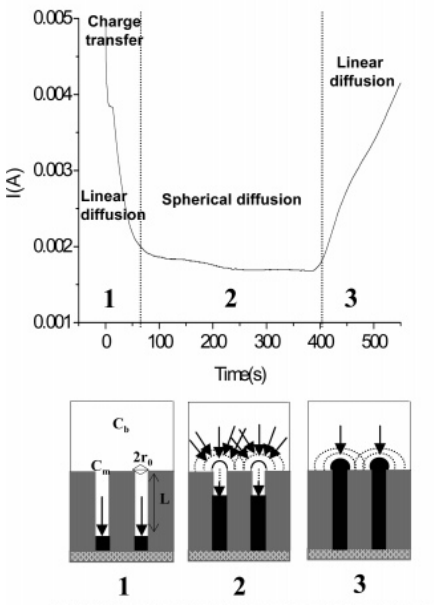

Figure 1.8 – Different kinetic regions when electroplating into nanoporous templates[10]: (top) current *vs.* time, (bottom) schematic representation of the various regimes.

cause the diffusion layer becomes larger than the template thickness, meaning being in a spherical diffusion-controlled regime. When the pores are completely filled, linear diffusion and charge-transfer regime are again dominant.

The concept of current regimes and possible solutions for improving the electrochemical processes inside LIGA moulds are based on a rather limited literature, which mostly consists of experimental confirmations of numerical simulations of both current distribution and mass-transport of ions. Moreover, simple electrochemical systems are usually employed for simplifying the modelling part. In the same way, for the deposition into nanotemplates, only single metals or binary alloys containing cobalt or nickel have been modelled [70]. Electrodeposition of ternary to quaternary alloys into miniaturised moulds has never been investigated thoroughly before, especially in case of more complicated systems based on Cr(III) chemistry.

1.4.2 Miniaturisation *vs.* material properties and microstructure

Regarding micro and nanocomponents, the effects of miniaturisation on various material properties are becoming important and they should be considered for understanding better the material behaviour. Miniaturisation effects can be categorised based on: 1) mould geometries/dimensions, 2) material crystal structure and 3) nanostructured material design.

[10] adapted from Ref. [70]

Electrodeposited microcomponents produced using a standard LIGA process have a minimum dimension on the order of 1-10 µm, therefore alloy properties should not be affected by size effects, which begin to appear for sub-micron features [91].
On the other hand, in the case of nanoporous templates, pore diameter is between 15 and 400 nm, consequently the constrained size is influencing the material characteristics. In compounds with grain sizes comparable to the minimum template dimensions, material strengthening can occur possibly due to dislocation confinement mechanisms [92]. Composition is also affected by moulds size due to variation in current distribution and increase in the density of current lines. In these conditions, side-reactions can become relevant, for example HER leading to enhanced porosity when the mould minimum dimension decreases. Another aspect is the electrodeposition into high AR and highly ordered nanodimensional structures which yields enhanced magnetic features for ferromagnetic elements because of perpendicular anisotropy [93].
Another aspect is nanostructured materials, which can be classified depending on the structure dimensionality: 0D (*i.e.* nanoparticles), 1D (*i.e.* nanowires, nanotubes), 2D (*i.e.* thin films, multi-layers) and 3D (*i.e.* composites). In such cases, size effects and interfaces play an important role and lead to different properties with respect to standard films [35].

However, in case of electroplating of alloys inside micron and sub-micron templates, the present studies in literature focus mainly on the magnetic behaviour [94, 95]. The influence of miniaturisation on the electrodeposition of more complex materials (*e.g.* binary to quaternary alloys) is still missing, as well as the correlation between variation in dimensionality to other important material properties such as corrosion resistance, wear resistance and biocompatibility.

1.4.3 MEMS/NEMS for bio-medical and micro-robotic applications

Miniaturised components are emerging strongly in bio -medicine and -technology, principally for drug delivery and disease diagnosis applications. Many organic compounds are typically studied, because they are considered to be safer for human application. However, inorganic materials show characteristics which are difficult or impossible to replace. Essential in this context are the presence of good mechanical properties. In addition, bio-compatiblity tests have shown good results for many metals and alloys containing chromium, making them suitable in the biomedical sector [2, 3].
Recently, research has been focused on nanostructured inorganic materials for drug delivery applications, such as nanoporous alumina, titania and silica [96], functionalised carbon nanotubes (CNT) [97] and magnetic NTs [98]. However, electrodeposition is employed in very few cases, *e.g.* a magnetic CuNi foam film [99] and a hybrid CoNi/PPy helical magnetic microrobot [100]. This last study

shows the potential of electroplating in miniaturised templates to produce advanced and versatile micro- and nanorobotic components.

Nonetheless, there is still the need to explore electrodeposited metals and alloys with good biocompatibility, magnetic and mechanical features for bio-medical and micro-robotics sectors, especially when electrodeposition is combined with miniaturised moulds/templates. Moreover, coupling size effects at the micro- and nanoscale from different contributions (*e.g.* microstructure, minimum templates geometry/dimensions and material nanostructured design) to the electrodeposition of Cr(III)-based alloys (*e.g.* FeCrNi) is a very novel and challenging topic. Further investigation is required to take advantage of the many possible material properties achievable by using such alloy in combination with different miniaturisation effects.

Statement of the problem

In the research and development of a process for obtaining the desired material characteristics, there are two main sets of inter-related parameters which have to be considered:

1. ***material properties***
   The fundamental ones are *intrinsic or primary material properties*, which are *chemical composition*, *microstructure* and *morphology*. These are the key factors for obtaining a material with tailored features, such as corrosion resistance, magnetic response, etc. (named *extrinsic or secondary material properties*).

2. ***process parameters***
   The fabrication process also determines the overall material properties by means of understanding the *deposition mechanisms*, tuning the *deposition parameters* and varying the *architecture design*.

In this context, FeCrNi similar to austenitic SS is electroplated from an environmentally 'green' Cr(III)-based electrolyte. Even though much research has been carried out, the correlation between deposition process and material properties is missing for Cr(III)-based electroplating systems.

The main issues linked to the electrodeposition of alloys including trivalent chromium ions are the following:

A) Complex Cr(III) chemistry in water solution

- Cr(III)-aqua complexes are formed in aqueous electrolytes, which are kinetically inert and thermodynamically stable. Therefore, large overpotentials are necessary to reduce these chromium ions into their metallic state at the cathode.
  Challenges:
  - side-reactions at the cathode, such as competing HER followed by a local pH increase [38, 101], leading to:
    * poor surface quality (*e.g.* cracks formation)
    * hydrogen embrittlement and porosity
    * low deposition efficiency
  - only very thin films can be achieved

- Complexing agents (organic additives) for Cr(III) are typically employed for improving this deposition by destabilising Cr(III)-aqua species [54].
  Challenges:
  - many complexing agents and their combination have been studied in such system, with no unique understanding for similar findings
  - undesired electrolyte/electrode side-reactions, which can lead to:
    * incorporation of carbon-based impurities
    * variation of composition, morphology and microstructure
    * unexpected material properties

What is missing:

- correlation between *materials properties* and *deposition mechanisms*

B) Ternary alloy electrodeposition employing other transition metals such as iron and nickel

- Codeposition of Fe-Cr-Ni in a system comprised of Cr(III) and a complexing agent have only been studied in few cases [52, 56, 59–61].
  Challenges:
  - anomalous codeposition of Fe-Ni in such system
  - electrolyte stability
  - possible side-reactions at the cathode

What is missing:

- understanding of the FeCrNi system, in particular the *deposition mechanisms* involved
- investigation of the most important *deposition parameters* (*e.g.* experimental set-up, process parameters) affecting the *materials properties* (*e.g.* composition, microstructure)

C) Electrodeposition of Cr(III)-based alloys into miniaturised templates to create micro and nanocomponents

- Only few studies are available on the electrodeposition of Cr(III)-based alloys containing also Fe and Ni, mainly focused on binary systems, with little insight into the scientific findings [82–84, 102].
  Challenges:
  - growth rate inside constrained micro and nanofeatures is affected by limited mass-transport of ions and uneven current density [16].

- supplementary factors must be considered, *e.g.* size effects, non-conductive surfaces and electrolyte infiltration.

What is missing:

- how template assisted ED (constrained micro- nanoelectrodes) is affecting the FeCrNi system, especially in terms of *deposition mechanisms* and *materials properties*
- investigation of optimised processes for obtaining miniaturised components

Research objectives

The core objectives of this research are to investigate the electrodeposition of FeCrNi from a 'green' Cr(III)-based electrolyte in order to obtain a material having similar austenitic SS properties, which then will be used to achieve coatings and micro-nanocomponents for bio-medical applications.

As described previously in the *Statement of the problem*, this system needs to be further studied with regard to the following missing points which are correlated to the core objectives (depicted in Figure 1.9):

1. **electrodeposition mechanisms *vs.* material properties**
   Role of electrolyte composition and set-up on the resulting primary material properties. Thorough understanding of the mechanisms involved in such complex electrodeposition system.

2. **deposition parameters *vs.* material properties**
   Influence of deposition parameters on primary properties such as microstructure and composition. Relation between primary and secondary material properties for such electrodeposits and their comparison with standard metallurgical austenitic SS.

3. **architecture design *vs.* material properties**
   Investigation of the optimised process to fabricate miniaturised components using template assisted electrodeposition. Comparison of electrodeposited micro- nanocomponents and coatings in terms of materials properties, also taking into account the effects of miniaturisation (*i.e.* minimum dimension and geometry).

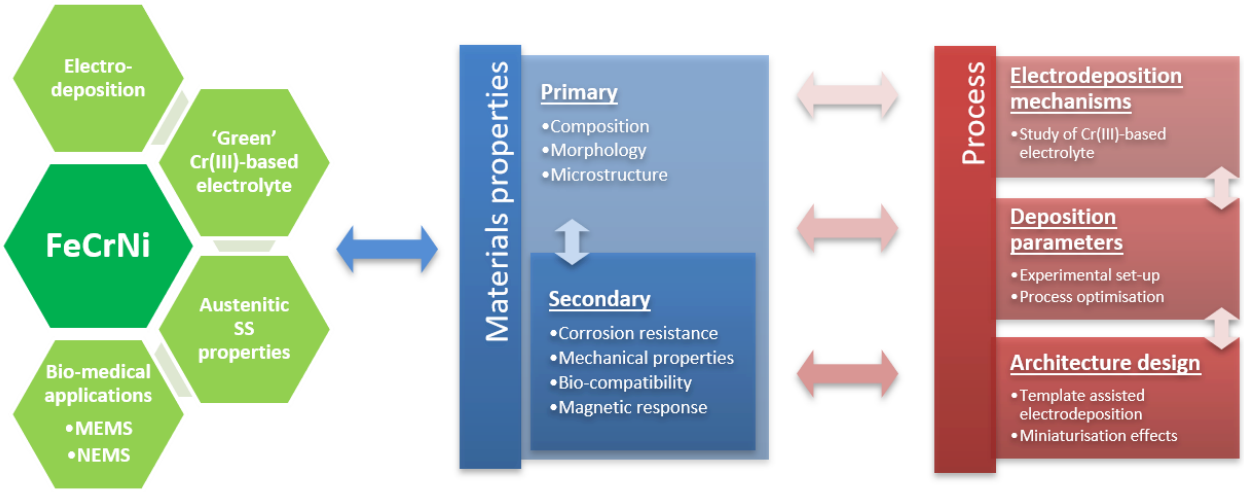

Figure 1.9 – Conceptualisation of the thesis objectives and investigations to be carried out.

2 Materials and methods

2.1 Fabrication of FeCrNi films and micro- nanostructures by electrodeposition

FeCrNi films and micro- nanostructures were deposited using a standard three electrode electrochemical cell equipped with a water jacket for temperature control (see schematic of the electrodeposition framework in Figure 2.1). The temperature of the electroplating bath was set to 22 °C ± 0.5 °C using a temperature controlled circulator (Julabo, F12-ED).

For films, portions of silicon wafer covered with a sputter-coated Au layer (100 nm) deposited on top of a Cr adhesion layer (5 nm) were used as substrates. Prior to each electrodeposition experiment, the substrate was cleaned in a freshly prepared Piranha solution (30% H_2O_2 : H_2SO_4 = 1 : 3) and thoroughly rinsed in deionized water (18.2 MΩ·cm). Subsequently, the substrate (*i.e.* WE) was partially masked with plastic tape to expose a plating area of 1.5 cm x 1.5 cm. A saturated Ag/AgCl electrode was used as RE. Depending on the experiment, a platinum mesh (80 mesh, 25 mm x 35 mm, ALS Co., Ltd) or pure Ni pellets inside a platinised titanium basket (PtTi fine mesh, HxWxD 65 mm x 50 mm x 15 mm) were used as a CE.

As for the nanostructures, the cell comprised a saturated Ag/AgCl electrode as RE and a platinum mesh (80 mesh, 25 mm x 35 mm, ALS Co., Ltd) as CE. Commercial membranes (Smartmembranes GmbH, Germany) with 50 µm thickness and 350 nm diameter pores, were sputtered with 5 nm Cr (adhesion layer) and 150 nm Au (conductive layer) and were used as WE in order to obtain NWs and/or NTs. After electrodeposition, the AAO templates were dissolved via chemical etching in chromic oxide (1.8 wt%) and phosphoric acid (7 wt%, 85 %) aqueous solution mixture at room temperature. Whereas for microcomponents (*i.e.* micro-pillars), the electrodeposition was performed into moulds produced by UV-LIGA lithography process.

The compositions of the electrolytes used in the electrodeposition of FeCrNi are shown in Table 2.1 for aqueous electrolytes reported in Chapters 3 and 4, and in Table 2.2 for mixed-solvent electrolytes reported in Chapters 5 and 6 .

All the chemicals were of reagent grade (Sigma-Aldrich) and were used as-received without any further purification. For the *Standard* bath preparation, a first solution (*solution1*) containing chromium chloride and glycine was mixed thoroughly with deionised water (DI water) in a glass beaker. Then, this solution was heated at 80 °C for at least 30 minutes in order to completely complex

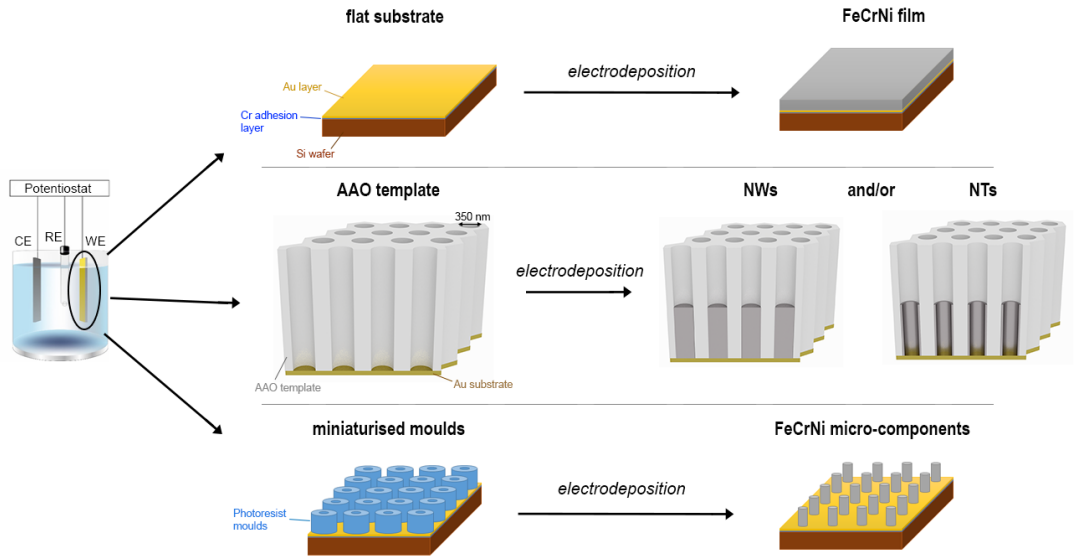

Figure 2.1 – Schematics of the electrodeposition protocol used for obtaining FeCrNi coatings (using a flat substrate), nanostructures (using nanoporous AAO templates sputtered with Cr and Au) and micro-components (using UV-LIGA moulds).

chromium ions with glycine. Afterwards, it was cooled down to room temperature and kept overnight. In a separate beaker, the rest of bath components were mixed with DI water (*solution2*). Then, *solution1* and *solution2* were mixed together at room temperature (*solution1+2*). The volume of *solution1+2* was adjusted with the corresponding solvent (in this case DI water) to reach 400 mL and the pH to be 1, obtaining the final electrolyte.

The electrodeposition was carried out using a potentiostat (PGSTAT 302N, Metrohm Autolab B.V.) controlled by NOVA (version 2.1) software, mostly in galvanostatic mode. The electrolytes were aged galvanostatically for a few hours at a constant current density to obtain films with good surface morphology and uniformity.

In Chapter 3 (*FeCrNi from aqueous electrolyte: role of anode and electrolyte on composition, microstructure and electrodeposition mechanisms*), two investigation approaches were followed to understand the deposition mechanisms involved in the Cr(III)-based FeCrNi electrolyte. Particular emphasis was placed on the role of Cr(III), additives (*i.e.* glycine) and ferromagnetic elements (*i.e.* Fe and Ni) on material composition and microstructural changes of FeCrNi electroplated films. The first approach involved studying the influence of the anode material by electrodepositing FeCrNi alloys using a platinum anode (*Pt anode*) and a pure nickel anode (*Ni anode*). The applied deposition parameters were the same for both cases (current density = -80 mA cm^{-2}, total deposited charge

Table 2.1 – Composition of the various aqueous FeCrNi electrolytes.

Electrolyte →	*Standard*	*No Cr-Glycine*	*No Cr*
	concentration (mol L^{-1})		
$CrCl_3 \cdot 6H_2O$	0.4	-	-
Glycine (NH_2CH_2COOH)	0.4	-	0.4
$FeCl_2 \cdot 4H_2O$	0.03	0.03	0.03
$NiCl_2 \cdot 6H_2O$	0.2	0.2	0.2
NH_4Cl	0.5	0.5	0.5
H_3BO_3	0.15	0.15	0.15
NaCl	0.5	0.5	0.5

pH = 1
temperature = 22 °C

density ≈ 200 C cm^{-2}) resulting in average deposition potentials of -1.44 and -1.41 V *vs.* Ag/AgCl for the *Pt anode* and *Ni anode* cases, respectively. Next, the samples were annealed using a rapid thermal annealing (RTA) system (MILA-5050, ULVAC) under an Ar controlled atmosphere (99.9999% purity) for 1 hour at 600 °C (ramp up and ramp down of 10 °C min^{-1}). In the second approach, the influence of Cr(III)-glycine complexation was studied using three different electrolytes (Table 2.1): *Standard*, *No Cr-Glycine* (*Standard* without chromium and glycine) and *No Cr* (*Standard* without Cr). FeCrNi electrodeposition was performed galvanostatically at -60 and -80 mA cm^{-2} (total deposited charge density ≈ 50 C cm^{-2}) from *Standard* electrolyte resulting in average deposition potentials of -1.30 and -1.44 V *vs.* Ag/AgCl, respectively. For *No Cr-Glycine* and *No Cr* baths electrodeposition at current density of -80 mA cm^{-2}, average deposition potentials were -1.55 and -1.39 V *vs.* Ag/AgCl, respectively. A platinum anode was used as the CE in all experimental variations.

In Chapter 4 (*FeCrNi from aqueous electrolyte: role of chromium content on material properties*), electrodeposition of films was performed using a platinum anode as CE, in galvanostatic mode with a current density ranging from -50 to -100 mA/cm^2. The material properties of such electrodeposits have been investigated.

In Chapter 5 (*FeCrNi mixed-solvent vs. aqueous electrolytes: coatings and micro-nanocomponents*), electrodeposition was performed from both aqueous and mixed-solvent electrolytes and the results have been compared. The aqueous electrolyte used was the *Standard* one, whereas mixed-solvent ethylene glycol (EG, ≥ 99 % purity) electrolytes were obtained with the same procedure as for the *Standard* aqueous solution, with the only difference of adjusting the base solution (*solution1+2*) with EG in order to reach the final desired volume proportions as showed in Table 2.2, either 30 vol% or 50 vol% EG. The conditions used

Table 2.2 – Composition of the various mixed-solvent FeCrNi electrolytes.

Electrolyte →	*Standard aqueous*	*30 vol% EG*	*50 vol% EG*
	concentration (mol L^{-1})		
$CrCl_3 \cdot 6H_2O$	0.4	0.4	0.4
Glycine (NH_2CH_2COOH)	0.4	0.4	0.4
$FeCl_2 \cdot 4H_2O$	0.03	0.03	0.03
$NiCl_2 \cdot 6H_2O$	0.2	0.2	0.2
NH_4Cl	0.5	0.5	0.5
H_3BO_3	0.15	0.15	0.15
NaCl	0.5	0.5	0.5
Water volume (mL)	400	300	220
EG volume (mL)	-	100	180
Total volume (mL)	400	400	400

pH = 1
temperature = 22 °C

for the electrochemical cell set-up were the same as in Chapter 4 for both films and micro- and nanostructures. FeCrNi films were galvanostatically electrodeposited until a total charge of 400 C was reached. Different current densities were applied depending on the electrolyte in order to obtain similar compositions: -80 mA cm^{-2} (average deposition potential -1.44 V *vs.* Ag/AgCl), -50 mA cm^{-2} (average deposition potential -1.52 V *vs.* Ag/AgCl) and -30 mA cm^{-2} (average deposition potential -1.65 V *vs.* Ag/AgCl) corresponding to *Standard aqueous* solution, *30 vol% EG* and *50 vol% EG* mixed-solvent electrolytes, respectively. Regarding the electrodeposition into AAO templates, the total deposition time for each sample was approx. 5 hours and the current density varied depending on the used electrolyte: -20 mA cm^{-2} for *Standard aqueous* electrolyte, whereas -10 and -5 mA cm^{-2} for *30 vol% EG* electrolyte.

Micro-components were obtained by electroplating into micromoulds obtained by either UV-LIGA process or two-photon lithography. All the preparation steps for the template creation were performed in a cleanroom Class 10.000 (Empa - Thun). The final template obtained in this study was aimed to create micro-pillars with a diameter of 25 µm. Therefore, the design utilised was a matrix of hollow cylinders with an external diameter of 225 µm, an internal diameter of 25 µm and in inter-distance between each others of 50 µm. The typical UV-LIGA process is depicted in Figure 2.2.

Step 1, the Au/Cr/Si substrate was dehydrated on a hot plate for at least 20 minutes at 180 °C. Step 2 was optional and in this case not used. Immediately after (Step 3), SU-8 negative photoresist GM 1075 (Gersteltec Sarl) was spin coated

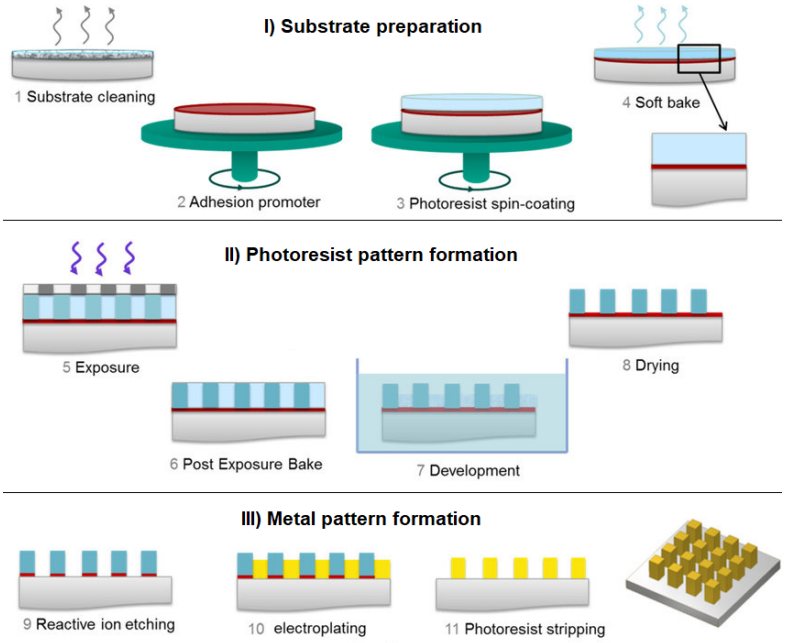

Figure 2.2 – Schematic of UV-LIGA process resulting in an electrodeposited pattern[1].

using a spin-coater (SM-180-BT, Sawatec AG) at different rotation speed (revolutions per minute - RPM) depending on the targeted thickness (typically 1900 RPM for achieving 80 µm thick SU-8 coating). Soft bake (Step 4) was performed afterwards with a hot plate (HP-401, Sawatec AG) at 120 °C for 1 hour. Exposure of the resist through the desired mask was done using a 4-inch mask aligner MA6 (Karl Süss) in hard contact mode using a typical exposure dose of approximately 200 mJ cm^{-2} (power of the UV lamp 8.1 mW cm^{-2}). Post exposure bake (Step 6) was implemented with a hot plate for 1 hour at 90 °C. The substrate was developed (Step 7) up-side down in propylene glycol methyl ether acetate - PGMEA (Reagent Plus, $\geq$ 99.5 % purity) for 15 minutes, followed by 2-propanol (puriss. p.a., $\geq$ 99.8 % purity) rinsing and then let it dry (Step 8). Reactive ion etching (Step 9) was not used because of Step 2 optional. Instead, the templates were descumed for 20 min with a 450 W oxygen plasma (O.P.) treatment (MUEGGE R3T system) for improving electrolyte infiltration inside non-conductive cavities. Electrodeposition inside UV-LIGA moulds (Step 10) was performed via a CV-like deposition, sweeping the potential between -1.7 and -0.5 V *vs.* Ag/AgCl with a scan rate of 10 mV/s. The surface was mechanically polished to remove the possible over-growth and to obtain a uniform flat surface. At the end, the photoresist was etched away (Step 11) with a 400 W O_2-CF_4-N_2 plasma treatment (MUEGGE R3T system) for few hours.

In Chapter 6 (*FeCrNi mixed-solvent vs. aqueous electrolytes: materials prop-*

[1] adapted from Ref. [103]

erties), the analysed electrodeposited coatings were the same as obtained in Chapter 3 and Chapter 4 for *Standard aqueous* electrolyte and in Chapter 5 for *30 vol% EG* electrolyte (in this chapter called *Mixed-solvent EG*).

2.2 Morphology and microstructure analysis

The morphology characterisation of the FeCrNi samples was performed *via* field-emission scanning electron microscopy (FE-SEM, Hitachi S-4800, Hitachi High-Technologies Corporation) for both films and micro- nanocomponents (*i.e.* NWs/NTs from AAO cross-section and components from miniaturised moulds) and *via* dual-beam FE-SEM/Ga FIB system (Tescan Lyra3, Tescan Orsay holding a.s.) for dispersed FeCrNi NWs.

Crystal structures were characterised by means of *in-situ* Bragg-Brentano X-ray diffraction (BB-XRD, Brucker) with a Cu $K\alpha$ radiation source (40 kV, 40 mA). Diffractograms were recorded in the 2θ range between 15 and 100 °. An offset of 1 ° was used to avoid the signal from the Si substrate. Moreover, possible fluorescence signals associated with the presence of Fe in the films were filtered by using a larger lower discriminator. The mean size of the crystallite τ (more specifically, the coherent diffraction length) was calculated using the Debye-Scherer equation

$$\tau = \frac{K\lambda}{\beta \cos\theta} \tag{2.1}$$

where K is the shape factor (0.9), λ is the radiation wavelength, λ is the broadening of full width half maximum (FWHM) of the selected peak and θ the corresponding Bragg angle. The used peaks and Bragg angles were (110) peak at 2θ=45 ° for the α-Fe phase and (111) peak at 2θ=44 ° for the γ-Fe phase. Fitting of the XRD peaks was performed by using the Crystallographic Open Database - COD [104].

2.3 Composition analysis

X-ray fluorescence (XRF, Fischerscope® X-RAY XDV®-SDD, Fischer Technology) was used to estimate the Fe-Cr-Ni wt% and thicknesses along the coating sample area. The measurements were performed at 25 uniformly distributed points on each specimen. The films were characterised by an uneven composition from the edges to the centre of the sample (Cr variation $\approx$ 15 wt%), caused by the primary current distribution during electrodeposition. Therefore, the averages of 9-matrix central points on each sample were chosen as representative concentrations. Approximate current efficiencies (C.E., %) from XRF thickness measurements were calculated by knowing the weight percentage of each metal element, assuming the density of stainless steel to be ρ_{SS} = 7.93 g cm^{-3}

and using Faraday's law.

The elemental composition (at%) and chemical binding energies (BE) of the metal species (Fe, Cr and Ni) and impurities (O, C and N) were evaluated *via* X-ray photoelectron spectroscopy (XPS) on the coatings' surface and profiling at different depths from the surface down to approximately 500 nm. The representative bulk concentrations were the ones measured after approximately 50 min of sputtering time in-depth of the coating. In Chapter 6, XPS concentration and fitting were also evaluated after 5 min sputtering time in order to correlate the surface chemical states with the material properties. In-depth profiling was achieved by sputtering the material with Ar^+ ions (2 or 4 keV sputtering energy). XPS data was acquired using various equipment:

- Physical Electronics (PHI) 5500 Multi-technique System[2] to investigate the influence of anode type on as-deposited films electrodeposited from aqueous solution.
- Physical Electronics (PHI) Quantum 2000 Scanning ESCA Microprobe System[3] to investigate the effect of thermal annealing on films obtained from aqueous electrolyte and to compare the composition variation of coatings obtained from mixed-solvent and aqueous electrolytes.
- Physical Electronics (PHI) VersaProbe II Scanning XPS Microprobe System[4] to determine the impact of Cr(III)-glycine complexation on films' properties by varying the aqueous electrolyte composition.

XPS spectra were analysed using CasaXPS software [105] (version 2.3.19). The spectra were charge corrected by shifting all binding energies (BE) with respect to adventitious carbon (C 1s; C-C, C-H) at 284.8 eV. The regions of interest and

[2]Monochromatic Al K-alpha X-ray radiation source ($h\nu$ = 1486.6 eV) of 350 W power with a typical beam diameter of 800 µm. Hemispherical capacitor electron-energy analyser equipped with a multichannel plate detector. Electron take-off angle of 45 ° and analyser operated in the constant pass energy mode at 23.50 eV. Compensation of eventual surface charging with built-in electron neutraliser. Base pressure of the system below $1 \cdot 10^{-8}$ Pa. Binding energy calibrated using Ag $3d_{5/2}$ at 368.21 eV with FWHM of 0.8 eV.

[3]Monochromatic Al K-alpha X-ray radiation source ($h\nu$ = 1486.7 eV) of 29.7 W power with a typical beam diameter of 150 µm. Hemispherical capacitor electron-energy analyser equipped with a channel plate and a position-sensitive detector. Electron take-off angle of 45 ° and analyser operated in the constant pass energy mode at 29.35 eV. Compensation of eventual surface charging with built-in electron and argon ion neutralisers. Base pressure of the system below $5 \cdot 10^{-7}$ Pa. Binding energy calibrated using Cu $2p_{3/2}$, Ag $3d_{5/2}$ and Au $4f_{7/2}$ at 932.62 eV, 368.21 eV and 83.96 eV, respectively to within $\pm$ 0.1 eV.

[4]Monochromatic Al K-alpha X-ray radiation source ($h\nu$ = 1486.7 eV) of 25.2 W power with a beam diameter of 100 µm. Spherical capacitor electron-energy analyser set at 45 ° take-off angle respect to sample surface. Analyser operated in the constant pass energy mode at 46.95 eV. Compensation of eventual surface charging with built-in electron and argon ion neutralisers. Base pressure of the system below $5 \cdot 10^{-7}$ Pa. Binding energy calibrated using Cu $2p_{3/2}$, Ag $3d_{5/2}$ and Au $4f_{7/2}$ at 932.62 eV, 368.21 eV and 83.96 eV, respectively to within $\pm$ 0.1 eV.

corresponding relative sensitivity factors (R.S.F.) for elemental quantification and fitting were 1s for oxygen, carbon and nitrogen, and $2p_{3/2}$ for Fe, Cr and Ni elements. Core level XPS peak fitting was performed using an asymmetric line shape defined in CasaXPS as LF(α, β, w, m), where α and β set the spread of the tail on each side of the Lorentzian component. The w parameter is the damping factor, which gives the integration limit for tail reduction and m is the width of the Gaussian convoluted with the Lorentzian. All other components were fitted using a Gaussian (Y%)-Lorentzian (X%) profile defined in CasaXPS as GL(X), where Y=100-X and the X value was varied depending on the analysed element (from 25 to 50). Moreover, a standard Shirley background was used for all spectra.

Compositional characterisation (Fe-Cr-Ni-O-C, at%) of the dissolved NWs was carried out by energy dispersive X-ray (EDX) analysis on the Tescan Lyra3 system with a 30 kV accelerating voltage.

Additionally, H ratio in at% with respect to all metal species (Fe, Cr and Ni) was determined for electrodeposited films at depths up to 200 nm by helium elastic recoil detection analysis (He-ERDA, ETH Zurich) using a 2 MeV He beam and the absorber foil technique [106]. The representative concentration of hydrogen was the one measured after approximately 20 min sputtering time in-depth of the coating.

Atom probe tomography (APT, EIKOS X [107], CAMECA Instruments Inc. - Madison - USA) was performed on the FeCrNi electrodeposited films from aqueous solution. Lift-out specimens attached to W posts were sharpened into tip geometry with radius of $\approx$ 50 nm using focused ion beam annular milling. Atom probe analysis was conducted in laser pulsing mode with wavelength of 532 nm and laser pulse energy of 13-20 nJ operating at 200 kHz with a specimen base temperature of 50 K and detection rate set to 0.005-0.02 atom per pulse. The typical dataset size of each analysis is around 10-50 M ions. IVAS 3.8 software from CAMECA was used for data reconstruction, detailed analysis for local chemical identification/composition (deduced from mass-over-charge ratio) and distribution of impurities.

2.4 Chemical characterisations

Chemical equilibrium diagrams and concentration of species for the aqueous electrolytes were evaluated using Hydra-Medusa software [108].

UV-vis absorbance spectra were measured in the wavelength range between 300 to 700 nm using a UV-vis spectrophotometer (UV-vis Lambda 900 UV, PerkinElmer)

for different electrolytes: freshly prepared FeCrNi electrolytes (*i.e. Standard aqueous*, *30 vol% EG*, *50 vol% EG*) and galvanostatically aged aqueous FeCrNi electrolytes (using platinum or nickel anodes) diluted 10 times (final Cr(III)-glycine concentration of 0.04 M) into the corresponding solvent (*i.e.* DI water, 30 vol% EG, 50 vol% EG), trivalent decorative chromium and hard hexavalent chromium commercial electrolytes (riag Oberflächentechnik AG, Switzerland) diluted in DI water 10 and 20 K times (final Cr ions concentration unknown), respectively. Prior each measurement, for each electrolyte, the corresponding solvent baseline has been taken into account by the software via background subtraction.

Electrolytic conductivity have been measured at room temperature (approx. 25 °C) using a conductometer (914 pH/Conductometer, Metrohm AG) resulting in κ equal to 99.74 and 45.91 mS cm^{-1} for aqueous and mixed-solvent (30 vol% EG) FeCrNi solutions, respectively. Instead dynamic or absolute viscosities of each electrolyte have been evaluated using a rheometer (Discovery Hybrid HR-3 Rheometer, TA instruments) at room temperature (22 °C) taking the values at high shear rate when reaching steady-state values. Kinematic viscosities (ν [m^2 s^{-1}]) were approximatively calculated considering the densities (ρ [kg m^{-3}]) at room temperature ($\approx$ 23 °C) of deionised water (997 kg m^{-3}) and of 25 vol% EG/water mixture [109] (1068 kg m^{-3}), resulting in kinematic viscosities of $1.5 \cdot 10^{-6}$ and $3.6 \cdot 10^{-6}$ m^2 s^{-1} for *Standard aqueous* and *30 vol% EG* electrolytes, respectively.

Linear sweep voltammetry was performed on flat substrates into the various used electrolytes (*i.e.* aqueous and mixed solvent) using the previously mentioned set-up (standard three-electrode electrochemical cell and a potentiostat) with a scan rate (SR) equal to 10 mV s^{-1} and varying the potential from -0.25 to -1.75 V *vs.* Ag/AgCl, with a measured open circuit potential (OCP) of 0.40 V *vs.* Ag/AgCl. This allowed to obtain the various reduction peaks corresponding to iron, nickel and chromium ions.

Additionally, LSV were performed using a RDE set-up in order to retrieve more detailed kinetics information of aqueous and mixed-solvent electrolytes. The set-up was composed of a standard electrochemical cell containing 100 mL volume of solution. The WE was a rotating disk platinum electrode with a diameter of 5 mm, the CE was also a platinum electrode and the RE was a saturated Ag/AgCl electrode (all electrodes, Metrohm AG). Prior experiments, the solution was bubbled with N gas for 30 minutes. The used rotation speed were 1000, 2000 and 4000 RPM corresponding to 104.7, 209.5 and 419 rad s^{-1}, respectively. The data was fitted to Koutecky-Levich theory (equation (1.22)), explaining the kinetic behaviour of the studied systems under mass-transport controlled conditions (diffusion coefficients for the active ion species were approximatively evaluated).

Corrosion behaviour of the FeCrNi electrodeposits was analysed by anodic linear sweep voltammetry in a 0.5 M H_2SO_4 aqueous solution at 23 °C and in a DMEM (Dulbecco's Modified Eagle Medium) biological medium at neutral pH at 37 °C. In addition to the electrodeposited films (from both aqueous and mixed-solvent electrolytes), commercial disks of AISI 316L (Cr18-Ni10-Mo3) and AISI 304 (Cr18-Ni10) were investigated as reference standard metallurgical samples for comparison. The measurements were performed in a conventional three electrode electrochemical cell. The test solution was freshly prepared and de-aerated in the electrochemical cell with Ar bubbling for at least 30 min prior to each experiment. A FeCrNi electrodeposited film was placed in a Teflon sample holder with an exposed electrode area of 9 mm in diameter. Platinum wire was used as CE, while a Ag/AgCl electrode was used as RE. For AISI 316L and AISI 304 disks, samples were cleaned in acetone with sonication for 15 min, followed by rinsing in ethanol. Then, they were further cleaned in Piranha solution for a few minutes to remove any residual surface contamination prior to each measurement. The electrodeposited films were cleaned in deionized water before measurements. The cleaned samples (AISI 316L, 304 and electrodeposited samples) were immersed in the test solution (0.5 M H_2SO_4) for 15 min prior to each measurement. For this solution, a cathodic pre-treatment was carried out at -0.6 V *vs.* Ag/AgCl for 15 min. The anodic linear sweep voltammetry was performed from -0.6 to +1.5 V *vs.* Ag/AgCl at a scan rate of 1 mV s^{-1} immediately after the cathodic pre-treatment. For the DMEM biological solution, no cathodic pre-treatment was employed, and the anodic LSV was performed under the same conditions as for the acidic medium.
For each polarisation scan, the corrosion parameters (E_{corr} and i_{cor}) have been extracted from the Tafel method by using only the cathodic part of the measurement (due to the passive film formation in the anodic part).

2.5 Bio-compatibility tests

For the cytotoxicity tests, all the tested samples (electrodeposited FeCrNi from aqueous or mixed-solvent EG electrolytes, AISI 304 and AISI 316L SS) were sterilized by incubating them overnight in 70% ethanol/water. Afterwards, they were thoroughly washed with phosphate-buffered saline (PBS) and transferred to a 6-well cell culture plate.
In Chapter 4 (*FeCrNi from aqueous electrolyte: role of chromium content on material properties*), cells (A549, human adenocarcinoma cell line) were seeded into 6-well cell culture plates containing the steel samples (n=3 for every plate). Cells were seeded on the samples at a density of 100000 per mL in DMEM medium containing 1% fetal bovine serum (FBS) and antibiotics. For the positive control, cells were lysed with 0.1% Triton X (total lysis). Cells not exposed to samples served as negative control. After 24 hours, supernatants were collected and lactate dehydrogenase release into the medium was measured by the lactate

dehydrogenase (LDH) kit following the manufacturer's protocol (NonRadioactive Cytotoxicity Assay, Promega). The results are expressed relative to the positive control (total lysis, equivalent to 100% cell death). Cells were then fixed with 4% paraformaldehyde (PFA) for 12 hours at 4°C and permeabilized with 0.1% Triton X for 2 minutes. The cytoskeleton of the cells was then stained with Phalloidin Alexa 488 (Life Technologies, following the manufacturer's protocol). The nucleus was stained with DAPI (4',6-diamidino-2-phenylindole). Cells were then imaged using a Zeiss Axio Fluroescence microscope. For scanning electron microscopy, cells were gradually dehydrated with ethanol (30%, 50%, 70%, 80%, 90%, 100% (3x) for 5 minutes each), coated with 7 nm of gold and imaged in a FE-SEM (Hitachi S-4800, Hitachi High-Technologies Corporation) using a voltage of 2 kV.

In Chapter 6 (*FeCrNi mixed-solvent vs. aqueous electrolytes: materials properties*), NHDF, a non-cancerous human skin fibroblast cell line (Sigma-Aldrich, Switzerland), was used for cytotoxicity evaluations. Cells were cultured in Dulbecco's Modifies Eagle Medium (DMEM) – high glucose (#RNBG3787, Sigma-Aldrich, Switzerland) supplemented with 10% FCS, 1% PSN and 1% L-Glutamine. Normal human dermal fibroblasts were then seeded into 6-well cell culture plates containing the steel samples (n=3 per sample). Cells were seeded on the samples at a density of 200000 per mL in DMEM medium containing 1% fetal bovine serum (FBS) and antibiotics. For the positive control, cells were lysed with 0.1 % Triton X (total lysis). After 24 hours, supernatants were collected and lactate dehydrogenase release into the medium was measured by the lactate dehydrogenase (LDH) kit following the manufacturer's protocol (NonRadioactive Cytotoxicity Assay, Promega). The results are expressed relative to the positive control (total lysis, equivalent to 100% cell death). Of note, the annealed coatings slightly delaminated at the edges during the experiment.

2.6 Magnetic characterisation

Magnetic hysteresis loops (intensity of magnetisation M *vs.* magnetic field H) were recorded at room temperature (300 K) varying the magnetic field between -20 to +20 kOe, sampling every 1 kOe in the ranges [-20 to -2 kOe] and [+2 to +20 kOe], whereas sampling every 20 Oe in the range [-2 to 2 kOe].

In Chapter 4 (*FeCrNi from aqueous electrolyte: role of chromium content on material properties*), a vibrating sample magnetometer (VSM, Oxford Instruments) has been employed with a maximum applied magnetic field of 1 Tesla. The magnetic field was applied along the film plane direction.

In Chapter 6 (*FeCrNi mixed-solvent vs. aqueous electrolytes: materials properties*), a superconductive quantum interference device vibrating sample magnetometry (SQUID-VSM) in a Quantum design MPMS3 setup was used. The magnetic field was applied along the film plane direction.

2.7 Tribological measurements

Tribological measurements were performed with a tribometer (CSM instruments) in dry friction condition, ball-on-flat configuration (linear sliding) using a corundum (Al_2O_3) ball of 6 mm diameter in a controlled atmosphere with constant temperature ($\approx$ 21 °C) and humidity ($\approx$ 50 %). The number of cycles was set to 100 and various normal loads were tested from 1 to 5 N, but only the results at higher loads (*i.e.* 5 N) have been considered in this work because more reliable due to the higher uncertainties affecting low loads measurements.
After tribological tests, cross-section profiles and roughness measurements were performed using a standard surface profilometer (SURFTEST SJ-210, Mitutoyo) with a diamond tip of 2 µm diameter applying a force of 4 mN at a speed of 0.25 mm/s using the differential inductance method.
The analysed samples were FeCrNi electrodeposits with various chromium content characterised by large thickness (more than 5 µm), compared to commercial disks of austenitic AISI 304 and 316L SS.

2.8 Mechanical tests

Indentation measurements were performed on the original electrodeposits surfaces (as-deposited and annealed) and on the area that had been measured by XPS (in-depth, after sputtering process). A Hysitron Ubi Nanoindenter equipped with a Berkovich-shaped diamond tip was used for all the tests. The area function of the indenter tip had been calibrated with fused silica prior to the experiments. Loading and unloading were done over 5 s, while the maximum load of 10 mN was held for 2 s. In order to obtain the hardness and reduced elastic modulus, the load displacement curves were analysed using the Oliver-Pharr Method [110] and at least 25 individual indents were measured to obtain a representative average. An average Poisson's ratio of 0.3 was considered in order to calculate the elastic modulus from the reduced one [111].

3 FeCrNi from aqueous electrolyte: role of anode and electrolyte on composition, microstructure and electrodeposition mechanisms

Cr-based alloys (*e.g.* FeCrNi) electrodeposited from environmentally friendly trivalent chromium electrolytes are crucial for industrial application for facilitating the transition towards sustainable and ecological production and processing. Moreover, electrodepositing multicomponent alloys containing chromium allows to obtain films with a combination of properties that cannot be achieved by pure chromium coatings. Nevertheless, these processes have not been comprehensively studied or understood in depth, especially the role of organic agents (common additives for improving Cr(III)-based plating; *e.g.* glycine) in terms of material properties of the electrodeposits.

In the literature, the use of Fe and Ni in a Cr(III)-complex electrochemical system can be found for FeNiCr [59,60,102] and FeNiCrMo [56]electrodepositions. However, these works mainly focus on the influence of deposition parameters on film features (*e.g.* corrosion resistance, mechanical properties), overlooking the role of the electrochemical reactions on the coating's composition and properties. Only one of our previous publications [112] tackled the electrodeposition of FeCrNi from a Cr(III)-glycine electrolyte and put forward an explanation for the source of impurities incorporated in the films. According to this study, the use of an inert platinum anode was the cause of the oxidation of glycine, which resulted in the formation of by-products (*e.g.* formaldehyde, formic acid). These were, in turn, the main source for carbon inclusion and consequent amorphisation of the deposit.

Other impurities, such as high amount of carbon/carbides can decrease the corrosion resistance [29,113], while nitrogen and hydrogen are also known to have an impact on morphology and other properties of chromium-containing alloys like austenitic SS [114]. According to Gabe [48], a local rise of pH at the cathode results in the formation, adsorption and incorporation of chromium hydrides (Cr-H). Hydrogen incorporation is thought to play a key role in the coating's porosity and embrittlement, lowering deposition efficiency and producing amorphous films, as it was also suggested in the previous chapter.

There is a lack of thorough research aiming to explain or to better understand the possible mechanisms involved in the electrodeposition of alloys from Cr(III)-based electrolytes (*e.g.* FeCrNi) and how these ED mechanisms are linked to the obtained films' properties (*e.g.* composition, microstructure, etc). This is particularly true regarding the pathways by which impurities are incorporated in the deposits, as they are as important as the main metallic elements in determining the coatings' material properties. It is crucial to investigate how the morphology, microstructure and film composition are affected by deposition parameters and post-processing for these systems. This is a necessary step for further improving Cr(III)-based electrodeposition, considering that the process is of great importance for environmentally friendly and sustainable applications which make use of chromium.

In this chapter, the objective is to investigate the influence of an electrolyte consisting of Cr(III)-glycine complexes, Fe and Ni ions, in terms of morphology, microstructure and composition of the resulting electrodeposits. The influence of impurities and deposition parameters on material's properties is assessed by first varying the anode material and then the electrolyte composition, in combination with post-treatments (*i.e.* thermal annealing) and several advanced characterisation techniques. In particular, XRD and XPS are utilised to correlate coating microstructure and composition, while taking into account the chemical states of Fe, Cr, Ni, O, C and N. Additionally, He ERDA is used to accurately determine the hydrogen content throughout the coating's thickness. Furthermore, 3D atom-by-atom elemental reconstruction is implemented using cutting-edge APT. This technique is used to precisely determine which elements/compounds are present and how they are spatially distributed within the FeCrNi coatings at the nano-scale, providing information regarding material inhomogeneity (*i.e.* clustering, phase separation, precipitates) and coating elemental evolution during microstructural and material composition variations (before and after annealing process). The influence of glycine in terms of metals complexation, and chromium speciation within different chromium-based electrolytes are evaluated by means of chemical equilibrium diagrams and UV-vis spectra, respectively. Based on the obtained results, some mechanisms are proposed to explain the following processes involved in the amorphisation of the FeCrNi electrodeposits:

1. Complexed Cr(III) electroreduction.
2. Complexing agent (*i.e.* glycine) side-reactions.
3. Influence of transition metals (*i.e.* Fe, Ni) on cathodic reduction processes.

Declaration of contribution

In this work, Enrico Bertero fabricated the samples by electrodeposition and characterised them using SEM, XRF, XRD and XPS, contributed to most of the data analysis and writing. Cristina V. Manzano (Empa - Thun) annealed the samples and provided support on data analysis and writing. Eva Pellicer and Jordi Sort (UAB - Barcelona) provided support on XPS measurements and on the overall research results. Robert M. Ulfig (CAMECA - USA) performed APT on the samples and gave support to the resulting analysis. Max Döbeli (ETH - Zurich) performed He ERDA measurements. Stefano Mischler (EPFL - Lausanne) provided support on XPS results and on the overall research results. Johann Michler and Laetitia Philippe (Empa - Thun) supervised the work and provided the facilities to carry out the work.

Parts of this chapter use materials adapted from Bertero *et al.* [115] with permission from the Royal Society of Chemistry.

3.1 Anode role investigation

3.1.1 Surface morphology

The electrodeposit from the *Ni anode* differs slightly in terms of appearance from that obtained using the *Pt anode*. Semi-bright grey coatings were achieved from both anodes, however the one produced using the *Ni anode* is less uniform, as the borders appear to be duller and more fragile. The differences between the samples are more pronounced after annealing: blue-violet semi-bright coloured sample surface from the *Pt anode* and dull-grey from the *Ni anode* (pictures of the samples in the *Supporting information*). The colour variation from grey to blue could be caused by a change in the thickness of the passive oxide layer, based on stainless steel tempering colours and oxide growth theory [113]. Optical microscopy and SEM observations show that the sample produced with *Ni anode* (Figure 3.1c) has more cracks than the *Pt anode* coating (Figure 3.1a). As reported in previous similar works [112, 116], the presence

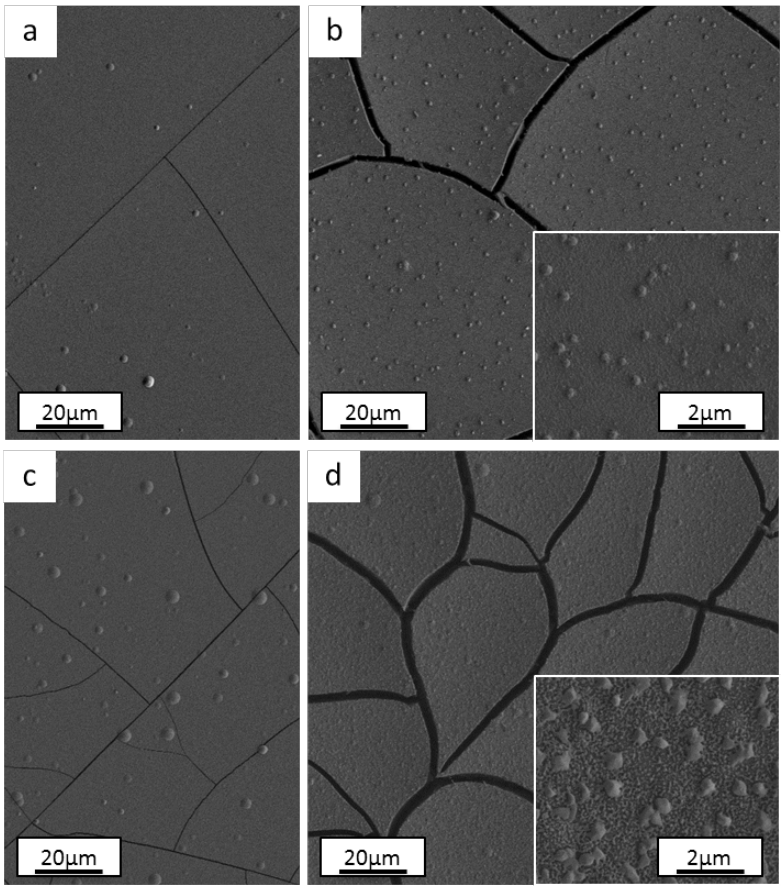

Figure 3.1 – Surface morphology of electrodeposited FeCrNi films using: *Pt anode* (a) as-deposited and (b) after thermal treatment, *Ni anode* (c) as-deposited and (d) after annealing process.

of cracks is mainly dependant on the thickness of the film (crack-free samples

obtained when coating thickness is less than 5 µm). However, crack-free coatings (thickness $\leq$ 5 µm) started to crack immediately or a few days after deposition, when the chromium content in the coating exceeded a certain amount (Cr $\geq$ 28 wt%). This behaviour seems consistent with the incorporation mechanism of chromium hydrides within Cr(III)-based electrodeposited alloys [48]. High overpotentials (therefore increase in pH) result in the formation and incorporation of chromium hydrides (hexagonal close-packed, hcp), which are unstable and decompose into metallic chromium (body-centered cubic, bcc). This crystal phase transformation leads to approx. 15% volume shrinkage and, in turn, crack formation. The annealed samples confirm the above-mentioned mechanism. In fact, SEM observations for both *Pt anode* (Figure 3.1b) and *Ni anode* (Figure 3.1d) thermally treated samples show larger cracks with respect to the as-deposited counterparts. At high temperatures, unstable chromium hydrides easily decompose to metallic chromium, therefore producing more cracks. The FeCrNi electrodeposits present nodule-like features, which are undistinguishable in terms of composition with respect to the smooth surface, as observed in our previous work [116]. Nevertheless, the difference in anode does not particularly affect the surface morphology of the studied coatings.

3.1.2 Crystal structure

Ex-situ Bragg-Brentano XRD measurements of the electrodeposited FeCrNi for *Pt anode* (Figure 3.2a) and *Ni anode* (Figure 3.2b) cases are shown in Figure 3.2, both as-deposited and annealed under an Ar controlled atmosphere. Diffraction peaks at $2\theta \approx$ 38, 69 and 82 ° correspond to face-centered cubic fcc Au (111), Si (100) and fcc Au (222) crystal planes (substrate contributions), respectively. The XRD diffractogram for the as-deposited *Pt anode* coating presents a very broad 2θ peak at approx. 45 °, which highlights that the amorphous state has a tendency towards (110) reflection of the bcc α–Fe structure. In contrast, the as-deposited *Ni anode* film shows a narrower peak in the same position as previously stated, revealing an ultrafine-grained α–Fe material with a calculated crystallite size of approx. 5 nm. The annealed samples (*Ni anode* and *Pt anode*) possess similar diffractograms. However, there is a clear difference between the as-deposited and annealed films. The thermally treated samples are characterised by many new peaks at approx. 44, 51, 75, 91 and 95 ° corresponding to the (111), (200), (220), (113) and (222) crystal planes, respectively, which are reflections of the γ-Fe fcc phase. The mean crystallite size calculated from the most intense γ-Fe peak is in both cases in the range of 20-25 nm. Several small peaks are discernible in the diffractograms corresponding to iron oxides [117] (Fe_3O_4 - magnetite) and chromium oxide (α-Cr_2O_3 - eskolaite). Moreover, in the case of the *Pt anode* annealed coating, although the predominant crystalline structure is γ-Fe, a distinct α-Fe peak is also visible at 45 °, therefore showing that

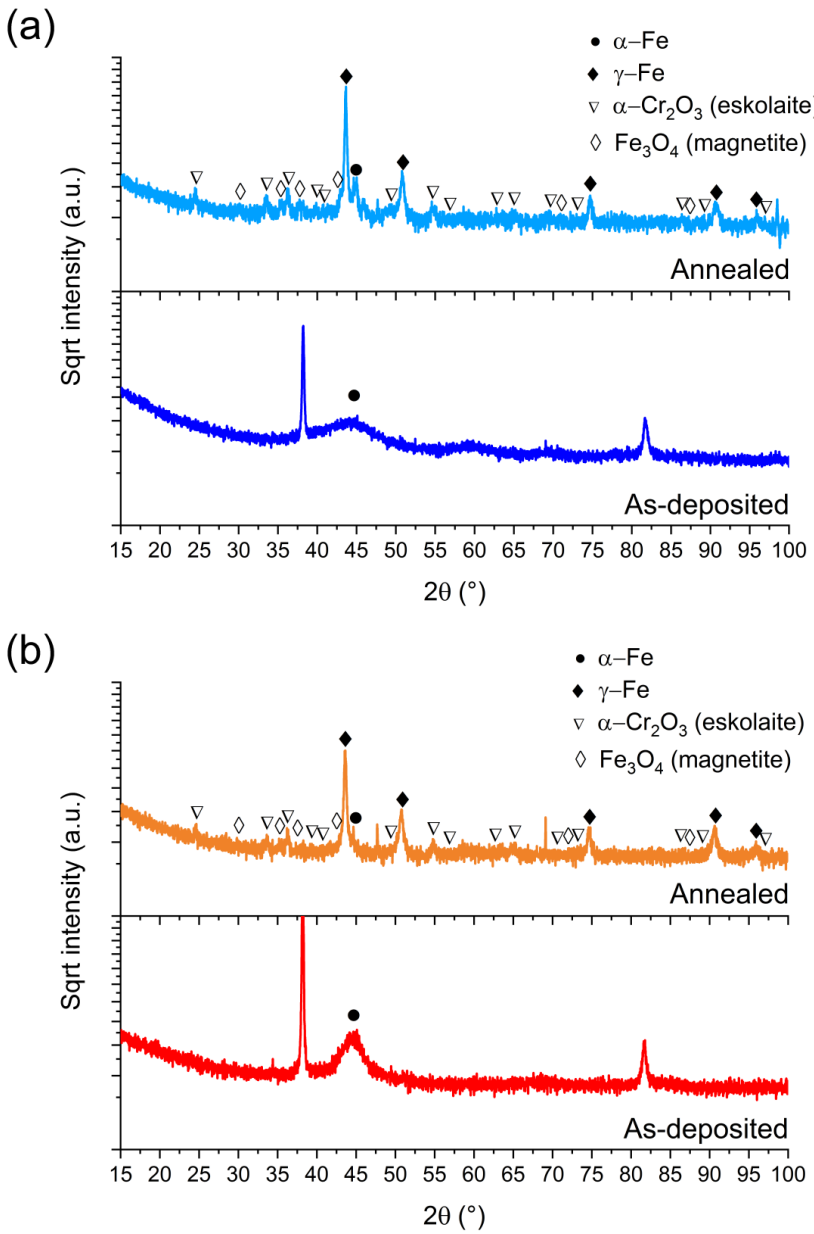

Figure 3.2 – BB-XRD measurements of FeCrNi as-deposited and annealed (Ar atmosphere, 1 h at 600 °C) electrodeposits for (a) *Pt anode* and (b) *Ni anode* coatings.

the film is a mixture of γ-Fe and α-Fe phases. The *Ni anode* annealed sample, in the other hand, does not exhibit a marked α-Fe contribution. It is worth mentioning that all diffractograms present a high background at low angles, which could be attributed to the presence of amorphous oxides. It could be expected that the higher amount of nickel (see Section 3.1.3) in the *Ni anode* samples would cause γ-Fe to be the predominant phase in the electrodeposited films (nickel retains austenitic phase in stainless steel [113]). However, from one of our studies [116], the microstructure of FeCrNi films was found not to be influenced by chromium and nickel concentrations. Therefore, the microstructure diversity is anode-dependant and most probably related to impurity variations.

3.1.3 Chemical composition, oxidation states and 3D atom-by-atom reconstructions

XRF was used to estimate the composition in wt% and current efficiency of the FeCrNi electrodeposited coatings. When a platinum anode was used (*Pt anode* case), the composition of the resulting coating was Fe57-Cr28-Ni15 (6.2% current efficiency, C.E.), whereas Fe52-Cr26-Ni22 (C.E. 8.3%) films were obtained from using a nickel anode (*Ni anode* case). The higher nickel content in the latter is most probably caused by higher amounts of nickel ions being released in the electrolyte during anode oxidation throughout the deposition process.

The elemental compositions in at% for all samples (*Pt anode*, *Ni anode*: as-deposited, annealed) including both metallic species (Fe, Cr and Ni) and impurities (O, C and N) were evaluated by means of XPS and are depicted in Table 3.1, both outer surface and in-depth (achieved by sputtering for overall 50 min) of the samples. In the same table, H content ratios with respect to the total metal species obtained from He-ERDA are also listed (the content inside the coating was determined after 20 min of Ar sputtering). The unsputtered surfaces of both as-deposited films are rich in oxygen and carbon, with relatively low metal species contributions, except for the *Ni anode* film, where 10.2 at% Fe was measured. The amount of oxygen in-depth of the coating is relatively large regardless of the anode type used (more than 15 at%). The nitrogen concentration is very low and close to the detection sensitivity limit of the XPS instruments ($\approx$ 1 at%), suggesting that there is no direct incorporation of Cr(III)-glycine complexes or uncomplexed glycine molecules inside the coating. As expected, the carbon content is more pronounced for the *Pt anode* film ($\approx$ 16 at%), whereas for the *Ni anode* coating it reaches 4 at%. Interestingly, the ratio of hydrogen to total metal atoms is quite large (above 12 at%), and slightly higher for the *Pt anode* derived sample. In contrast, annealed coatings exhibit lower amounts of both carbon and hydrogen in-depth of the film (at the expenses of oxygen and chromium, which at% content increase). Iron and nickel composition variation

Table 3.1 – Elemental composition of Fe-Cr-Ni-O-C-N (XPS) and of H (He-ERDA) of as-deposited and annealed electrodeposited FeCrNi using platinum and nickel anodes, analysed both on the surface and in-depth of the coatings.

Sample		Fe (at%)	Cr (at%)	Ni (at%)	O (at%)	C (at%)	N (at%)	H (at%)/metals
Pt anode as-deposited	Surface	3.2	2.7	0.2	36.4	56.2	1.3	-
	In-depth	37.8	15.8	11.7	16.8	16.4	1.5	16.0
Ni anode as-deposited	Surface	10.2	2.6	3.2	49.7	33.3	1.0	-
	In-depth	35.2	15.5	21.0	22.2	4.2	1.9	12.0
Pt anode annealed	In-depth	36.0	23.3	10.3	22.0	6.5	1.9	3.7
Ni anode annealed	In-depth	26.5	24.7	14.6	32.6	0.8	0.8	0.1

is thought to be linked with diffusion mechanisms and the elemental transformation of compounds due to the high temperatures involved in the annealing process. Moreover, the composition is not perfectly homogeneous across the thickness of the coatings, especially in the case of the *Ni anode* (variation of chromium peaks intensity and oxidation states in Figure 3.3b and d). The carbon content is reduced by approx. three times with respect to the as-deposited counterparts and the hydrogen-to-metals ratio is below 4 at% for the *Pt anode* film and undetectable for the *Ni anode* sample. Thus, it appears that the majority of hydrogen (and some carbons) incorporated within the coatings are weakly bonded and diffuse and outgas upon annealing. Moreover, not only the large carbon concentration, but also the high amount of incorporated hydrogen is responsible for the amorphous character of as-deposited FeCrNi films. Detailed information about the oxidation states of the different elements from XPS spectra can be found in the *Supporting information*. Overall, the fitting results of both *Pt anode* and *Ni anode* as-deposited coatings are very similar in terms of binding energies (BE) of the deconvoluted bands. The surface is mainly characterised by carbon and oxygen contribution, with little amounts of chromium oxide and hydroxide (respectively, $2p_{3/2}$ BEs at 576.2 and 577 eV; Figure 3.3a surface), as well as traces of iron in the oxide phase in the *Pt anode* film. Similar results were obtained for the *Ni anode* film (little chromium oxide; Figure 3.3b surface), however, with a more intense iron oxide contribution with respect to the previous case. The elemental evolution from surface to depth shows that iron and nickel are mainly in metallic state, regardless of anode type. Interestingly, the clear carbon C 1s peak at around 282.5 eV could be associated with chromium carbide (*e.g.* Cr_3C_2) [118]. However, it is rather difficult to distinguish between the oxides, carbides and nitrides from the chromium fitting, as their spectral lines are close together. For this reason and as the XRD diffractograms do not show any presence of carbides, it seems more accurate to refer to the fitted peaks as

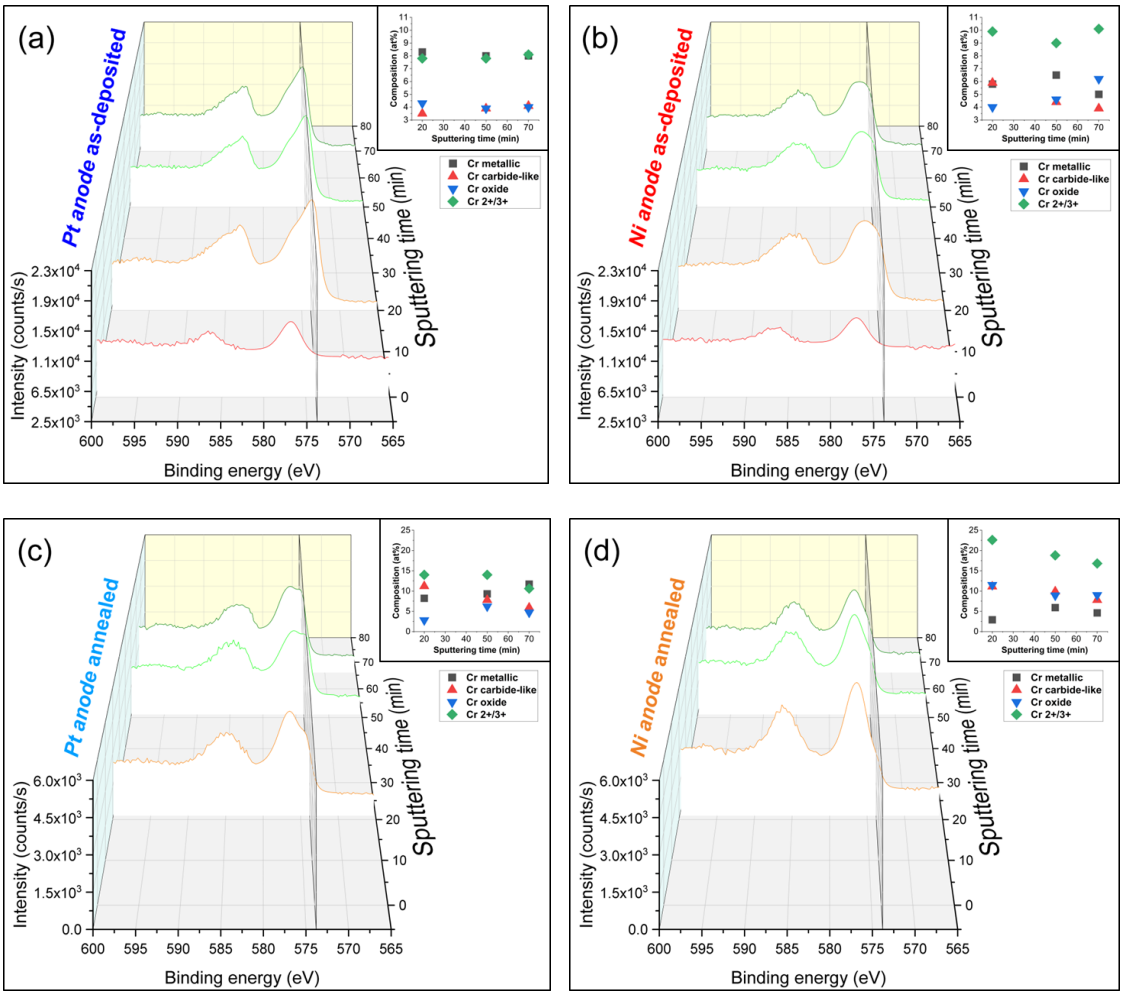

Figure 3.3 – Cr 2p XPS spectra in-depth profiling (0 to 70 min sputtering time) of electrodeposited FeCrNi with corresponding oxidation states composition graphs: *Pt anode* (a) as-deposited and (b) annealed coatings, *Ni anode* (c) as-deposited and (d) annealed. Secondary plane at 573.4 eV corresponds to chromium metallic peak.

chromium carbide-like (Cr-C) for chromium and carbide-like for carbon. Nevertheless, chromium has a rather constant distribution along the depth of the coating for the *Pt anode* film (Figure 3.3a in-depth), *i.e.* a larger metallic phase with respect to both oxide and carbide-like contributions. For the *Ni anode* coating (Figure 3.3b in-depth) the peaks' intensity for metallic chromium is lower compared to the overall oxidation state contribution ($Cr^{2+/3+}$). For some elements, annealing led to a variation in the oxidation states as a function of the coatings' depth. For the *Ni anode* film, if the nickel content is not affected by thermal treatment (likewise in the *Pt anode* sample), then iron exhibits a rise in the oxide to metallic ratio. After annealing, chromium shows an increase in total contribution (oxide plus carbide-like) with respect to the metallic one (Figure 3.3c and d in-depth) for both anode cases. Additionally, when observing other signals (C 1s and O 1s), the thermally treated films show a decrease in carbide-like state in carbon from 12.5 to 6.0 at% for the *Pt anode* coating and from 3.9 to 0.5 at% for the *Ni anode* one. Simultaneously, an increase in chromium oxide contribution in oxygen is observed from 12.4 to 16.7 at% for the *Pt anode* film and from 15.8 to 26.1 at% for the *Ni anode* sample (Table A.1 in the *Supporting information*.). These results show that annealing in general enhances chromium oxide transformation, due to the rather large amount of oxygen present in the coating, especially in the case of the *Ni anode*.

Additionally, APT was performed, resulting in 3D elemental reconstructions of nanometre tips for electrodeposited FeCrNi films. The as-deposited samples from both *Pt anode* (Figure 3.4a) and *Ni anode* (Figure 3.5a) seem to have a similar homogeneous elemental distribution. Statistical analysis of the collected data produced some clustering, as depicted in the renderings (Figure 3.4b and 3.5b). The magenta-coloured clusters (30% concentrated isosurfaces) are most probably chromium oxide (termed Cr-O). Except for a large cluster on the topmost part of the *Pt anode* as-deposited case (passive oxide layer at the surface of the film), these Cr-O clusters are infrequent and not uniformly distributed within both case tips. Instead, low concentration (2% isosurfaces) precipitates are heterogeneously distributed within the material (dark-gold colour) corresponding to a mass-over-charge peak identified and labelled as CO_2H_2 (more generally a carboxyl molecule). Based on the atom maps (Figure 3.4c and 3.5c), it appears that all the analysed elements have no preferential distribution along the tips (except for the top most part in the *Pt anode* as-deposited film). The data from FeCrNi annealed films gives a more complex reconstruction (Figure 3.6a and 3.7a) than from as-deposited ones. Isosurface renderings from clustering analysis (Figure 3.6b and 3.7b) show that Cr-O regions are phase separating (30% concentrated isosurfaces) in a convoluted pattern inside the material. These Cr-O clusters have a chemical microstructure region size of around 20-25 nm. CO_2H_2 precipitates are also present in both annealed samples with a slightly

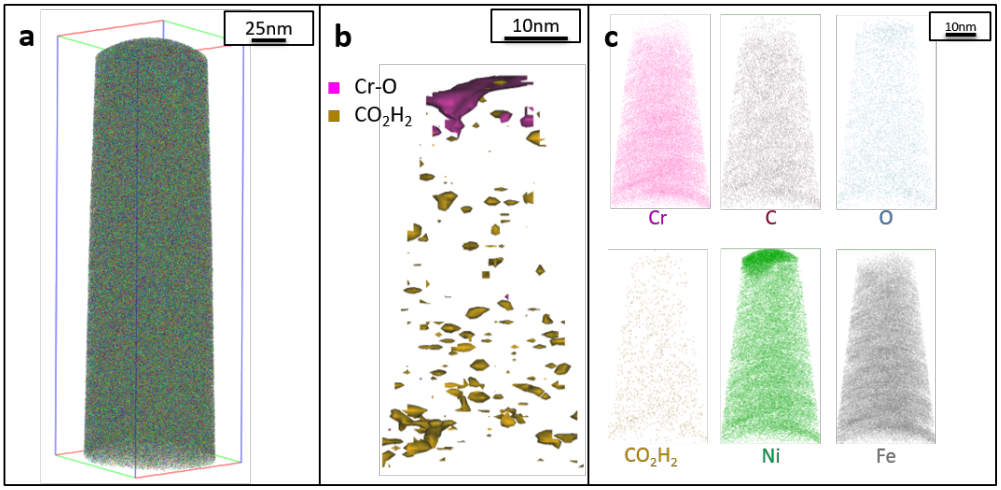

Figure 3.4 – APT results of the FeCrNi tip sample from the *Pt anode* as-deposited coating: (a) 3D elemental reconstruction, (b) isosurface rendering of Cr-O and CO_2H_2 compounds and (c) atom maps for different elements/compounds.

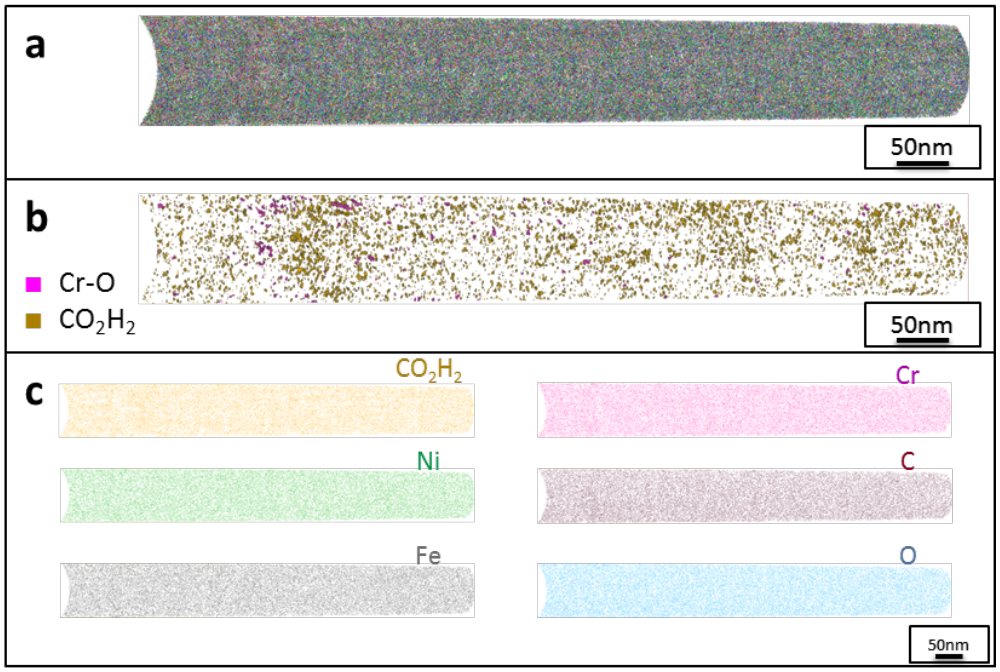

Figure 3.5 – APT results of the FeCrNi tip sample from the *Ni anode* as-deposited coating: (a) 3D elemental reconstruction, (b) isosurface rendering of Cr-O and CO_2H_2 compounds and (c) atom maps for different elements/compounds.

higher concentration profile (5% isosurfaces) and are associated with the highly dense Cr-O regions. Atom maps for single elements/compounds (Figure 3.6c and 3.7c) show that some elements are correlated with each other. Carbon and oxygen rich regions follow chromium rich one in *Pt anode* film. Instead, the annealed *Ni anode* sample has an overall lower carbon concentration with re-

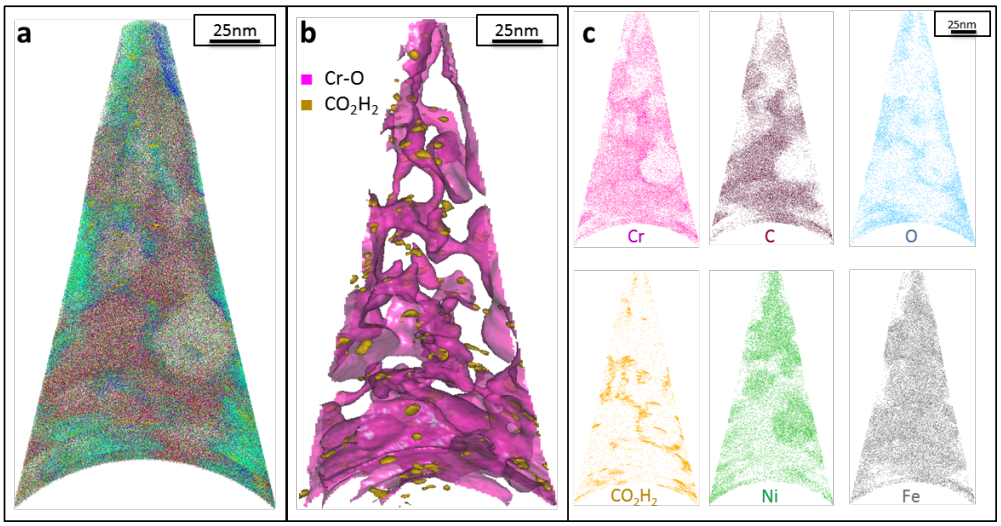

Figure 3.6 – APT results of the FeCrNi tip sample from the *Pt anode* annealed coating: (a) 3D elemental reconstruction, (b) isosurface rendering of Cr-O and CO_2H_2 compounds and (c) atom maps for different elements/compounds.

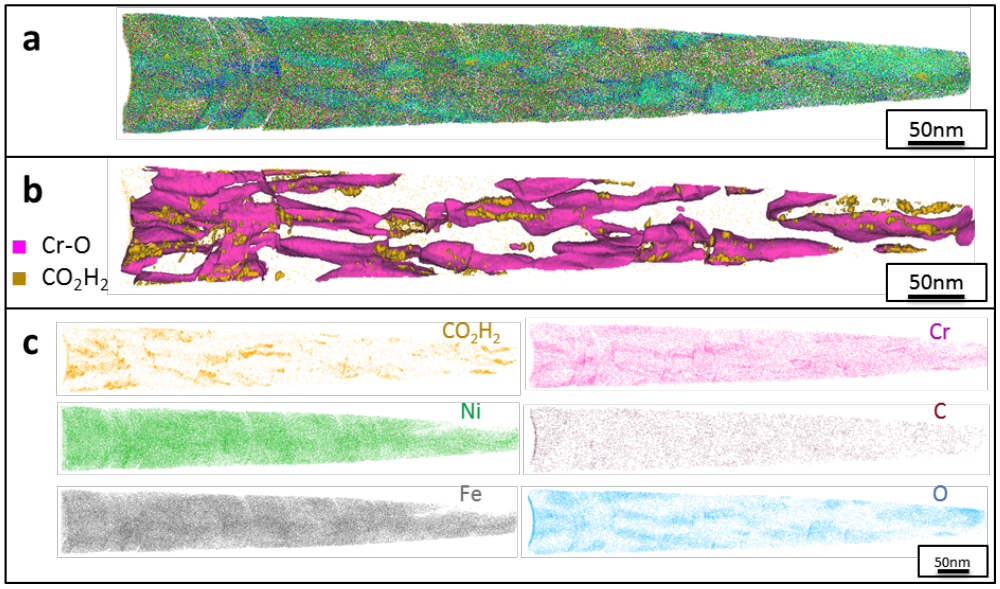

Figure 3.7 – APT results of the FeCrNi tip sample from the *Ni anode* annealed coating: (a) 3D elemental reconstruction, (b) isosurface rendering of Cr-O and CO_2H_2 compounds and (c) atom maps for different elements/compounds.

spect to the *Pt anode* counterpart and it seems not to have a preferential spatial arrangement. In both cases, CO_2H_2 is present in close proximity to chromium intense areas and at the boundaries of Cr-O clusters. Nickel and iron are not segregating, the former mainly distributed outside of the Cr-O rich zones (mainly for *Pt anode* annealed coating), whereas the latter is present rather uniformly inside the tips.

3.2 Investigation of Cr(III) complexation

3.2.1 Surface morphology

The surface of the studied samples was mainly semi-bright grey for the *Standard* and *No Cr* electrolytes. Conversely, the coating produced from the *No Cr-Glycine* bath was bright and light-grey. From both optical and scanning

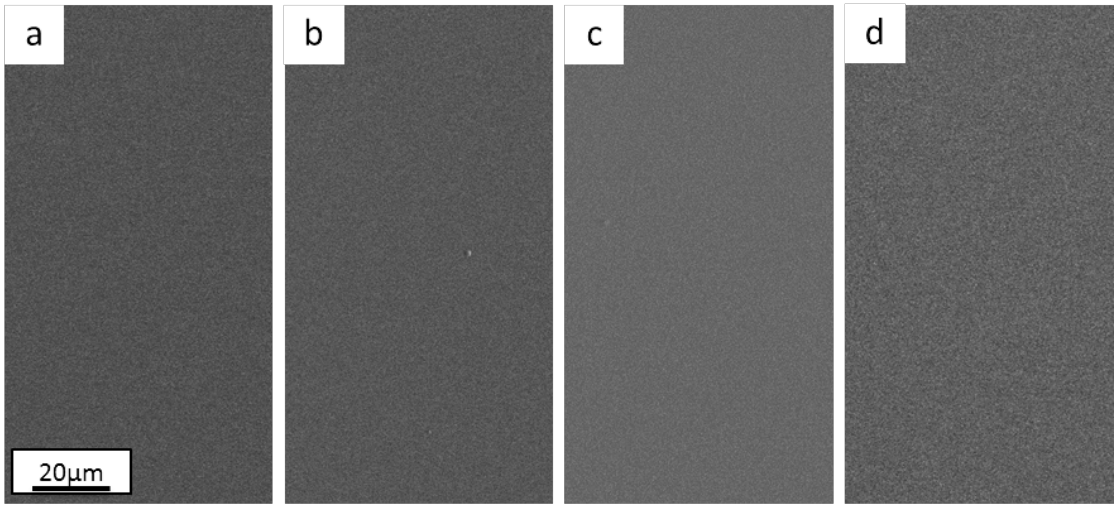

Figure 3.8 – Surface morphology of electrodeposited FeCrNi films from *Standard* electrolyte with current density of (a) -60 mA cm^{-2} and (b) -80 mA cm^{-2}, from (c) *No Cr-Glycine* bath at -80 mA cm^{-2} and from (d) *No Cr* bath at -80 mA cm^{-2}.

electron microscopy, no morphological dissimilarities were observed among the films as depicted in SEM top-view images for *Standard* (Figure 3.8a and b), *No Cr-Glycine* (Figure 3.8c), *No Cr* (Figure 3.8d) coatings. It should be noted that differently to the coatings described in Section 3.1(*Anode role investigation*), no cracks were observed. In fact, in these experiments, a lower total deposited charge was used, *i.e.* lower deposition time (see *Materials and methods*). Such behaviour is consistent with the previously mentioned crack formation mechanism.

3.2.2 Crystal structure

The crystalline structure studied by means of ex-situ Bragg-Brentano XRD measurements of FeCrNi electrodeposits is depicted in Figure 3.9a for the *No Cr-Glycine* film and in Figure 3.9b for the *No Cr* sample. The visible peaks at 2θ of 38, 69 and 82 ° are linked to fcc Au (111), Si (100) and fcc Au (222) crystal planes (substrate contributions), respectively. The diffractograms for the *Standard* electrolyte samples are the same as for the as-deposited *Pt anode* coating in section 3.1: the lack of peaks or a very broad hump at approx. 45 ° demonstrates that the material is amorphous with a tendency to form α–Fe phases. When neither chromium nor glycine are present in the electrolyte (*No Cr-Glycine* so-

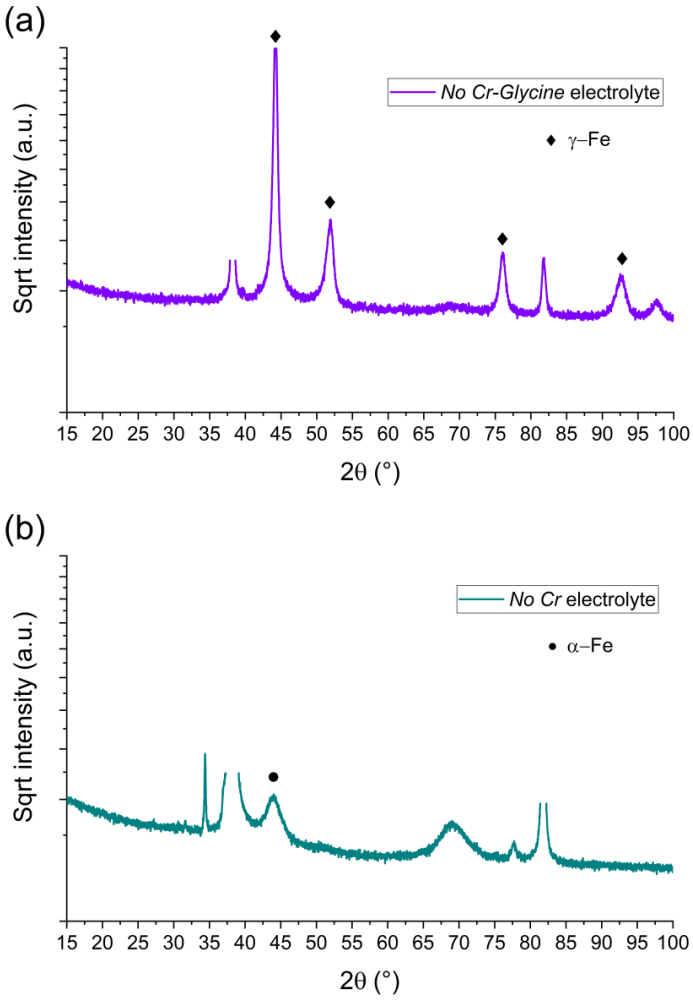

Figure 3.9 – BB-XRD measurements of FeCrNi electrodeposits from (a) No Cr-Glycine and (b) No Cr electrolytes.

lution), therefore without chromium content in the final coating, the XRD plot (Figure 3.9a) clearly shows that the material is γ-Fe (2θ peaks at 44, 52, 76 and 92 °) with an estimated mean crystallite size of 16 nm. Interestingly, the coating obtained from the electrolyte containing glycine and without chromium (*No Cr* bath), shows a crystalline structure similar to ultrafine-grained FeCrNi films (Figure 3.9b), with a minor peak at $2\theta \approx 45$ ° corresponding to α-Fe phase and a calculated crystallite size of approx. 10 nm.

3.2.3 Chemical composition, oxidation states and speciation

XRF measurements give the Fe-Cr-Ni composition in wt% and current efficiency of the electrodeposited samples depending on the electrolytes: *Standard* bath samples for -60 and -80 mA/cm^2 current densities are Fe65-Cr17-Ni18 (C.E. 3.6%) and Fe58-Cr28-Ni14 (C.E. 6.9%), respectively. *No Cr-Glycine* bath coating is Fe75-Ni25 (C.E. 34.7%) and, *No Cr* bath film is Fe64-Ni36 (C.E. 3.5%).

The compositions in at% of Fe-Cr-Ni-O-C-N for the studied electrodeposits from various electrolytes were obtained via XPS in-depth of the coating (50 min sputtering time) (values listed on Table 3.2). In the same table, H atomic percentage with respect to the total metal atoms is given from He-ERDA analysis in-depth (20 min sputtering time).

Table 3.2 – Elemental composition of Fe-Cr-Ni-O-C-N (XPS) and of H (He-ERDA) of as-deposited FeCrNi electrodeposits obtained from *Standard*, *No Cr-Glycine* and *No Cr* electrolytes and analysed in-depth.

Electrolyte	i (mA cm^{-2})	Fe (at%)	Cr (at%)	Ni (at%)	O (at%)	C (at%)	N (at%)	H (at%)/metals
Standard	-60	40.9	12.7	18.1	16.2	11.2	0.9	13.8
	-80	41.3	17.1	11.9	17.2	11.1	1.4	18.2
No Cr-Glycine	-80	28.5	0.0	68.8	2.1	0.6	0.0	0.6
No Cr	-80	42.7	0.0	39.1	15.0	2.6	0.6	10.4

Standard electrolyte coatings show that increasing the current density (therefore the overpotential) from -60 to -80 mA cm^{-2} causes an increase in chromium content from 12.6 to 17.1 at%, similarly as measured by XRF. This is in agreement with previous results [116], where for high overpotentials, chromium ions are in the mixed mass/charge-transfer region differently to nickel and iron ions, which are diffusion limited. It should be noted that there are no contents variations for all the non-metallic elements with changes in current density, except for hydrogen, where the ratio to total metal species increased from 13.8 to 18.2 at%, suggesting there is a correlation between chromium deposition and hydrogen inclusion. Furthermore, removing both chromium and glycine from the electrolyte (*No Cr-Glycine* bath) causes that no impurities are incorporated in the electrodeposits (C, N and H below 1 at%), oxygen presence is very low ($\approx$ 2 at%) and there is more nickel than iron. By removing chromium and keeping glycine in the electrolyte (*No Cr bath*), the composition of the obtained film completely changes: iron content is again higher than nickel, oxygen and hydrogen ($\approx$ 10 at%) return to high atomic percentages similar to the Standard electrolyte coating, and the carbon concentration is no longer negligible ($\approx$ 3 at%). From the oxidation point of view, detailed descriptions are present in the *Supporting information*. Never-

theless, the *Standard* electrolyte cases described in this section are identical to the *Pt anode* film described in Section 3.1.3. The increase in current density mainly leads to a rise in the metallic chromium contribution. By comparing *No Cr-Glycine* and *No Cr* electrolyte coatings, it could be concluded that the addition of glycine to the bath is linked to an increase in both iron metallic and oxide contributions, together with a significant decrease in nickel content.

To better understand the possible reactions taking place inside the electrolyte, as well as the speciation/complexation of metal ions obtained from both chemical equilibrium diagrams and UV-vis absorbance spectra, additional literature on acid dissociation and formation/stability constants has been reviewed (see *Supporting information*).

3.3 Discussion

In this work, a comparison among FeCrNi coatings electrodeposited from a Cr(III)-glycine bath was pursued by using inert platinum and pure nickel anodes. The use of a nickel anode (*Ni anode*) reduces the amount of carbon incorporation, confirming that glycine reactions at the anode are hindered by nickel preferential oxidation to Ni(II) ions. In terms of microstructure of as-deposited coatings, the *Pt anode* sample is amorphous whereas the *Ni anode* coating is ultrafine-grained. The three-fold decrease in carbon content in the latter can be related to the amorphisation process, similarly as mentioned in a previous work from our group [112] on FeCrNi coatings: glycine oxidises at the platinum anode, producing mainly formaldehyde and formic acid, which are sources of carbon atoms incorporated interstitially within the film, leading to an amorphous microstructure. However, the deposition mechanism of both chromium and impurities in that work was not clear. In the present research, carbon XPS spectra show a peak in the C 1s signal, which can be associated with chromium carbide. However, as the peaks corresponding to oxides, carbides and nitrides are near each other, it is impossible to completely rule out other possible contributions. A photo-emission study of the interaction of chromium with polymers containing carbonyl groups (*i.e.* C=O) states the formation of Cr-C carbide-like bonds, with a visible peak at 283 eV in the C 1s signal [119], similarly as in the outcome of this work. For this reason, carbide-like terminology has been used. Furthermore, the chromium to carbon stoichiometric ratio (Cr:C) was evaluated for the carbide-like fitted contributions (see *Supporting information*). In the as-deposited coatings, the high amount of carbon atoms linked to chromium (*e.g.* Cr:C 1:3 for *Pt anode* sample) is not consistent with the presence of carbides (*i.e.* Cr_3C_2, Cr_7C_3, $Cr_{23}C_6$). This fact seems correlated with carbon and carbon moieties (*i.e.* carboxyl groups) being in supersaturated state, probably bonded to chromium and to other molecules such as chromium oxide. After thermal annealing, the Cr:C stoichiometric ratio increases in both anode cases, however,

XRD diffractograms and APT results do not show any evidence towards the presence of carbides. From comparing as-deposited and annealed coatings, it was observed that C and H contents decreased after thermal treatment in all samples. This strengthens the concept that some of the carbon within the coating is linked directly to hydrogen, possibly in a carboxyl manner. The presence of iron oxides after annealing is confirmed by both XRD and XPS. However, diffractograms show a low signal-to-noise ratio, associated with the amorphous nature of the coatings. Moreover, the chromium oxide phase is most probably present in amorphous state within the film or too small, therefore not detected *via* XRD measurements. FeCrNi electrodeposits can be seen as either completely amorphous (as-deposited) or nanocrystalline with an amorphous background (after annealing). Additionally, from APT measurements, results of as-deposited coatings suggest that all the elements in the film are randomly space-distributed (identical results for different analysed sections of the film), with the exception of carboxyl molecules (labelled as CO_2H_2) which seem to be directly incorporated within the film as a 'precipitate'. Depending on the used anode, the two studied coatings have very similar APT outcomes, except for the lower carbon concentration for the *Ni anode* film. APT reconstructions of the annealed samples illustrate more interesting details about the FeCrNi electrodeposits at the nano-scale, which were not possible to observe from microscopic XPS measurements of the coatings' bulk. Cr-O isosurfaces show a complex chromium oxide pattern, which has a chemical region size in the same range as the estimated mean crystallite size using XRD. These Cr-O isosurfaces are associated with carboxyl precipitates (also detected in the as-deposited films). Based on atom maps, there is a clear correlation between C, O and Cr rich regions, as well as Cr-O clusters. In terms of elemental uniformity of the annealed coatings, APT data depict that homogeneity is not maintained at the nano-scale. However, analysis performed at different sections of the same analysed sample always show identical distributions, demonstrating that the annealed coating is reasonably uniform at the micro-scale. In summary, as a result of anode investigations *via* XRD, XPS and APT, it can be stated that using a platinum anode leads to the oxidation of glycine, probably into formaldehyde (CH_2O), next formic acid (HCOOH), followed by the direct incorporation of a certain amount of carboxyl molecules into the coating. It was observed that it is possible to avoid/decrease glycine-anode reactions by using a nickel anode. This was confirmed by surface morphology variations between the produced coatings. Chemical analyses indicate that carbon and carbon-based moieties contents decrease when using a nickel anode. Moreover, heat treatment leads to different kinetics. Firstly, the diffusion of impurities, *i.e.* carbon, oxygen and carboxyl precipitates, within the deposit (probably directly incorporated during the plating) distribute in close proximity to chromium/chromium oxide rich regions at grain boundaries. Secondly, annealing seems to be also responsible for the outgassing of carboxyl

and -H compounds weakly bonded to chromium. However, this does not fully explain the chemical reactions and the mechanisms responsible for the amorphous structure of electrodeposited FeCrNi.

The study of Cr(III)-glycine complexation shows that both Cr(III) and glycine electrolyte addition strongly influence the composition variation and microstructural changes of the electrodeposited FeCrNi films. Based on the collected XPS data, it can be seen that an increase in chromium content (*Standard* electrolytes) is linked to higher hydrogen incorporation within the coatings, with no other metal or impurity (C and N) content variations. This demonstrates that the reduction of complexed Cr(III) is influenced by a hydroxides and/or hydrides deposition process [42, 48] and probably without direct glycine incorporation, due to low nitrogen content. XRD diffractograms show that the samples are amorphous, as expected from the first part of this study. By comparing the two chromium-free baths, it can be observed that the absence of glycine (*No Cr-Glycine* electrolyte) leads to an impurity-free NiFe coating with very low O content and a high current efficiency (C.E. $\approx$ 35%). The FeNi electrodeposited film obtained from the electrolyte containing glycine (*No Cr* electrolyte) is characterised by a low C.E. (less than 4%), is rich in O and H, but contains low amounts of carbon. In the first case (NiFe film), the higher amount of nickel is due to a much larger Ni ions concentration within the bath with respect to Fe (Ni:Fe molar ratio > 5), even though iron-nickel is a well-known anomalous co-deposition system. However, the main result is the influence of uncomplexed glycine inside the bath. Glycine did not seem directly responsible for impurity incorporation. However, its presence or, more probably, the presence of its by-products (*i.e.* formaldehyde, formic acid and/or carboxyl group molecules) clearly favours metal hydroxides formation and incorporation. Moreover, competing hydroxides/hydrides reduction processes decrease the efficiency of FeCrNi alloy electrodeposition. XRD results show that without glycine in the bath (NiFe coating without impurities) the film is nanocrystalline, and by adding glycine into the electrolyte (FeNi coating with high hydrogen and oxygen contents and low amount of carbon) the material tends to become amorphous again. Atomic weights in terms of oxidation state (Table A.2 in the *Supporting information*) depicts that role of glycine as an intermediate for impurity incorporation. By comparing the resulting coatings from the *No Cr* and *No Cr-Glycine* electrolytes, it can be seen that the addition of glycine significantly increases the iron metallic contribution, while simultaneously increase the H and O contents within the produced film.

Based on the literature and on the results from speciation/complexation studies (see *Supporting information*), Cr(III) is complexed with glycine in the FeCrNi *Standard* bath as verified by UV-vis absorbance spectra. Moreover, in the absence of Cr(III) and glycine in the electrolyte (*No Cr-Glycine*), iron and nickel ions are almost certainly following the anomalous co-deposition via the hydroxides mechanism [39, 40]. When glycine is added (*No Cr* electrolyte), the most probable

and stable glycine complex to be present in the bulk electrolyte is Ni(II)-glycine (confirmed by chemical equilibrium diagrams). However, due to the presumably higher local pH near the cathode surface, the presence of carboxylate and hydroxo ions can strongly affect the metals' complexation. Fe(II)-complex molecules possess a greater tendency to substitution reactions due to their lower stability with respect to Ni(II)-glycine molecules. This explains the increase in iron deposition with respect to nickel even when the Ni:Fe molar ratio is greater than 5. The amorphous/ultrafine-grained microstructure may be linked to the high hydrogen, oxygen and carbon contents brought about by the co-deposition of carboxylate-hydroxo complexes. Additionally, it seems that when Cr(III)-glycine complexes are present in the bath (*Standard*), the correlation between the increase in chromium concentration, as well as hydrogen and carbon contents can only be explained by an incomplete reduction at the cathode. The carboxylate groups are still attached to chromium during the electroreduction process, leading to the presence of metalorganic or organometallic compounds within the coatings.
Both *ex-situ* analyses presented in this chapter and previously reported information on the studied Cr(III)-glycine based electrolyte, allow to propose the following reactions (Figure 3.10):

- Anode glycine oxidation: in the presence of an inert anode, the oxidation of uncomplexed glycine (first into formaldehyde and later formic acid) becomes relevant.
- Cathodic reactions of Cr(III):
    1. Cr(III)-glycine to metallic chromium: a two-step mechanism with the release of glycine anions. These uncomplexed glycine molecules are free in the electrolyte and can react at the anode or with other metal ions.
    2. Cr(III)-glycine hydroxides/hydrides: the presence of strong hydrogen evolution and high local pH at the cathode favours the formation of adsorbed Cr-complex-OH (*via* hydrolysis reaction) and/or Cr-complex-H molecules at the surface.
    3. Cr(III)-glycine incomplete deposition: based on annealing results, the drastic decrease in C and H shows that these two elements are weakly bonded to Cr or CrOx (most probably *via* a carboxyl group). More precisely, incomplete glycine molecules form weak carbide-like and nitride-like bonds with chromium molecules. High temperatures destabilise both carboxyl and –H weak bonds, which are then released from the Cr compound and free to outgas from the film.
- Carboxyl group incorporation: direct inclusion from the electrolyte as precipitate.

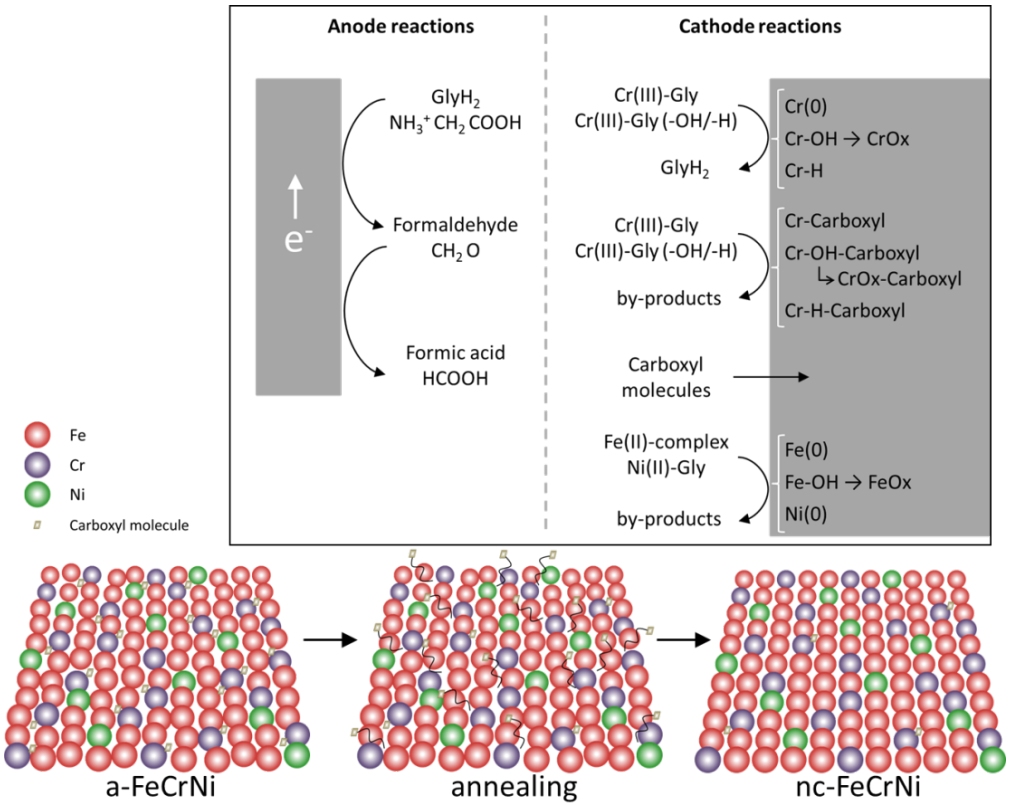

Figure 3.10 – Proposed mechanisms in Cr(III)-glycine -based FeCrNi electrodeposition: (top) anodic/cathodic reactions and (bottom) illustration of microstructural variations due to annealing.

- Cathodic reactions of Fe(II) and Ni(II): anomalous co-deposition is enhanced due to the high stability of complexed Ni(II)-glycine and to the fact that Fe(II) ions have a higher tendency to be complexed by carboxylate/hydroxo ions.

It can be concluded that the studied material is in fact a composite. Considering the *Standard* FeCrNi electrodeposition (aqueous FeCrNi Cr(III)-glycine electrolyte and using a platinum anode), the as-deposited coating is composed of the following phases/species:

- a matrix of metallic FeCrNi - 59 at% (Fe63-Cr17-Ni20)
- organometallic compounds - 19 at% (Cr16-O26-C47-N11)
- chromium oxide - 10 at% and iron oxide - 10 at%
- carboxyl compounds (C-C and C-H) 2 at%

3.4 Summary

The electrodeposition of FeCrNi from a 'green' Cr(III)-glycine based electrolyte was investigated. Electroreduction mechanisms were proposed correlating microstructural and composition variations. The anode affects the impurity content and, in turn, the crystallinity. Amorphous and significantly contaminated (high C and H contents) coatings were obtained when using an inert platinum anode, whereas using a nickel anode provided ultrafine-grained films with a lower impurity content. Annealing at 600 °C produced nanocrystalline gamma-Fe coatings (estimated mean crystallite size $\approx$ 20-25 nm) with substantially decreased carbon and hydrogen contents, showing that these elements are weakly bonded within the material and released during thermal processing. Additional analysis by varying the bath composition depicts that both Cr(III) and glycine are responsible for the large quantity of impurities. First, glycine oxidises at the anode and forms carboxyl group molecules, such as formic acid. These by-products, together with a local pH increase at the cathode, are the major factors for side-reactions, direct carboxyl moieties inclusion and lower deposition efficiency. Moreover, substantial impurity incorporation (C 11 at% and H 18 at%) in the presence of Cr(III)-glycine complexes suggests that this electrodeposition process can undergo:

- an incomplete metal-complex reduction, leading to carboxyl molecules weakly bonded to chromium and chromium oxide present within the film,
- Cr-hydroxides/hydrides: formation, adsorption on the cathode's surface and inclusion within the coating.

Impurities from these processes are the main contributor to film amorphisation. Complexation/speciation studies confirm trivalent chromium is complexed with glycine. Additionally, both Ni(II)-glycine stability and the tendency of Fe(II) to form carboxyl/hydroxo complexes, enhances anomalous Fe-Ni co-deposition. Cr(III)-glycine FeCrNi electroreduction mechanisms were also verified by comparing the as-deposited and thermally treated samples using XPS and APT. The electrodeposits were a mixture of Fe, Cr, Ni, as well as large quantities of chromium oxide, hydrogen, carbon and carbon-based impurities. Films obtained using a nickel anode exhibited lower carbon and carboxyl moieties contents than when using a platinum anode. Further annealing demonstrated that CrOx preferentially segregated at the grain boundaries and was associated to carbon-based precipitates. In conclusion, the as-deposited material can be considered a composite, mainly formed by a metallic matrix (Fe-Cr-Ni) containing homogeneously distributed chromium organometallic compounds, oxides (CrOx and FeOx) and carboxyl molecules.

4 FeCrNi from aqueous electrolyte: role of chromium content on material properties

In the previous chapter (Chapter 3), we investigated the electrochemical mechanisms involved in FeCrNi Cr(III)-glycine electrodeposition system and how composition (*i.e.* metals and impurities) was correlated with morphology and microstructure of the films. Even though impurities can play an important role on the final material properties, in stainless steel-like alloys, chromium content is generally considered as the primary factor determining the corrosion resistance (Cr > 10 wt%) as well as other relevant properties.

In this chapter, a series of electrodeposition experiments are carried out at various current densities with the same *Standard* experimental set-up used previously, obtaining FeCrNi deposits with different chromium contents. These electrodeposits are then compared to standard metallurgical austenitic SS in terms of corrosion resistance, bio-compatibility and magnetic response.

Declaration of contribution
In this work, Enrico Bertero fabricated part of the electrodeposited samples, performed part of the anodic LSV and magnetic VSM tests, characterised the samples using SEM and XRF, performed tribological measurements and contributed to data analysis and writing to a great extent. Madoka Hasegawa (Empa - Thun) produced part of the electrodeposited samples, performed part of the anodic LSV and contributed partially to data analysis and writing. Samuel Staubli and Inge K. Hermann (Empa - St. Gallen) performed the cytotoxicity tests. Eva Pellicer and Jordi Sort (UAB - Barcelona) performed part of the magnetic measurements and provided support to the research results. Henrikas Cesiulis, Natalia Tsyntsaru and Svajus Asadauskas (VU - Vilnius) provided the infrastructure and support for tribological measurements. Johann Michler and Laetitia Philippe (Empa - Thun) supervised the work and provided the facilities to carry the work out.

Parts of this chapter use materials adapted from Bertero *et al.* [116] (Elsevier Copyright).

4.1 Chemical composition and efficiency

Fe-Ni deposition, which follows the so-called anomalous co-deposition [14], leads to less-noble iron depositing preferentially with respect to nickel, even if the Ni/Fe concentration inside the bath is much larger than one (Table 2.1). However, during co-deposition of Fe-Cr-Ni in this plating system, cathodic reactions of iron and nickel ions are limited by mass-transfer. On the other hand, chromium, whose deposition potential is more negative than those of iron and nickel, is deposited in the charge-transfer limited or mixed regime. Hence, the deposition rate of chromium is highly dependent on the polarisation of the electrode (or the applied current density) while those of iron and nickel should not be affected as long as the mass-transfer state is unchanged. Thus, the chromium content in a deposit can be adjusted simply by tuning the current density.

Indeed, results from XRF measurements (Figure 4.1a) show this dependence of composition on the current density. As expected, chromium content increases from 3 to 40 wt% with an increase in the cathode current density from -50 to -100 mA cm^{-2}. This consequently leads to a decrease of iron and nickel contents from 79 to 50 wt% and from 18 to 10 wt%, respectively. It should be noted that the wt% ratio of Fe/Ni within the films essentially did not change (≈4), which agrees with the deposition mechanism described in the introduction of this chapter. At high overpotentials, iron and nickel are in the diffusion limited region, while chromium is still in the charge-transfer or mixed regime.

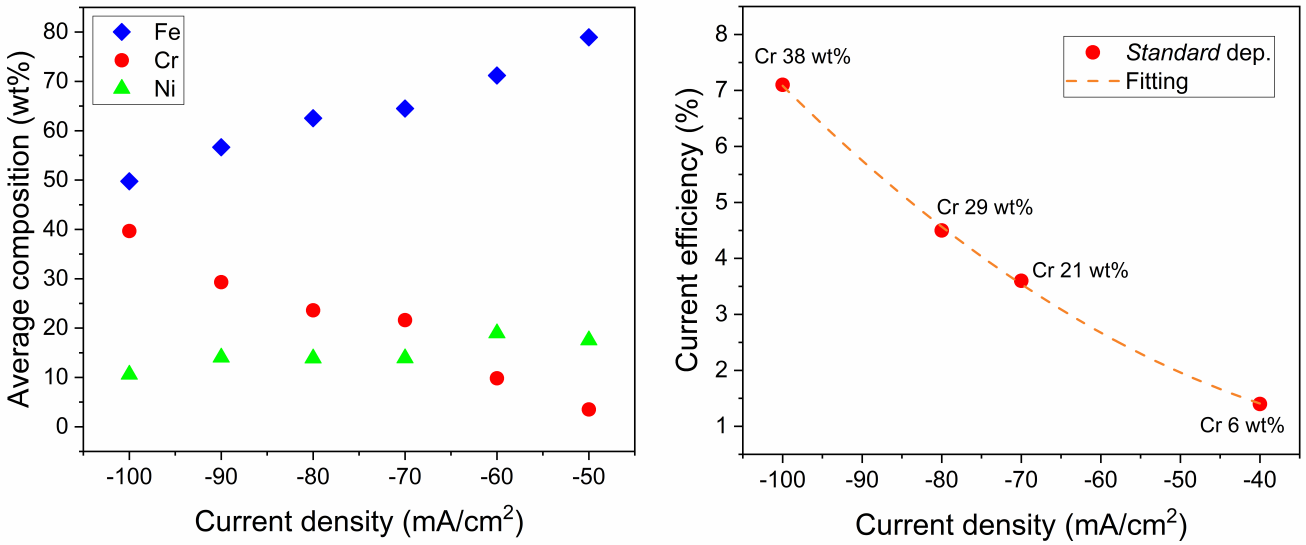

Figure 4.1 – FeCrNi electrodeposits: (a) average composition *vs.* applied current density, (b) current efficiency with respect to the current density (*i.e.* chromium content).

The current efficiency, evaluated with Farday's law, is plotted in Figure 4.1b for various FeCrNi electrodeposits *vs.* their corresponding applied current density. This plot shows how the current efficiency is augmenting with the increase of overpotential and therefore, it is correlated with the increase in chromium content. This behaviour can be explained by the fact that chromium has a high molar concentration inside the electrolyte and also because of the deposition mechanism explained earlier. Still, this graph shows also how low the current efficiency is (lower than 10 %), which means that most of the current applied during the process is used for side reactions, such as the HER.

In Chapter 3, the compositions in at% of Fe-Cr-Ni-O-C-N of some FeCrNi electrodeposits have been evaluated by XPS measurements in-depth of the coating (up to 50 min sputtering). The sample from Section 3.2 electrodeposited from a *Standard* aqueous electrolyte at -80 mA cm^{-2} (wt% from XRF: Fe58-Cr28-Ni14) is very similar in terms of deposition conditions to one of the coatings presented here within the measurement uncertainty limit, which is FeCrNi 29 wt%Cr (wt% from XRF: Fe57-Cr29-Ni14). Therefore, from XPS stoichiometric evaluation of that sample, it can be deduced that the metallic part is making up to $\approx$ 60 at% of the coating, with the following proportions: Fe63-Cr17-Ni20. Moreover, considering only Cr 2p XPS fitting, the atomic weights of the various chromium phases (with respect to the Fe-Cr-Ni-O-C-N total content) are the following: Cr metallic 10 at%, Cr carbide-like 3 at% and Cr oxide 4 at%.

4.2 Morphology

Avoiding or minimizing cracking in electrodeposited films is a challenge for chromium and its alloys, and this limits the maximum achievable thickness of the coatings. As mentioned in the previous chapter, Gabe [48] proposed that cracking is related to the incorporation of chromium hydrides (CrH and/or CrH_2), which subsequently decompose into metallic chromium and hydrogen atoms, thus resulting in shrinkage of the films. Here, cracks were observed in FeCrNi electrodeposits when the films exceeded a certain thickness (thickness > 5 µm) and/or the average chromium content was higher then 28 wt%. Such behaviour can be observed in Figure 4.2, showing top-view SEM images of 5-micrometer-thick FeCrNi films with different chromium contents. Typically, for films with higher chromium content, cracks started to appear on the film's surface after some hours or days of storage once the samples were prepared. This observation suggests structural changes in the deposits after electrodeposition, which supports the aforementioned mechanism. Therefore, in this study, films with thickness of less than 5 µm were prepared and characterised immediately afterwards for their corrosion resistance and cytotoxicity. FeCrNi films are in general rather smooth (roughness $\leq$ 200 nm), although a few nodule-like deposits were occasionally observed on the surface. The size of these nodules varies from

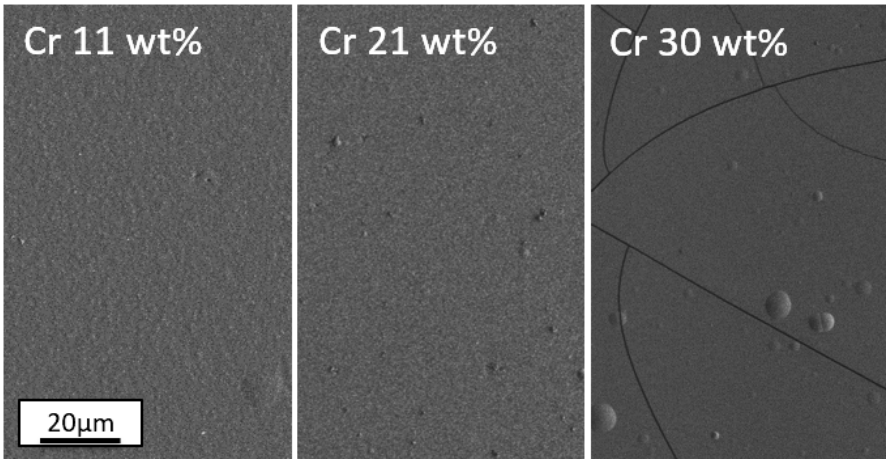

Figure 4.2 – SEM top-view images of FeCrNi electrodeposits with varying chromium content.

sub-micrometer to a few micrometers, and the number of nodules also varied among samples. While no clear relationship was observed between the nodule formation and the alloy composition, the number of nodules tends to increase with an increase of thickness, implying that nodules nucleate randomly but remain during film growth.

4.3 Crystal structure

Crystallographic structures of the FeCrNi electrodeposits with different compositions were analysed by GI-XRD (Figure 4.3). We previously reported [112] that FeCrNi deposits containing 25-30 wt% chromium are amorphous, unlike austenitic stainless steels AISI 304 and AISI 316L. In agreement with the previous result, no visible peaks were observed in any of the GI-XRD profiles of the Fe-Cr-Ni electrodeposits in the range of chromium content between 5 and 51 wt%. These results reveal that the microstructure of the FeCrNi deposits is not significantly affected by the composition, at least in the range of chromium content investigated in this study.

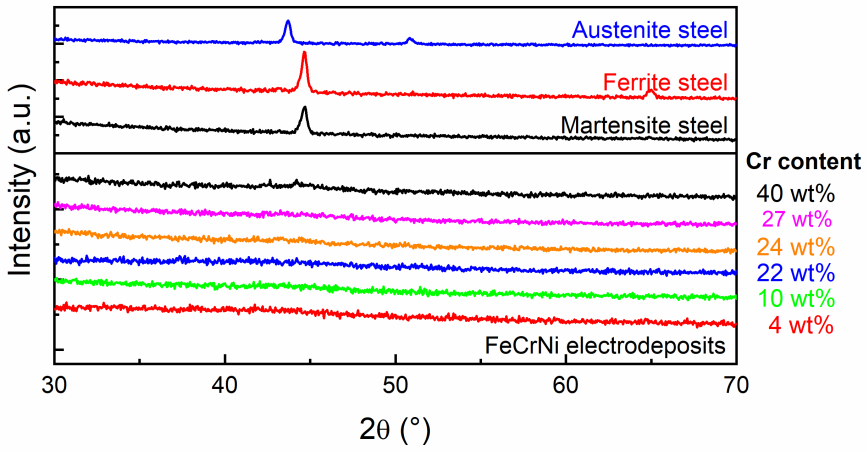

Figure 4.3 – Comparison of XRD diffractograms of FeCrNi electrodeposits with various Cr content and metallurgical steels.

4.4 Corrosion resistance

The excellent corrosion resistance of stainless steels is associated with the native surface oxide (passivation) which protects the alloy from anodic dissolution [120–122]. Extensive studies of the passivation film have shown that its composition [123], thickness [124] and microstructure [31] significantly affect the corrosion resistance. Therefore, the investigation of surface oxides, especially their formation and anodic dissolution, provides important insights into corrosion of stainless steels. Firstly, the anodic linear sweep voltammograms of the samples were measured in 0.5 M aqueous sulfuric acid. We employed a cathodic pre-treatment (or activation), which is a commonly used surface preparation method for anodic polarisation studies of stainless steels [124–127], in order to remove the native oxide layer, thereby enabling the characterization of oxide formation and its anodic dissolution during a potential sweep. The cathodic pretreatment was performed at -0.6 V *vs.* Ag/AgCl for 15 min in the test solution in order to remove the native oxide layer. The polarisation measurement was performed immediately after the pre-treatment. The polarisation curves obtained with this procedure are satisfactorily reproducible. Figure 4.4a compares the anodic polarisation curves of an electrodeposited FeCrNi film (24 wt% Cr), AISI 304 and AISI 316L. Table 4.1 lists the corrosion parameters which were extracted using Tafel plot. All polarisation curves show the typical active-passive-transpassive transition. The anodic peak for the passive oxide formation appears around -0.25 V *vs.* Ag/AgCl and the passivation plateau continues until the breakdown potential around +1.0 V *vs.* Ag/AgCl, where the transpassive formation of soluble $Cr_2O_7^-$ starts [124]. The anodic polarisation curve of an electrodeposited sample (24 wt% Cr) in the passive region is well overlapped with those of AISI 316L and AISI 304, demonstrating that the electrodeposited sample exhibits a passivation

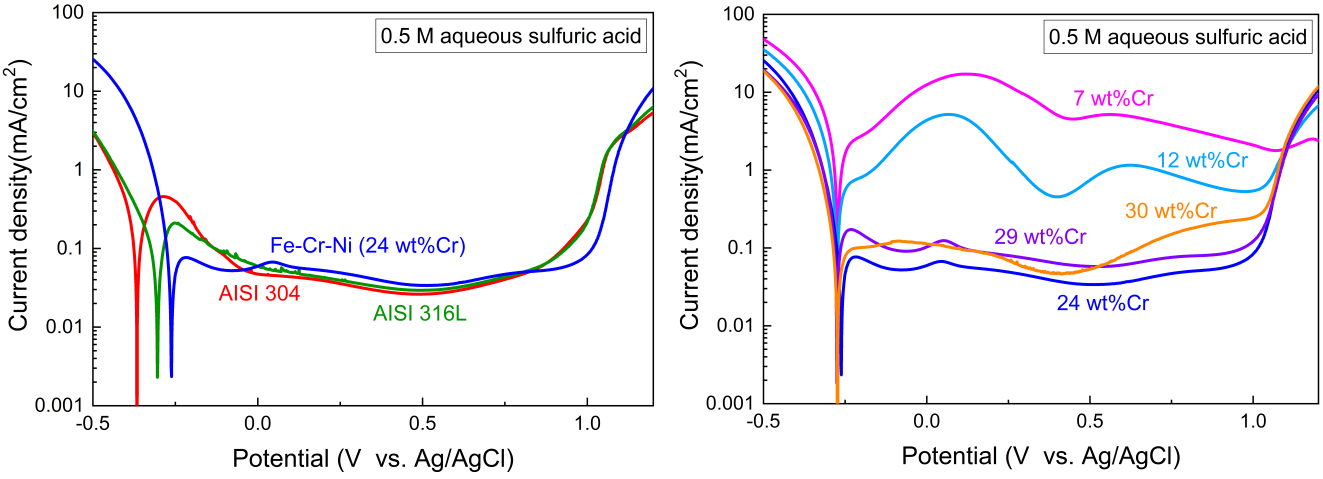

Figure 4.4 – Anodic polarisation curves (with cathodic pre-treatment) in 0.5 M H_2SO_4 aqueous solution for: (a) a FeCrNi electrodeposit and AISI steels, (b) Fe-CrNi electrodeposits with various chromium contents.

Table 4.1 – Extracted corrosion parameters from anodic LSV tests in aqueous sulfuric acid (0.5 M H_2SO_4) and biological medium (DMEM).

Sample	Solution	E_{corr} (V vs. Ag/AgCl)	i_{corr} (mA cm^{-2})
FeCrNi (Cr 24 wt%)	0.5 M H_2SO_4	-0.262	0.197
AISI 304	0.5 M H_2SO_4	-0.366	0.237
AISI 316L	0.5 M H_2SO_4	-0.304	0.102
FeCrNi (Cr 26 wt%)	DMEM	-0.416	$0.546 \cdot 10^{-3}$
AISI 304	DMEM	-0.223	$1.961 \cdot 10^{-3}$
AISI 316L	DMEM	-0.260	$1.440 \cdot 10^{-3}$

behaviour similar to those of standard austenitic stainless steels. On the other hand, some characteristic differences between the electrodeposited sample and metallurgical stainless steels are observed. Primarily, the cathodic part (related to hydrogen evolution) for the electrodeposited sample is significantly enhanced with respect to AISI 316L and AISI 304, and this consequently results in the positive shift of the zero-current potential. Secondly, the transpassive breakdown starts at a slightly more positive potential on the electrodeposited sample than in standard stainless steel samples. The difference in electrochemical behaviour between the electrodeposited sample and standard stainless steels is attributed to the dissimilarities in microstructure and chemical composition of the passive oxide film. In fact, electrodeposited FeCrNi is amorphous, in contrast to its metallurgical crystalline counterpart [112]. Moreover, the incorporation of hydroxides and hydrides in the coating from enhanced HER [47, 48]

results in a passive oxide layer which differs in chemical composition with respect to those of the AISI stainless steels. Figure 4.4b shows the polarisation curves for electrodeposited samples having various chromium contents. The graph reveals that chromium content significantly affects the passivation performance of electrodeposited FeCrNi. The polarisation curves of samples with 7 and 12 wt% chromium show two broad current peaks in the potential ranges between -0.2 and +0.4 V *vs.* Ag/AgCl and between +0.4 and +1.0 V *vs.* Ag/AgCl. These peaks are attributed to the formation of soluble Fe(II) and Fe(III) compounds [124], respectively. It is widely accepted that the corrosion protection is brought about by the formation of a chromic oxide matrix which stabilizes these iron species [124]. As can be seen in the graph, the current peaks in the passive region become smaller with an increase in the chromium content up to around 25 wt%, which is in agreement with the known effects of chromium on corrosion properties of stainless steels [124, 126]. The best results are obtained around this chromium content, and for the best cases (*i.e.* 24 wt% Cr, 29 wt% Cr), the polarisation curves in the passive region are very close to those of AISI 304 and AISI 316L, confirming the outstanding corrosion resistance of these coatings. Further increase in the chromium content does not provide any significant changes in passivation, inversely, it seems to slightly worsen passivity. This behaviour could be explained because of the increase in amount of carbon-based impurities incorporated in the oxide passive layer of the coating linked with the augmenting of plated chromium. As mentioned before, the amount of chromium measured by XRF is the overall weight contribution. However, in order to compare electrodeposited samples to metallurgical SS, it is better to consider only the contribution of chromium coming from the metallic phase (evaluated by XPS in at%), which is the main one affecting some materials properties such as corrosion resistance. Those results can then be seen from this prospective. In fact, the best polarisation scans are the ones from electrodeposited FeCrNi 24 wt%Cr and 29 wt%Cr. The latter is corresponding to an effective metallic chromium content of 17 at%, which is a comparable amount with respect to AISI SS.

Additionally, anodic linear sweep voltammetry tests of the samples were performed in a biological medium, namely Dulbecco's modified Eagle medium (DMEM) using the same polarisation parameters as for the acidic case, but without implementing a cathodic pre-treatment, thus maintaining the native oxide layer intact. Those measurements allowed for assessing the corrosion behavior of electrodeposited FeCrNi films in a physiological solution, which resembles a possible bio-medical application environment. Figure 4.5 compares the anodic polarisation curves of an electrodeposited FeCrNi film (26 wt% Cr), AISI 304 and AISI 316L. The extracted corrosion parameters for those samples (Table 4.1) are in agreement with results previously obtained for standard stainless steels in other physiological media [128]. Electrodeposited FeCrNi presents a lower catalytic effect on the cathodic reaction with respect to standard stainless steels,

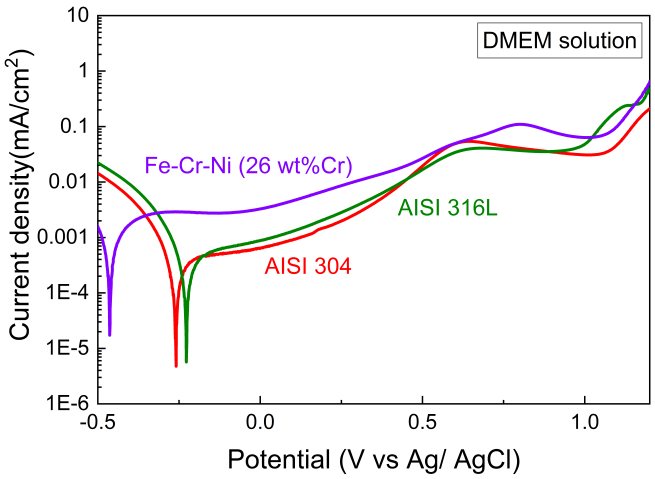

Figure 4.5 – Anodic polarisation curves (without cathodic pre-treatment) in a biological medium (DMEM) for a FeCrNi electrodeposit and AISI steels, (b) FeCrNi electrodeposits with various chromium contents.

which could explain its higher passive current in the anodic region. The absence of current spikes in the passive domain, together with visual inspection of the samples after tests, confirmed that pitting was not initiated. Moreover, the transpassive domain (starting at around +0.7 V *vs.* Ag/AgCl) is consistent with Cr(III) to Cr(VI) dissolution and water oxidation at neutral pH. In this region, the variation of current values at the plateaus can be explained by the differences of chromium dissolution among the samples: electrodeposited FeCrNi is much richer in chromium than standard austenitic stainless steels.
Overall, in the case of an acidic solution, the results of polarisation measurements of the electrodeposited samples clearly show the formation of a highly passive surface oxide film, similar to those of the standard stainless steels. Moreover, polarisation scans in a biological medium (DMEM) confirm that electrodeposited FeCrNi also presents good corrosion resistance in a physiological cell-culture environment, showing no signs of pitting.

4.5 Bio-compatibility

Regarding the potential biomedical applications of electrodeposited FeCrNi, cell adhesion and compatibility issues are imperative. Therefore, cell adhesion and morphology on electrodeposited FeCrNi samples and on commonly used austenitic stainless steels (AISI 304 and AISI 316L) were compared. Figure 4.6a-c reveals comparable cell adhesion for all three samples investigated, with no visible cell morphological differences among them. SEM micrographs (Figure 4.6d,e) further show comparable morphology and cell surface adhesion between AISI 316L stainless steel (Figure 4.6e) and electrodeposited FeCrNi (Figure 4.6d) sam-

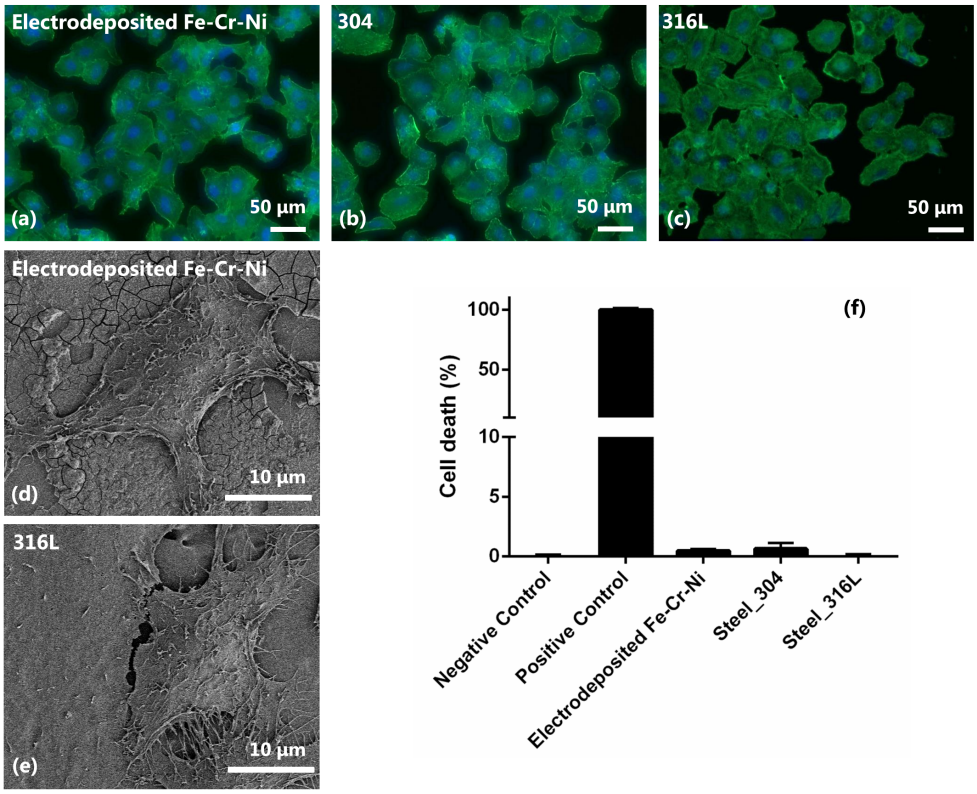

Figure 4.6 – Cytotoxicity tests with lactate dehydrogenase assay for electrodeposited FeCrNi, AISI 304 and 316L samples.

ples. Cell compatibility was confirmed by quantifying lactate dehydrogenase (LDH) release into the medium (Figure 4.6f). LDH is released in response to membrane damage and is a sensitive marker for cytotoxicity. Again, there is no difference between the various samples and cell death is comparable to the negative control (no steel, sample with cells only).

4.6 Magnetic behaviour

Contrary to the non-magnetic character of conventional (*i.e.* crystalline) austenitic steels, the electrodeposited amorphous-like FeCrNi films are ferromagnetic. Representative hysteresis loops of the various investigated coatings, measured along the in-plane direction, are shown in Figure 4.7a. All films exhibit a soft ferromagnetic behaviour, with coercivity values in the range 5 to 40 Oe and saturation magnetisation (M_S), which decreases linearly with respect to Cr wt% (see Figure 4.7b). For a chromium content exceeding approx. 30 wt%, the electrodeposited alloys become fully non-magnetic. These results are in agreement with previous studies on FeCr -based metallic glasses [129, 130], where the dilution of iron with chromium was reported to lead to a linear decrease of the overall magnetisation due to a decrease of the Fe-Fe exchange interactions [130], which were also manifested, in a reduction of the Curie temperature. Additionally, the Fe-Cr exchange interactions are known to be antiferromagnetic [129], hence additionally contributing to the decrease of M_S. Overall, our results reveal that by varying the current density during electrodeposition the magnetic response of electrodeposited FeCrNi alloys can be highly tailored, as occurs in other electrochemical systems, such as CuNi [131]. This is an interesting result for the potential implementation of this type of coating in magnetically-actuated micro- and nano-electro-mechanical systems (MEMS/NEMS).

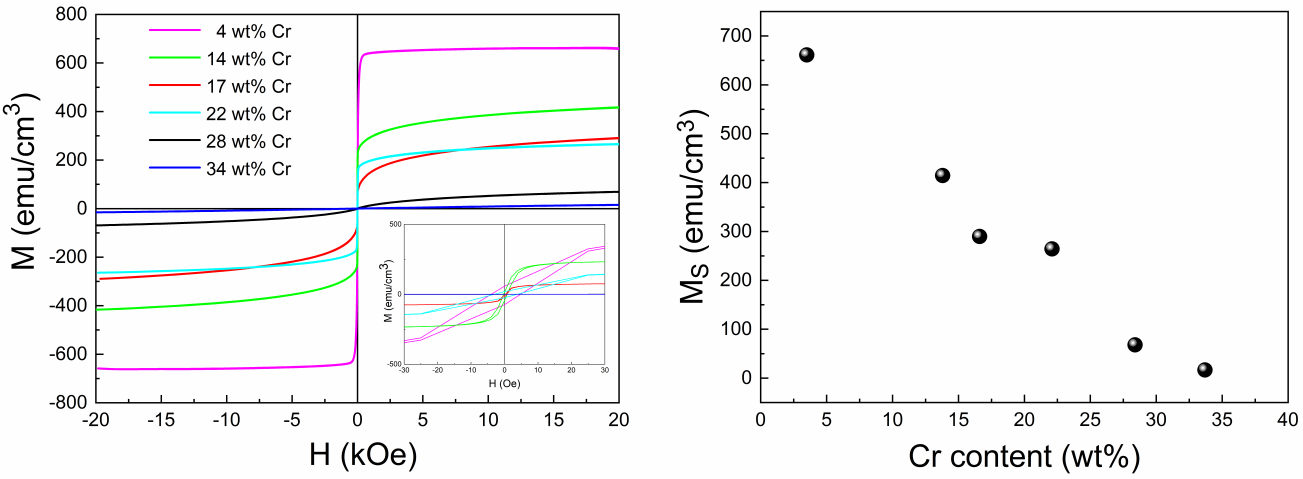

(a) (b)

Figure 4.7 – (a) Hysteresis loops corresponding to the electrodeposited FeCrNi coatings with different chromium contents, measured at room temperature; (b) dependence of the saturation magnetisation of the coatings as a function of the chromium content.

4.7 Tribological properties

Tribological tests using a corundum ball in linear sliding mode (dry friction condition) were performed on metallurgical AISI SS and on electrodeposited FeCrNi coatings with various chromium content. SEM-EDX after tribological measurements indicated no sign of aluminium traces on the tracks and no wear was found from optical inspection of the corundum ball. SEM top-view images after these tests show the wear tracks of the different analysed samples (Figure 4.8) . For metallurgical SS the tracks are rather large and uniform, whereas all electrodeposited FeCrNi coatings (*e.g.* FeCrNi Cr 32 wt% in Figure 4.8) present a narrower track but clear sign of big ruptures of the coating.

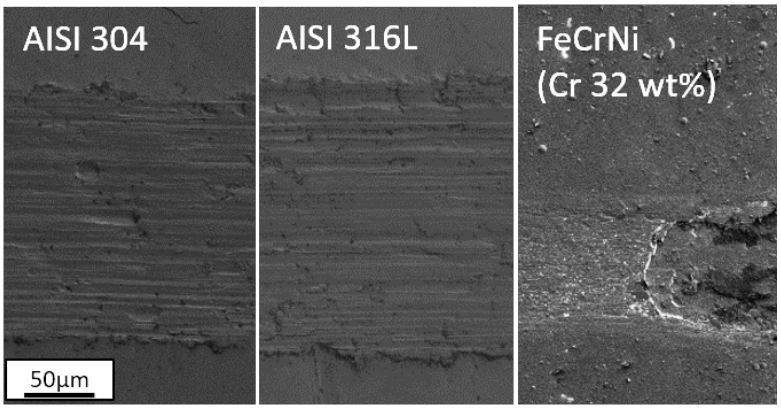

Figure 4.8 – SEM top-view images showing the wear tracks after tribological tests for AISI 304, AISI 316L and an electrodeposited FeCrNi coating (*i.e.* in this case FeCrNi with chromium 32 wt%).

A diamond tip profilometer was used prior tribological measurements to retrieve the surface mean roughness (R_a) of the various samples (Table 4.2). These values are consistent with the fact that AISI samples were polished and mirror-like (as-received by the company), at the contrary of electrodeposited FeCrNi coatings which were analysed as-deposited.

Table 4.2 – Surface mean roughness of AISI 304, AISI 316L and electrodeposited FeCrNi (average), measured by using a diamond tip profilometer.

Sample	R_a (nm)
AISI 304	93
AISI 316L	41
FeCrNi (average)	222

After the tests, the profilometer was also employed to obtain surface profiles perpendicular to the wear tracks, which are depicted in Figure 4.9. AISI 304

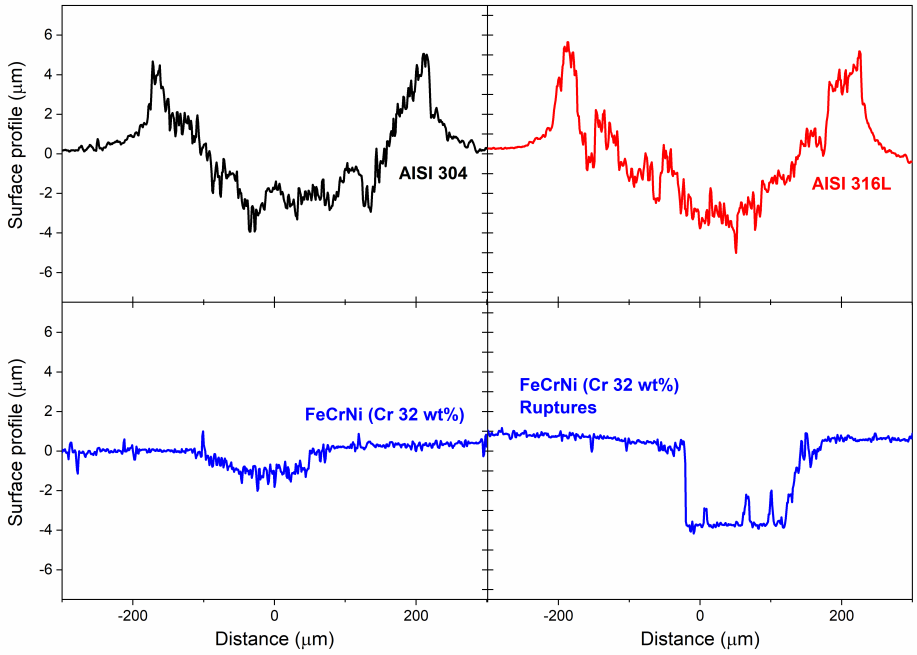

Figure 4.9 – Surface profiles perpendicular to the wear tracks after tribological tests for AISI 304 (top left), AISI 316L (top right) and electrodeposited FeCrNi coatings (in this case FeCrNi with chromium 32 wt%) with (bottom right) / without (bottom left) the presence of ruptures.

and 316L samples have similar behaviour. The centre deep parts of the tracks (called groove) have a depth (measured from the flat surface of the sample to the bottom of trench) of approximately 5 μm and they are rather jagged, which is correlated with high abrasive wear due to the presence of more debris. While the external parts of the wear tracks form high piles-up, which means the material has a high ductility (typical of steels having an austenitic phase such as AISI 304 and 316L). At the contrary, surface profiles of electrodeposited FeCrNi coatings, in Figure 4.9 FeCrNi Cr 32 wt%, show that the wear track groove is less deep and jagged without formation of piles-up, meaning the coatings suffer in a minor way of abrasive wear and they are not ductile (the coatings are all amorphous). In fact, there are ruptures of the coatings in some parts of the wear tracks that confirm the electrodeposited material is more brittle.

Additionally, from the tribological tests it was possible to extrapolated the friction coefficients (μ) of the various tested samples at normal load (F_N) of 5 N, which were then plotted *vs.* the number of performed cycles (Figure 4.10). For AISI SS, the initial stage of the tests (first few cycles) is characterised by a fast increase in μ reaching peaks of more than 1, for then decreasing slowly afterwards, presenting also stick-slip phenomena (before 30 cycles). Instead, all electrodeposited FeCrNi deposits have an initial μ of $\approx$ 0.3, which does not change drastically, but

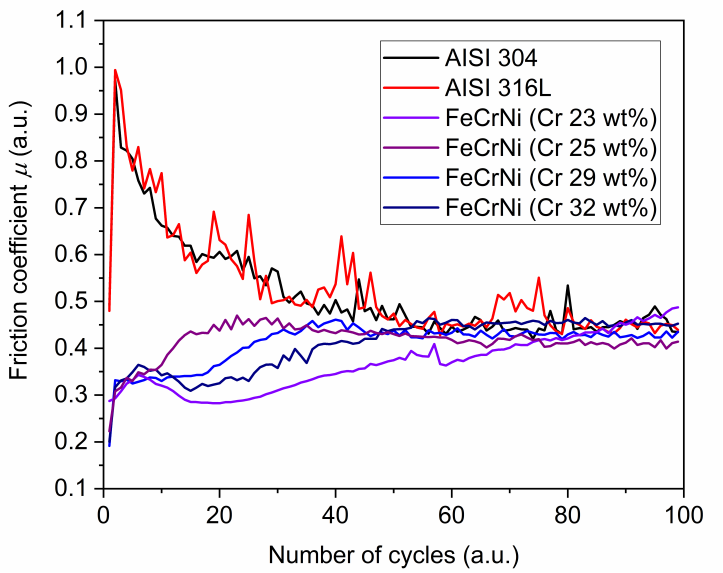

Figure 4.10 – Friction coefficient *vs.* number of cycles plotted for AISI 304, AISI 316L and electrodeposited FeCrNi coatings with different chromium content, during tribological tests performed at normal load of 5 N.

increase very slowly during the experiment. These facts can be explained by the rather low surface roughness of AISI samples with respect to more 'rough' electrodeposited FeCrNi ones. After 40 cycles, a stationary regime is reached for all samples, with μ being between 0.4 and 0.5, which shows that both austenitic metallurgical SS and electrodeposited FeCrNi coatings have a comparable tribological behaviour.

4.8 Summary

Amorphous FeCrNi thin films with various chromium contents were prepared by electrodeposition from an all-aqueous Cr(III)-based electrolyte.
The anodic LSV experiments demonstrated that:

- In aqueous sulfuric acid solution, electrodeposited FeCrNi films with a chromium content of 24 wt% and 29 wt% (effective metallic Cr 17 at%) exhibit an excellent passivation behavior, which resembles that of AISI 304 and AISI 316L austenitic SS.
- In the same acidic media, electrodeposited films with more than 24 wt% chromium show passivation currents below 0.07 mA cm^{-2} and a large and stable passive electrochemical window (-0.5 to +1.0 V *vs.* Ag/AgCl).
- In a biological medium, electrodeposited samples present good corrosion resistance compared to standard SS, without incurring pitting in such a physiological environment.

Cytotoxicity tests with the lactate dehydrogenase assay revealed that:

- Electrodeposited FeCrNi exhibits low cytotoxicity (cell death below 0.7%), comparable to that of AISI 304 and AISI 316L.

Unlike AISI 304 and AISI 316L, which are non-magnetic, electrodeposited FeCrNi alloys exhibit soft-magnetic properties:

- Saturation magnetisation of electrodeposits linearly decreases from 662 emu cm^{-3} to zero with an increase in chromium content from 4 to 34 wt%.

Nevertheless, tribological measurements showed the under-study material is rather brittle compared to metallurgical austenitic SS. Moreover, deposition efficiency is very low, which means that the HER and other side-reactions are dominant during the electroplating process.

5 FeCrNi mixed-solvent *vs.* aqueous electrolytes: coatings and micro-nanocomponents

Recently, miniaturisation trends in the high-tech industry have pushed the development of advanced bio-medical applications and therefore, the investigation for viable fabrication techniques and appropriate materials. Among the available techniques (*e.g.* 3D printing, micro-powder injection), only electroplating into micro- and nanotemplates seems promising in terms of cost, performances, time and precision [11]. However, the material choice is limited to CrCo and stainless steel based alloys (*e.g.* FeCrNi), when considering the final bio-medical requirements [132].

Electrodeposition of FeCrNi stainless steel-like coatings from a Cr(III) electrolyte has shown outstanding characteristics: high corrosion resistance, low cytotoxicity and soft-magnetic properties (Chapter 4). The combination of electrodeposition and miniaturised templates for creating FeCrNi micro and nanocomponents can revolutionise the future progress in bio-medicine and micro-robotics, for example for being used as magnetically-actuated devices for in-situ drug-delivery applications. However, the use of Cr(III) for obtaining chromium-based miniaturised devices is limited to few cases [82–84, 102] due to difficulties linked to trivalent chromium-based electrodeposition. Specifically, the electrochemical production of Cr containing binary and ternary alloy nanostructures from a Cr(III) electrolyte has not been reported so far.

Cr(III) chemistry requires rather negative applied potentials (Cr(III) $\rightarrow$ Cr(0), E^0 = -0.72 V *vs.* SHE) for the reduction of chromium ions to metallic chromium. Consequently, HER is enhanced which leads to low deposition efficiencies [46, 47, 54]. This is the limiting factor for growing thick FeCrNi films without stresses and porosity issues, making the deposition into high AR moulds challenging and, in turn, also the creation of micro- and nanostructures.

In Chapter 3, the use of Cr(III) and a complexing agent (*i.e.* glycine) in the electrodeposition of FeCrNi ternary alloy has been thoroughly investigated. From this study, it has been possible to understand the various mechanisms involved in such complex Cr(III)-based system, which mainly lead to incorporation of impurities and variation in the microstructure. It must be noted however, that the incorporation of impurities (*i.e.* C and H) by using an organic complexing agent was unavoidable and HER was still predominant. These factors significantly lowered the deposition efficiency and caused the material to become brittle and

porous, especially for longer depositions (Chapter 4). This made very difficult to achieve thick films and to obtain miniaturised structures *via* template-assisted electrodeposition.

In this chapter, the aim is to investigate an alternative pathway to electrodeposit FeCrNi into miniaturised templates still employing a 'green' Cr(III)-based electrolyte. The idea was to use a mixed-solvent electrolyte in which not only water would be employed, but another solvent would have been added to the solution. This was considered because of the well-known drawbacks of Cr(III) chemistry in aqueous solutions (*e.g* side-reactions, low deposition efficiency and hydrogen embrittlement due to HER and local pH increase). The use of non-aqueous solvent was thought could be beneficial for decreasing these effects. Some studies are present in literature confirming the improvement in deposition efficiency of electrodeposited metals/alloys (containing also chromium) by using non-aqueous solvents or mixed solutions [138–141]. For these reasons, a mixed-solvent electrolyte comprising ethylene glycol (EG) was found to be the most suitable solution. Among many other tested solvents, EG showed very good miscibility with the studied FeCrNi aqueous electrolyte and preliminary electrodeposition results depicted a good morphology of the coatings, although, further investigations were needed.
In this study, FeCrNi films obtained from both mixed-solvent and aqueous electrolytes are studied and compared in terms of: Cr(III) complexation inside the various electrolytes by means of UV-vis spectrophotometry, reduction of species *via* LSV, kinetics governing the studied electrolytes using a RDE set-up, composition of the coatings (namely, metals and impurities) using both XPS and ERDA, and deposition efficiency using XRF data. For the first time, the electrodeposition of FeCrNi nanostructures from both a mixed-solvent and aqueous solutions into AAO membranes is reported. In case of the mixed-solvent 30 vol% EG electrolyte and depending on the applied current density, either NWs and/or NTs are obtained. The investigation of such nanostructures is performed using SEM to determine filling ratio and morphology, together with EDX analysis. The outcome of this study is then compared to pre-existing kinetic models of metal ions deposited into nanotemplates and a possible explanation concerning the growth mechanisms during FeCrNi ternary alloy electrodeposition inside nanoporous AAO templates is given. Additionally, UV-LIGA process is used to electrodeposit FeCrNi into micro-moulds. By employing a mixed-solvent electrolyte and a CV-like deposition, it is possible to successfully obtain FeCrNi micro-pillars, while circumventing the frequently observed detachment of the photoresist.

Declaration of contribution

In this work, Enrico Bertero produced the samples (films and micro-nanostructures), characterised part of them using SEM, performed UV-vis spectroscopy, XRF, XRD and XPS characterisations, and contributed to most of the data analysis and writing. Cristina V. Manzano (Empa - Thun) produced the AAO templates and dissolved the template after deposition, performed part of the SEM and EDX analysis, and contributed partly to data analysis and writing. Gerhard Bürki (Empa - Thun) performed HR-SEM and EDX analysis on the samples. Max Döbeli (ETH - Zurich) performed He ERDA measurements. Stefano Mischler (EPFL - Lausanne) provided support on electrochemical characterisations and RDE experiments. Laetitia Philippe (Empa - Thun) supervised the work and provided the necessary facilities for its progress.

Parts of this chapter use materials adapted from Bertero *et al.* [142] (Elsevier Copyright).

5.1 Comparison of aqueous and mixed-solvent electrolytes

5.1.1 UV-vis absorption spectra

The UV-Vis absorption measurements were performed for freshly prepared FeCrNi electrolytes with different concentration of solvents and their spectra were compared (Figure 5.1). All electrolytes show peaks at λ_1 = 580 nm and λ_2 = 410 nm, indicating Cr(III) is complexed with glycine as similarly stated in previous literature results [115, 143, 144]. Complexation of chromium to glycine is essen-

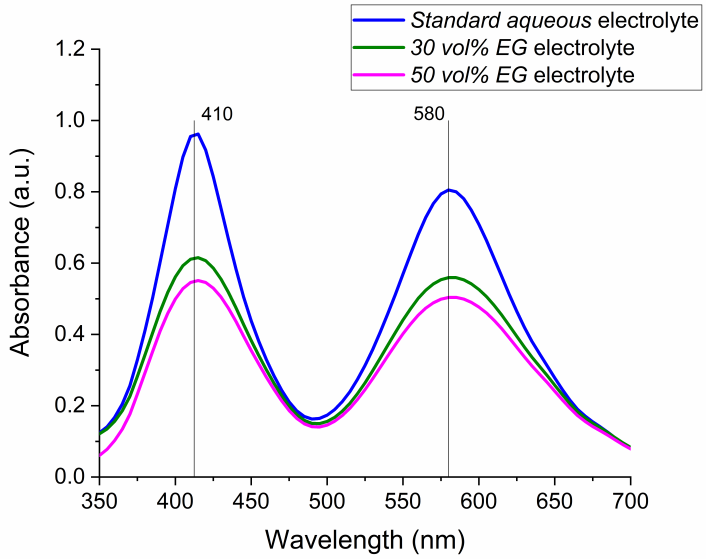

Figure 5.1 – UV-Vis spectra of various freshly prepared FeCrNi electrolytes (mixed-solvent and aqueous) diluted 10 times in the corresponding solvent (theoretical Cr(III)-glycine concentration of 0.04 M).

tial for promoting Cr(III) electroreduction at the cathode, otherwise Cr(III) aqua complexes would be favoured and no metallic deposition is achieved. In this case, the use of EG in the FeCrNi electrolyte seems not to affect too much Cr(III)-glycine complexation, which has identical peaks position for all cases, showing that EG-based electrolytes are also favourable for deposition. Upon increasing the amount of EG from 0 vol% (*Standard aqueous* electrolyte) to 30 vol% (*30 vol%* electrolyte) and then to 50 vol% (*50 vol%* electrolyte), the intensity of absorption decreases. This can be due to two concurrent factors. First, the interaction between EG and water molecules modifies the solvent surrounding Cr(III)-glycine compounds, consequently changing the intensity of light absorbed by such complexes [145]. At the same time, other Cr(III)-EG complexes are likely to be formed in the solution (for Cr(III)-EG logβ = -0.45 and for Cr(III)-EG(OH) logβ = 1.17 [146]) explaining the decrease in intensity for the Cr(III)-glycine peaks when EG volume in the electrolyte is increased.

5.1.2 Linear sweep voltammetry (LSV)

LSV have been used to retrieve the reduction potentials for the elements involved in the electrodeposition process (*i.e.* Fe, Cr, Ni) among the different analysed electrolytes. From Figure 5.2, it can be seen that both FeCrNi *Standard aqueous* and *30 vol% EG* mixed-solvent solutions have similar reduction peak positions: (a) at -0.67 V *vs.* Ag/AgCl corresponding to Ni(II) to Ni(0) (E^0 = -0.25 V *vs.* SHE), (b) at -0.89 V *vs.* Ag/AgCl corresponding to Fe(II) to Fe(0) (E^0 = -0.44 V vs. SHE) and (c) at -1.14 V *vs.* Ag/AgCl corresponding most likely to the first reduction step of complexed chromium (Cr(III)-glycine) from Cr(III) to Cr(II) (E^0 = -0.42 V *vs.* SHE). The second reduction potential of chromium is probably hidden by the higher current consuming concurrent HER. From these LSV results,

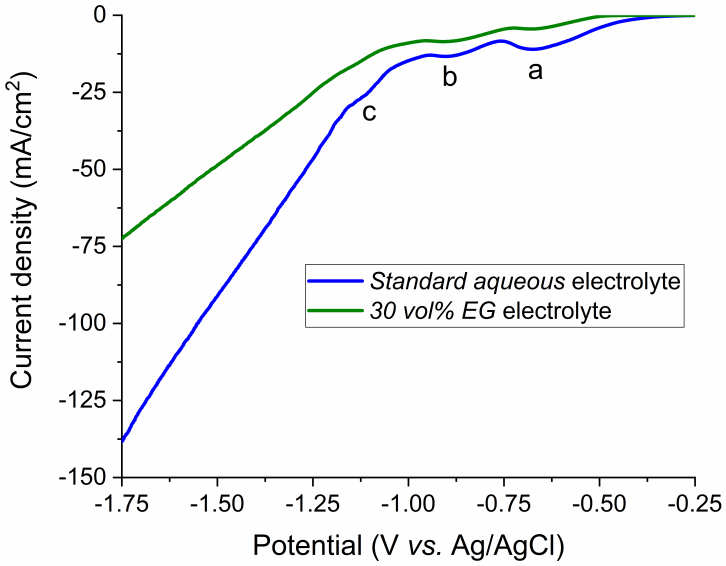

Figure 5.2 – LSV potentioscans on flat Au substrates from FeCrNi electrolytes: *Standard aqueous* and mixed-solvent *30 vol% EG*.

it is noticeable that for the same applied potential (*i.e.* FeCrNi $E_{dep} \approx$ -1.5 V *vs.* Ag/AgCl), the corresponding "consumed" current is lower for the mixed-solvent case with respect to the aqueous FeCrNi electrolyte counterpart. This already provides evidence that for the mixed-solvent solution, the HER is less active, consuming less current during the electroreduction processes at the cathode.

5.1.3 RDE experiments

A RDE allows to have controlled hydrodynamic conditions at the electrode surface. In this way, at high rotation speeds, the diffusion layer thickness is well-defined, as well as the equations governing mass transport by diffusion and convection. The concentration profile is described by Nernst diffusion layer model: close to the electrode surface (distance lower then the diffusion layer thickness

δ) mass transport is diffusion-controlled and the concentration is linearly dependent on the distance from the electrode, whereas, when convection is prevalent, concentration becomes constant and independent on the distance from the electrode.
Here, a RDE set-up has been used to record LSV potentioscans for both studied electrolytes and to understand better the kinetics dominating in such systems. For both *Standard aqueous* and *Mixed-solvent EG* electrolytes, LSV scans at different rotation rates, in Figure 5.3a and Figure 5.4a, show the electrochemical behaviour of species at the cathode, even though the reduction peaks are not completely visible. As stated beforehand, iron and nickel reduction processes are starting at relatively low applied potentials (< |-0.9| V *vs.* Ag/AgCl). At higher applied voltage (> |-0.9| V *vs.* Ag/AgCl), those two elements are in the diffusion-limited region. In this region, the increase of current with applied potential depicts that chromium is still in the charge-transfer limited or mixed region, also that HER is concurrently occurring at the cathode. Decreasing further the potential (> |-1.25| V *vs.* Ag/AgCl), a plateau of the current is becoming more visible, which corresponds to chromium species being mass transport limited by diffusion. However, the strong concurrent HER does not make this plateau clear enough.

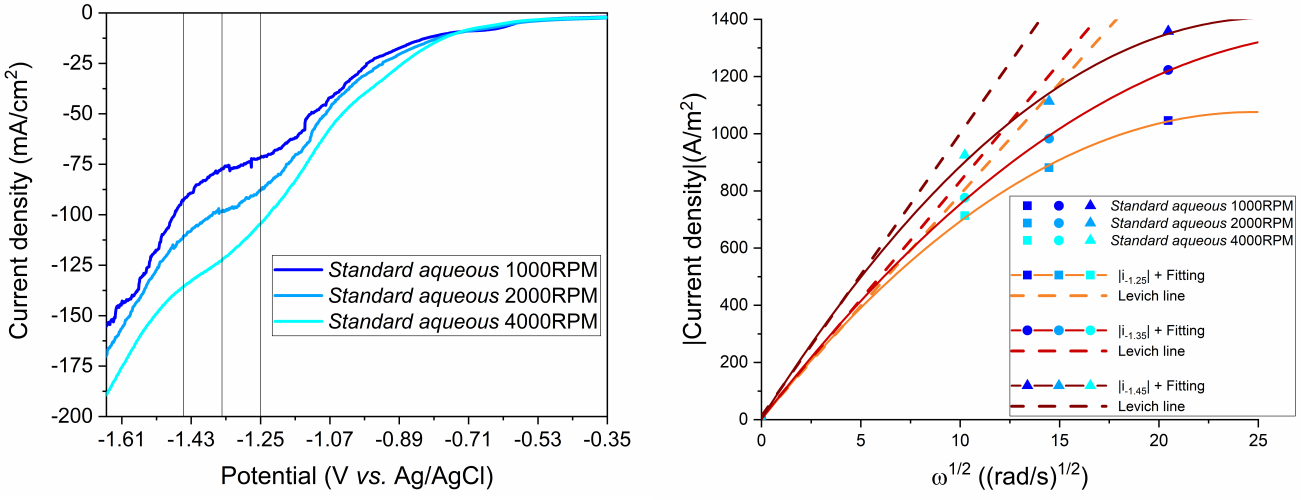

(a) (b)

Figure 5.3 – Measurements using a RDE set-up for the *Standard aqueous* FeCrNi electrolyte: (a) LSV potentioscans at various rotation speeds and (b) Koutecký-Levich fitting taken at fixed potentials (-1.25, -1.35 and -1.45 V *vs.* Ag/AgCl) with different rotation rates (1000, 2000 and 4000 RPM).

In order to retrieve some useful electrochemical information, the currents at various rotation rates taken in the approximate diffusion-limited region (at -1.25, -1.35 and -1.45 V *vs.* Ag/AgCl) were plotted against the square root of the rota-

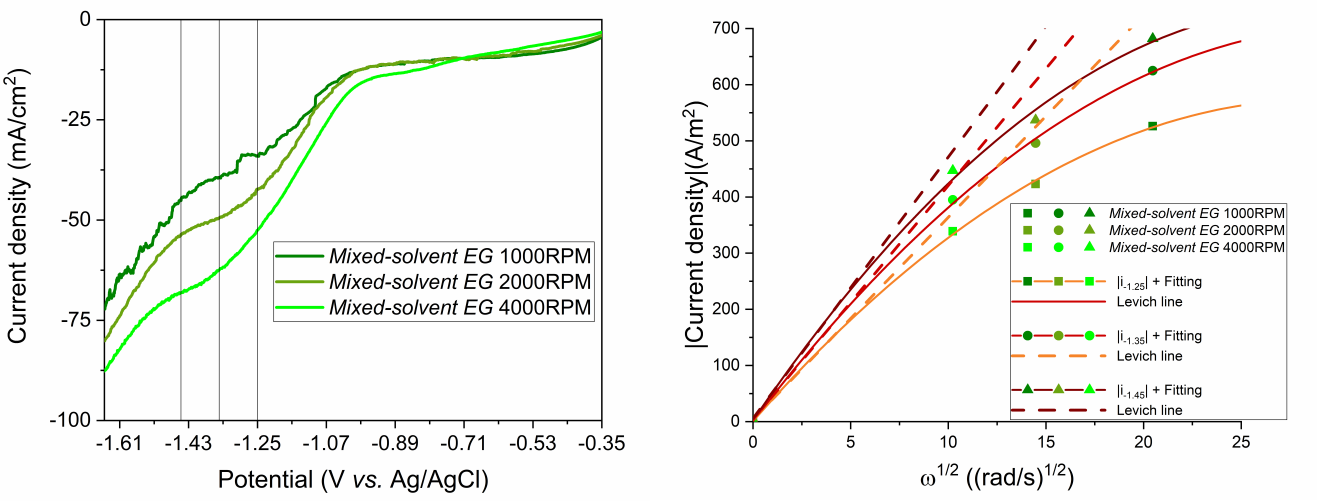

(a) (b)

Figure 5.4 – Measurements using a RDE set-up for the *Mixed-solvent EG* FeCrNi electrolyte: (a) LSV potentioscans at various rotation speeds and (b) Koutecký-Levich fitting taken at fixed potentials (-1.25, -1.35 and -1.45 V *vs.* Ag/AgCl) with different rotation rates (1000, 2000 and 4000 RPM).

tion rate ($\omega^{-0.5}$), as depicted in Figure 5.3b and Figure 5.4b. In both electrolytes, fitting of these points shows a deviation from a straight line intersecting the origin (Levich line). These plots can be linked to Koutecký-Levich theory (equation (1.22)), which means the systems under study are kinetically limited (*i.e.* irreversible). The slope values retrieved from the fitted Levich lines can be correlated to the corresponding limiting currents (equation (1.21)) and therefore, being used to extrapolate approximate diffusion coefficients valid for the overall FeCrNi reduction systems. For the *Standard aqueous* electrolyte, the slope values are 77.9, 82.7 and 98.9 for the currents at -1.25, -1.35 and -1.45 V *vs.* Ag/AgCl, respectively. Instead, for the *Mixed-solvent EG* electrolyte, the slope values are 36.0, 41.6 and 46.5 for the currents at -1.25, -1.35 and -1.45 V *vs.* Ag/AgCl, respectively. In conclusion, the average diffusion coefficients for the two studied systems are $7.1 \cdot 10^{-9}$ and $2.9 \cdot 10^{-9}$ m^2 s^{-1} for *Standard aqueous* electrolyte and *Mixed-solvent 30 vol% EG*, respectively. These results evince that mixed-solvent electrolyte has a lower diffusion coefficient than all-aqueous case (approx. 2.5 times lower), still remaining in the typical range as other alloys cases [147]. However, this difference can lead to a variation in kinetics for the mixed-solvent electrolyte, therefore affecting nucleation and growth, and thus the final material properties for such system.

5.1.4 Chemical composition and efficiency

The composition in wt% and the current efficiencies (C.E.) of the electrodeposited FeCrNi films have been estimated by means of XRF technique. In the case of the *Standard aqueous* solution the coating is Fe57-Cr28-Ni15 wt% (C.E. 6.2%), whereas for the *30 vol% EG* and *50 vol% EG* electrolytes are Fe54-Cr29-Ni17 wt% (C.E. 9.1%) and Fe56-Cr27-Ni17 wt% (C.E. 9.6%), respectively. The elemental contents in at% of Fe-Cr-Ni-O-C-N (XPS, 50 min sputtering time) and H/metals ratio (He ERDA, 20 min sputtering time) measured in-depth were evaluated for the coatings obtained by using two different EG mixed-solvent electrolytes (*i.e. 30 vol% EG* and *50 vol% EG*) and compared with the results for a film deposited using a *Standard aqueous* solution [115] (Table 5.1).

Table 5.1 – Chemical in-depth composition of Fe-Cr-Ni-O-C-N (XPS, 50 min sputtering time) and of H (He-ERDA, 20 min sputtering time) of electrodeposited FeCrNi films produced from *Standard aqueous* (Chapter 3), *30 vol% EG* and *50 vol% EG* mixed-solvent electrolytes.

Electrolyte	Fe (at%)	Cr (at%)	Ni (at%)	O (at%)	C (at%)	N (at%)	H (at%)/metals
Standard aqueous	37.8	15.8	11.7	16.8	16.4	1.5	16.0
30 vol% EG	44.1	15.4	15.8	15.8	7.6	1.3	15.0
50 vol% EG	41.4	16.0	16.5	17.5	7.4	1.1	17.0

Based on these results, it seems that the decrease in water content (due to EG) inside the electrolyte is positively affecting the current efficiency, which increases in both EG cases by approx. 1.5 times with respect to the aqueous counterpart. Regarding the incorporation of impurities (*i.e.* O, C, N and H), the hydrogen content is similar among all produced coatings, regardless of the used electrolyte. The only noticeable difference among aqueous and mixed-solvent electrolytes is the carbon content, which is half the all-aqueous value when using the EG solutions. These outcomes can be explained by looking at the FeCrNi electroreduction mechanisms proposed in our previous study for aqueous electrolyte(Chapter 3). There, strong HER and local pH increase were correlated to carboxyl-based impurities incorporation. For this reason, here for the mixed-solvent EG electrolyte, the lower fraction of water in the solution reduces the influence of HER at the cathode. Therefore, such variation is responsible for decreasing the incorporated carboxyl moieties coming from Cr(III)-glycine hydroxides/hydrides adsorbed molecules, and consequently for reducing the concentration of carbon within the coating. This fact should also have a positive effect on the mechanical properties of the material, *e.g.* by lowering the electrodeposit's brittleness. The ductility of stainless steel alloys is typically linked to the amount of incorporated carbon [113].

5.2 FeCrNi nanostructures using AAO templates

5.2.1 Morphology and chemical composition

Electrodeposition into AAO templates from aqueous solution at different current densities led to either completely empty channels or hardly any deposited material. SEM cross-section images of a sample obtained by electrodepositing at -20 mA cm^{-2} (Figure 5.5) show that this is the only case in which some presence of deposited material was observed, with the rest of the template remaining unfilled. This random distribution of the material inside the template could be due to produced shocks from cross-section procedure causing detachment of the nano-material and its movement along the AAO pores.

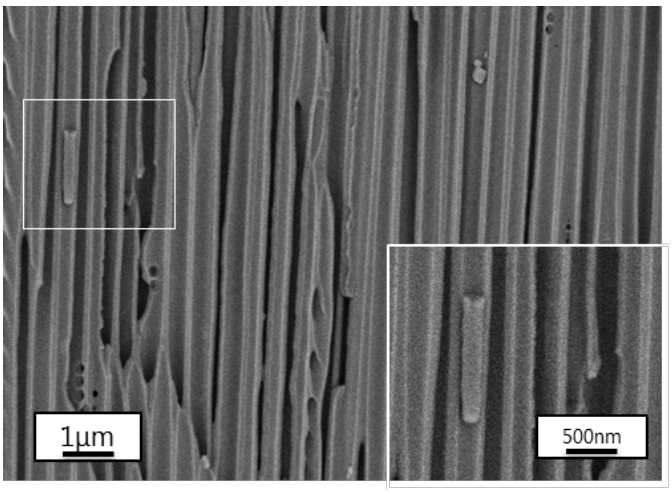

Figure 5.5 – SEM cross-section images of electrodeposited FeCrNi into AAO template from aqueous electrolyte.

In contrast, the electrodeposition of FeCrNi from the mixed-solvent *30 vol% EG* electrolyte shows all samples exhibiting a higher filling ratio than the *Standard aqueous* cases, *i.e.* from less than 10 µm applying a relatively low current density (-5 mA cm^{-2}), up to 30 µm when doubling the current density (-10 mA cm^{-2}). At a high current density the pore filling followed a cylindrical growth with NTs formation, as shown in the SEM cross-section images (Figure 5.6a1-4). At a low current density the material is more compact, resulting in NWs (Figure 5.6b1-3). When dissolving the AAO template for the various studied electrodeposited samples, it was possible to recover only a few NWs from the low current density case (Figure 5.6b4-5).
The atomic compositions of such NWs have been measured by using the EDX technique. The presence of carbon in the spectra is caused by the carbon matrix background, and other impurities (*i.e.* oxygen and nitrogen) are not considered in this discussion due to the measurement uncertainty for these elements. The NWs are mainly formed by Fe, Cr and Ni. Considering each NW individually, the atomic contents of these three elements along a NW are rather homoge-

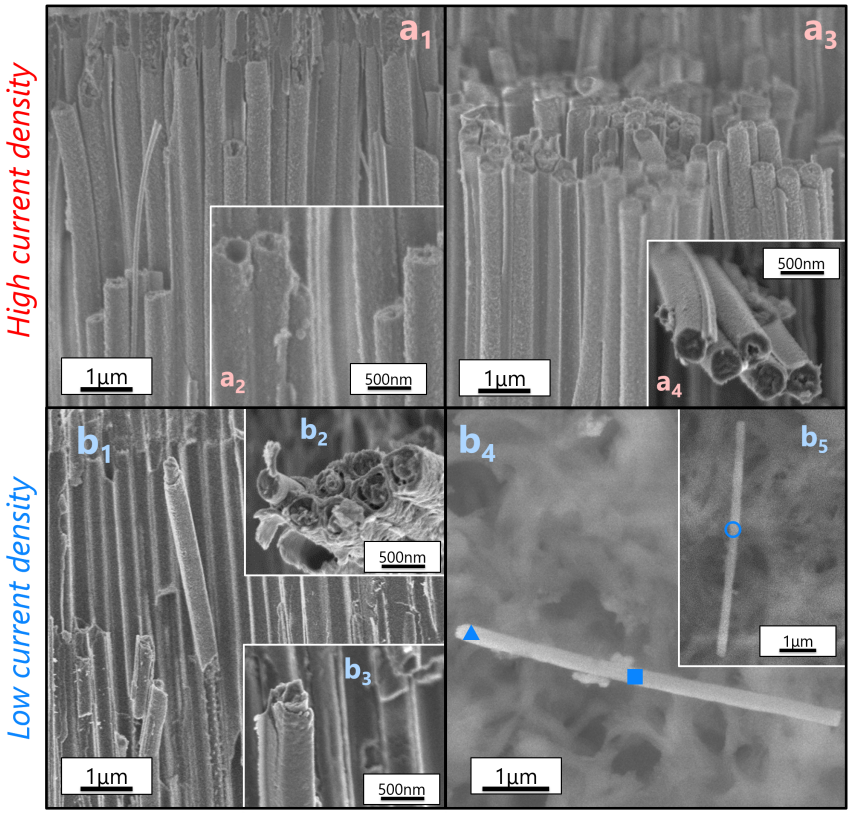

Figure 5.6 – SEM cross-section images of electrodeposited FeCrNi inside AAO templates from mixed-solvent *30 vol% EG*: (a1, a2, a3, a4) at a higher current density (-10 mA cm^{-2}) NTs growth, (b1, b2, b3) at a lower current density (-5 mA cm^{-2}) NWs growth. (b4, b5) SEM top-view images of dissolved single FeCrNi NWs.

Table 5.2 – Elemental composition of Fe-Cr-Ni (EDX) in at% at different points of single electrodeposited FeCrNi NWs using a mixed-solvent EG electrolyte (from Figure 5.6b4-5).

	Fe (at%)	Cr (at%)	Ni (at%)
triangle	64.3	4.9	30.8
square	66.9	3.1	30.0
ring	53.6	26.1	20.3

neous (Table 5.2 triangle and square). However, for different NWs of the same analysed sample, Fe-Cr-Ni contents vary. This could be due to an uneven primary current distribution (PCD) present in different parts of the samples (*i.e.* centre and edges) during electrodeposition.

5.2.2 Kinetic and growth model correlation

The possible mechanisms explaining the behaviour of this ternary FeCrNi electrochemical system are schematically drawn in Figure 5.7. When a relative high cur-

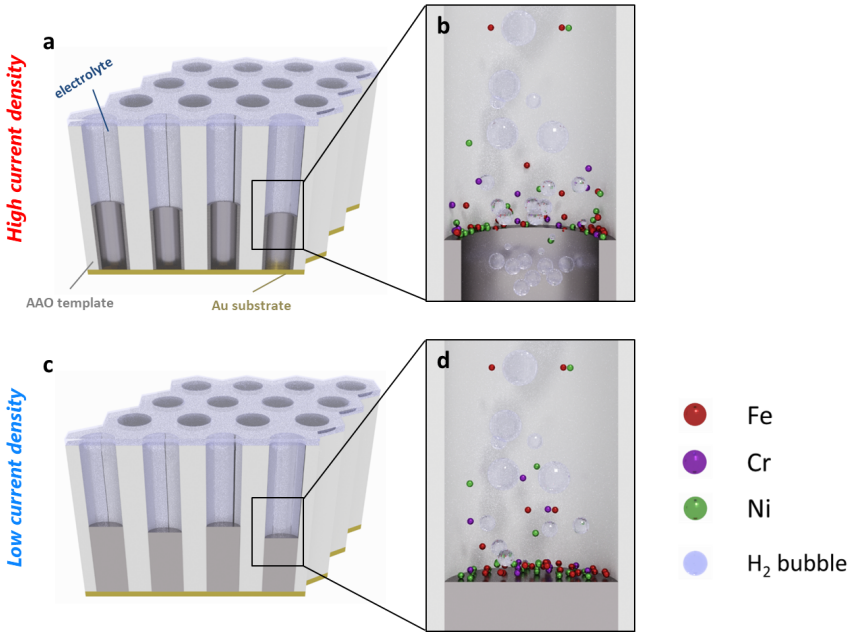

Figure 5.7 – Schematic of the possible growth mechanisms proceeding inside AAO templates during the electrodeposition of FeCrNi: (a, b) NTs produced at a higher current density, (c, d) NWs created at a lower current density.

rent density is applied, the HER forms H_2 bubbles that escape from the pores. The combination of more intense PCD at the edges of the pores and a favourable pathway for H_2 bubbles at the centre of each AAO pore force the material to mainly grow on the side-walls, leading to the formation of NTs, which are longer and less compact. However, when a relatively low current density is used, HER is less pronounced, as well as PCD. Consequently, the growth inside the pores is more homogeneous, producing shorter, but denser NWs. This work's experimental results and the proposed mechanisms can be correlated with the kinetic model explained by Philippe *et al.* [69, 70] for the electrodeposition of Co into high AR nanoelectrodes. In that study, the growth inside nanoporous templates was linked to two main factors. First, metal ions follow a spherical diffusion-controlled regime, when steady state is reached (*i.e.* Nernst diffusion layer becomes larger than the template thickness) and, second, the occurrence of pH variation inside the pores due to the HER. We propose that this model is also valid for more complex electrochemical systems such as the FeCrNi ternary system.

5.3 FeCrNi micro-components using UV-LIGA process

5.3.1 Electrodeposition method

Previously in Section 5.2, a mixed-solvent EG FeCrNi electrolyte has been found to be promising for electroplating into nano-templates, such as anodised aluminium oxide (AAO), decreasing the effect of the HER. However, electrodepositing FeCrNi inside UV-LIGA moulds was technically/experimentally challenging. The cause has been mainly correlated with the delamination of the negative photoresist (*i.e.* SU-8) templates due to two consequential factors. The first is due to H_2 bubbles from the HER, especially at the edges of the mould's cavities at the electrode surface in which primary current distribution is typically enhanced. At the cathode surface, the mould started to detach due to the strong mechanical force produced by the bubbling. The second factor has been the electrodeposition of material where the mould was slightly detaching (under-deposition). This cascade process has been responsible for the complete delamination of the moulds. Although in case of mixed-solvent EG electrolytes this phenomena was less intense than the all-aqueous counterpart, this was not sufficient for obtaining micro-components with such a fabrication technique.

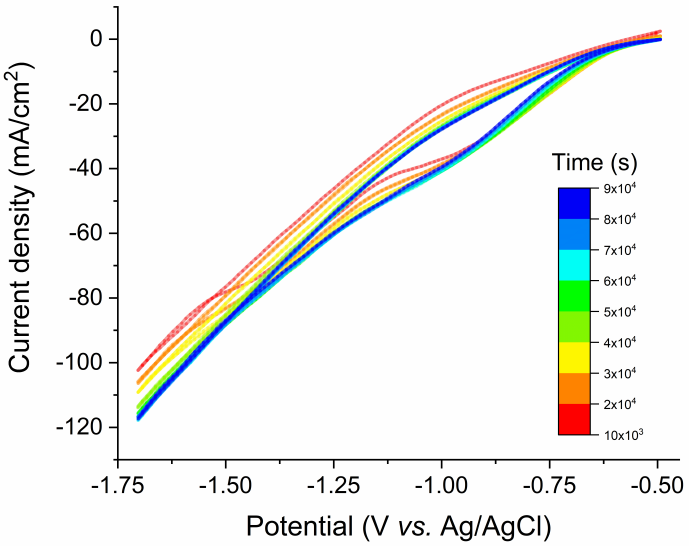

Figure 5.8 – Electrodeposition method (CV-like technique) for achieving FeCrNi micro-components inside LIGA moulds.

A solution to the mould's delamination problem was the implementation of a CV-like electrodeposition together with a FeCrNi mixed-solvent EG electrolyte. Sweeping the potential between -1.7 and -0.5 V *vs.* Ag/AgCl (Figure 5.8) diminished the effects of the HER on the mould by lowering the applied stress produced over time. The sweeping range was chosen in the electrochemical window in which iron, chromium and nickel are reduced, but not oxidised, and this method has been proven to produce coatings with the desired Fe-Cr-Ni com-

position.

5.3.2 Morphology and chemical composition

FeCrNi micro-pillars have been obtained for the first time by electrodepositing inside UV-LIGA moulds. SEM tilted images (Figure 5.9) show the morphology of two of the produced micro-pillars after the removal of the SU-8 photoresist mould.

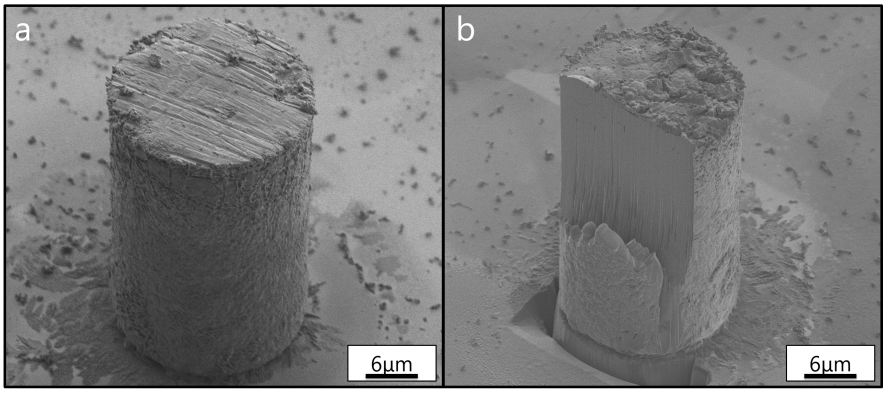

Figure 5.9 – SEM images of electrodeposited FeCrNi micro-pillars obtained using LIGA process: (a) with 45 ° tilting and (b) after FIB cross-section with 30 ° tilting.

Taking into consideration the tilting of 45 ° for the micro-pillar in Figure 5.9a, the extrapolated dimensions are 34.2 µm in height and 23.6 µm in diameter. All analysed micro-pillars appear to be straight-walled and to not have any tapering, which is instead very common for FIB milled micro-pillars, commonly tapered at 2 to 3.5 ° [148]. This is an advantage for micro-pillar compression tests making it feasible to retrieve more reliable mechanical information about the material without applying any correction due to tapering or without having a dedicated FIB stage/set-up [149]. Other enormous benefits of using LIGA process with respect to FIB-milling are, first of all, the avoidance of Ga ion implantation during milling and, secondly, the higher number of micro-pillars (or other structures) which can be created at once with the former technique [150,151]. For a typical 4-inch Au/Si wafer, millions of micro-components, made for example of nickel, can be obtained after a few hours of electrodeposition inside the LIGA mould. From SEM images, it is also possible to notice that the walls of the pillars seem rough and porous. However, after FIB cross-section (Figure 5.9b), the material appears to be uniform and compact, and porosity is not present if not for some sporadic nanometer-size (< 10 nm) voids. The lines visible at the surface are due to FIB curtaining effect: FIB ion bombardment is propagating some of the nano-size porosities along the cut, producing these fictitious lines. This is because the sputtering rate is higher at voids or edges [152]. EDX measurements allowed to obtain the Fe-Cr-Ni composition of the micro-pillars which is Fe 60.2 - Cr 21.5 - Ni 18.3 at%, therefore very close to the one of AISI 304 SS.

5.4 Summary

The electrodeposition of a stainless steel-like FeCrNi ternary alloy was investigated both in aqueous and mixed-solvent EG electrolytes on flat substrates and inside miniaturised moulds, *i.e.* nanoporous anodic alumina templates and UV-LIGA moulds. EG-based baths required lower current densities at the same deposition potentials, when compared to their aqueous counterpart, showing that the parasitic HER consumed less current during electrodeposition. The comparison of metal contents and impurities in-depth of the studied coatings revealed identical compositions, except for carbon at%, which was reduced by half in the case of the mixed-solvent electrolyte. The decrease in both HER and carbon content can be beneficial factors for improving electrodeposition into miniaturised moulds by increasing current efficiency and thus mechanical properties of the material. Electrodepositing into AAO templates from an aqueous FeCrNi electrolyte resulted in almost no filling of the pores. By using a 30 vol% EG mixed-solvent electrolyte it was possible to grow up to 30 µm thick material inside the templates. The main parameter affecting the deposition inside the nanoscale pores was the current density. Depending on current density, NWs or NTs could be grown inside the moulds. EDX measurements of Fe-Cr-Ni contents of the dispersed NWs showed that the composition was homogeneous along the NW length, but dissimilar when analysing different NWs for the same sample. For the first time, it was revealed that FeCrNi nanostructures can be achieved *via* electroplating into AAO templates from a Cr(III)-based mixed-solvent electrolyte. Moreover, the shape of such nanostructures can be controlled by varying the current density, giving rise to either NTs or NWs using higher or lower currents, respectively. Such a phenomenon can be explained by the kinetic and growth models present in the literature for single metals electrodeposited into nano-moulds. Additionally, FeCrNi micro-components were obtained by combining a mixed-solvent electrolyte together with a CV-like deposition method, in order to avoid the delamination of LIGA photoresist moulds during plating. FeCrNi micro-pillars were fabricated, showing good morphology without porosity issues and chemical composition matching the one of metallurgical austenitic SS.

6 FeCrNi mixed-solvent *vs.* aqueous electrolytes: materials properties

In Chapter 5, we investigated the deposition process from a novel mixed-solvent electrolyte for the electrodeposition of FeCrNi which allowed to successfully achieve micro and nanocomponents by decreasing the influence of HER during the deposition process. Although the morphology of the electrodeposited materials was independent of the used electrolyte (aqueous or mixed-solvent), we observed that the compositions were slightly different and most probably also the porosity due to lower HER (Chapter 4). Moreover, until now, materials properties have been investigated only for FeCrNi electrodeposited from an all-aqueous solution and for as-deposited amorphous samples in which the chromium content was varying.
In the following chapter, the FeCrNi electrodeposits is characterised thoroughly in terms of the most relevant properties important in view of the final bio-medical and micro-robotics application-oriented scope (*i.e.* corrosion resistance, biocompatibility, magnetic response and mechanical properties). This investigation consists of a comparison of such properties for the two types of coatings produced by varying the electrolyte solvent (*i.e.* all-aqueous and mixed-solvent EG). Not only the variations in composition, but also the changes in microstructure, from amorphous in as-deposited films to nano-crystalline in annealed coatings, are considered.

Declaration of contribution
In this work, Enrico Bertero produced the coatings, characterised the samples using XRF, XRD and XPS, and contributed to most of data analysis and writing. Petai Pip (Empa - Thun) performed the magnetic measurements. Nadia Rohbeck (Empa - Thun) performed nanoindentation tests for obtaining the mechanical properties of the samples. Max Döbeli (ETH - Zurich) performed He ERDA measurements for retrieving the hydrogen content. Inge K. Hermann (Empa - St. Gallen) tested the cytotoxicity of the coatings. Johann Michler and Laetitia Philippe (Empa - Thun) supervised the work and provided the facilities to carry the work out.

Parts of this chapter use materials adapted from Bertero *et al.* [116,142] (Elsevier Copyright) and from Bertero *et al.* [115] with permission from the Royal Society of Chemistry.

6.1 Coating's from aqueous and mixed-solvent electrolytes

6.1.1 Crystal structure

Bragg-Brentano XRD measurements were performed on FeCrNi electrodeposits both as-deposited and annealed under an Ar controlled atmosphere, produced using a *Mixed-solvent EG* electrolyte (Figure 6.1). Diffraction peaks at $2\theta \approx 38$, 69 and 82 ° correspond to face-centered cubic fcc Au (111), Si (100) and fcc Au (222) crystal planes (substrate contributions), respectively.

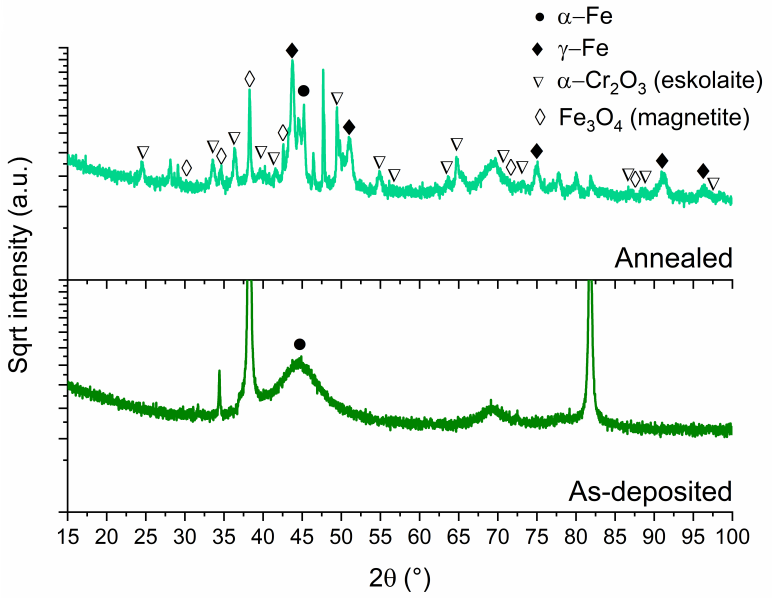

Figure 6.1 – BB-XRD measurements of FeCrNi as-deposited and annealed electrodeposits obtained from a *Mixed-solvent EG* electrolyte.

These results are very similar to the ones obtained for coatings from *Standard aqueous* electrolyte (using a platinum anode) in Section3.1.2. As-deposited films are amorphous, presenting a broad 2θ peak at approx. 45 °, showing the material has a tendency to (110) reflection of the bcc α–Fe structure. Annealed coatings are characterised by several peaks at approx. 44, 51, 75, 91 and 95 ° corresponding to the (111), (200), (220), (113) and (222) crystal planes, respectively, which are reflections of the γ-Fe fcc phase. Although the major crystalline structure is γ-Fe, a distinct α-Fe peak is also visible at 45 °, showing that the film is a mixture of γ-Fe and α-Fe phases. The mean crystallite size calculated from the most intense γ-Fe peak is in the 20-25 nm range. The small peaks discernible from the diffractogram correspond to iron oxides (Fe_3O_4 - magnetite) and chromium oxide (α-Cr_2O_3 - eskolaite). All diffractograms present a high background at low angles, which could be attributed to the presence of amorphous oxides.

6.1.2 Chemical composition

The composition in wt% and the current efficiencies (C.E.) of the electrodeposited FeCrNi films has been estimated by means of XRF technique. For the *Standard aqueous* solution the coating is Fe57-Cr28-Ni15 wt% (C.E. 6.2%), whereas for the *Mixed-solvent EG* electrolyte is Fe54- Cr29-Ni17 wt% (C.E. 9.1%). For each electrolyte, two samples with varying chromium content have been annealed in Ar controlled atmosphere. *Standard aqueous* electrolyte annealed coatings are Fe59-Cr25-Ni18 wt% (named low Cr 25wt%) and Fe52-Cr35-Ni13 wt% (named high Cr 35wt%). Instead, *Mixed-solvent EG* electrolyte annealed films are Fe57-Cr25-Ni15 wt% (named low Cr 25wt%) and Fe51-Cr35-Ni14 wt% (named high Cr 35wt%). Moreover, the elemental contents measured in-depth in at% of Fe-Cr-Ni-O-C-N (XPS, after 5 and 50 min sputtering time) and H/metals ratio (He ERDA, after 20 min sputtering time) were also evaluated [115, 142] (Table 6.1).

Table 6.1 – Elemental composition in-depth of Fe-Cr-Ni-O-C-N (XPS, after 5 and 50 min sputtering time) and of H (He-ERDA, after 20 min sputtering time) of electrodeposited FeCrNi films produced from aqueous solution and mixed-solvent EG electrolytes: as-deposited and annealed.

Sample	Sput. time (min)	Fe (at%)	Cr (at%)	Ni (at%)	O (at%)	C (at%)	N (at%)	H (at%)/metals
Standard aqueous	5	38.3	15.4	11.1	17.0	16.7	1.5	-
as-dep. (Cr 28wt%)	50	37.8	15.8	11.7	16.8	16.4	1.5	16.0
Standard aqueous	5	9.2	33.7	0.3	55.2	1.0	0.6	-
ann. (low Cr 25wt%)	50	36.0	23.3	10.3	22.0	6.5	1.9	3.7
Standard aqueous	5	13.1	31.8	7.9	44.6	0.9	1.7	-
ann. (high Cr 35wt%)	50	30.0	27.6	7.7	22.6	9.6	2.6	-
Mixed-solvent EG	5	42.8	15.7	16.2	16.1	7.8	1.4	-
as-dep. (Cr 29 wt%)	50	44.1	15.4	15.8	15.8	7.6	1.3	15.0
Mixed-solvent EG	5	6.6	38.4	3.5	44.6	6.1	0.8	-
ann. (low Cr 25wt%)	50	32.1	25.0	12.5	22.2	6.7	1.4	-
Mixed-solvent EG	5	0.7	41.3	0.2	52.2	4.9	0.7	-
ann. (high Cr 35wt%)	50	28.4	30.7	8.2	24.7	6.9	1.2	-

For the as-deposited samples (*i.e.* both electrolyte cases), the composition after few minutes of sputtering can be considered already as the bulk one, remaining constant throughout the thickness of the coating, which means that the oxide layer is rather thin (below 50 nm). The main difference in these coatings is the carbon content, which is half in case of the sample obtained from a mixed-solvent electrolyte with respect to all-aqueous film. This decrease can be related to the lower amount of water in solution, which reduces the influence of HER at the cathode, therefore, diminishing the incorporation of carboxyl compounds

within the coating from the Cr(III)-glycine electroreduction process (Chapter 3).

The results from annealed samples indicate a rather complex material, especially when considering the oxide layer. For each type of electrolyte, two samples with different average chromium concentrations (low Cr 25wt% and high Cr 35 wt%) were annealed and analysed by XPS. For all annealed cases the high amounts of oxygen and chromium after 5 min sputtering denote a thicker oxide layer (at least 50 nm) with respect to the as-deposited counterparts. Here, it is interesting to notice that these samples are not following a clear trend in terms of oxide layer composition (no dependence on the average bulk chromium concentration). From the XPS fitting of annealed samples analysed after 5 min sputtering (Figure 6.2 and 6.3), the major difference among the coatings is that, in some cases, nickel is not present at all in the oxide layer (*Standard aqueous* low Cr 25wt% and *Mixed-solvent EG* high Cr 35wt%). For the rest of the elements, chromium is in a mixture of metallic, oxide and carbide-like phases, whereas iron is present both as metal and oxide. In-depth of the annealed coatings (after 50 min sputtering), the behaviour is comparable to the thermally treated films (*Pt anode* case) in Chapter 3. Chromium, iron and nickel amounts and XPS fitting are similar to those described previously for 5 min sputtering measurements, but here the metallic contributions are much higher with respect to the total oxidised state ($2^+/3^+$) ones (except for nickel which is always present in the metallic state).

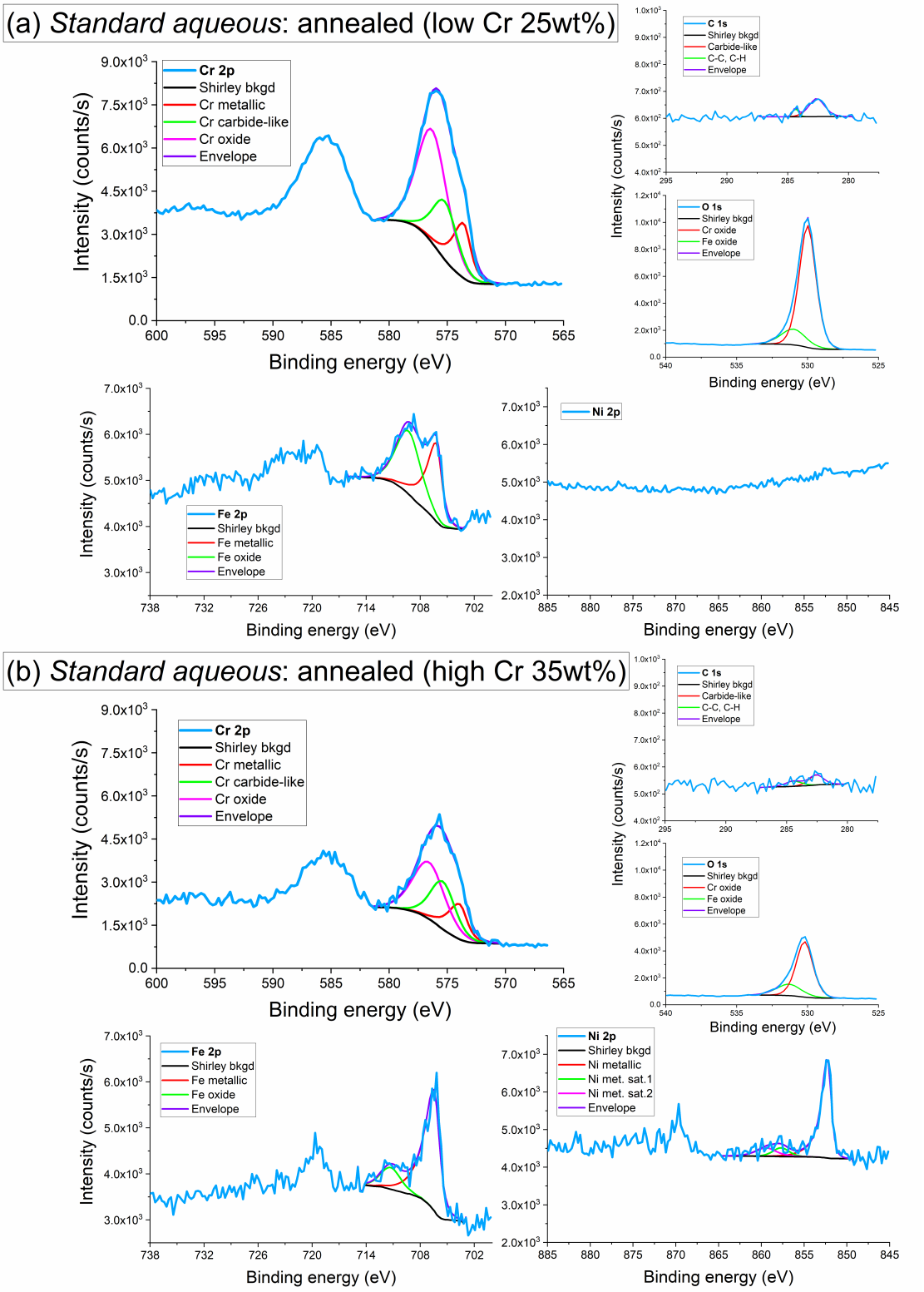

Figure 6.2 – Cr 2p, C 1s, O 1s, Fe 2p and Ni 2p XPS fitted spectra of electrodeposited FeCrNi annealed films from a *Standard aqueous* electrolyte analysed after approx. 5 min sputtering: (a) low Cr 25wt% and (b) high Cr 35wt% coatings.

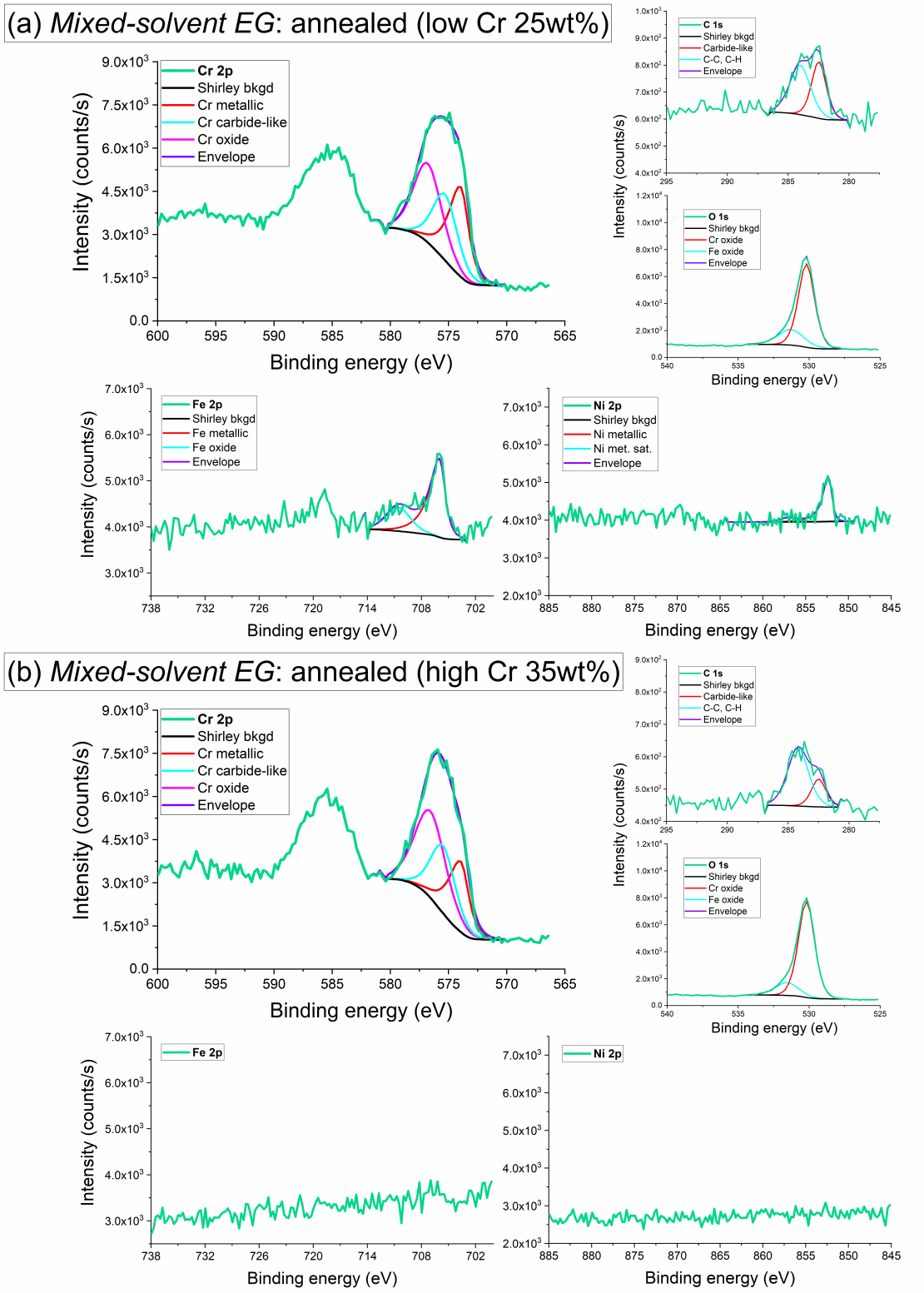

Figure 6.3 – Cr 2p, C 1s, O 1s, Fe 2p and Ni 2p XPS fitted spectra of electrodeposited FeCrNi annealed films from a *Mixed-solvent EG* electrolyte analysed after approx. 5 min sputtering: (a) low Cr 25wt% and (b) high Cr 35wt% coatings.

6.1.3 Corrosion resistance

Corrosion resistance in stainless steel (18Cr-11Ni) is dependent on the surface passive oxide layer and there are many parameters affecting passivation of such materials, *e.g.* composition [123], thickness [124] and microstructure [31]. We wanted to investigate the corrosion resistance of FeCrNi electrodeposits obtained using a mixed-solvent EG electrolyte and compare these results to all-aqueous samples and to annealed coatings in which thickness and microstructure are very different. Anodic linear sweep voltammograms were measured in 0.5 M aqueous sulphuric acid for FeCrNi electrodeposits from a *Mixed-solvent EG* (as-deposited) and a *Standard aqueous* (as-deposited and annealed) electrolytes, as depicted in Figure 6.4. We employed a cathodic pre-treatment (at -0.6 V *vs.* Ag/AgCl for 15 min) in order to remove the native oxide layer, enabling the characterisation of oxide formation and its anodic dissolution during a potential sweep. The polarisation measurements were performed immediately after the pre-treatment.

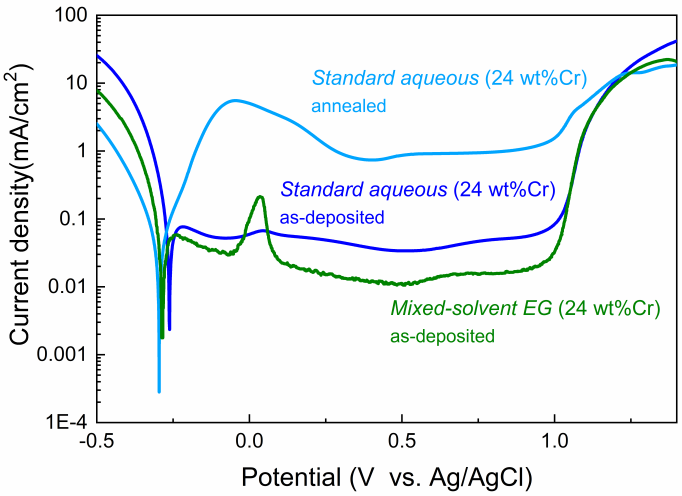

Figure 6.4 – Anodic polarisation curves (with cathodic pre-treatment) in 0.5 M H_2SO_4 aqueous solution for similar FeCrNi (Cr 24 wt%) electrodeposits obtained from different electrolytes: *Standard aqueous* (as-deposited and annealed) and *Mixed-solvent EG* (as-deposited).

In Chapter 4, we performed polarisation scans in acidic media for FeCrNi electrodeposited coatings obtained from a Cr(III)-glycine aqueous electrolyte (with various chromium content), and compared them with the one for austenitic SS (AISI 304 and 316L). Those results showed that FeCrNi electrodeposits with chromium content higher than 24 wt% had good passivation properties similar to standard metallurgical SS. Similarly here, all polarisation scans exhibit the typical transient regions (active, passive and transpassive) and the corrosion parameters, extracted using Tafel plots, are listed in Table 6.2. The retrieved high corro-

Table 6.2 – Extracted corrosion parameters from anodic LSV tests in aqueous sulfuric acid (0.5 M H_2SO_4) for as-deposited and annealed FeCrNi electrodeposits obtained from aqueous and mixed-solvent electrolytes, and for AISI SS (Chapter 4).

Sample	Electrolyte	E_{corr} (V *vs.* Ag/AgCl)	i_{corr} (mA/cm^2)
As-deposited (Cr 24 wt%)	*Standard aqueous*	-0.262	0.197
As-deposited (Cr 24 wt%)	*Mixed-solvent EG*	-0.286	0.212
Annealed (Cr 24 wt%)	*Standard aqueous*	-0.296	0.053
AISI 304	-	-0.366	0.237
AISI 316L	-	-0.304	0.102

sion currents for all analysed cases are due to the harsh test environment used here (0.5 M sulphuric acid) and consistent with the ones obtained for AISI SS and for similar alloys found in literature [124]. In the case of as-deposited samples, both samples have excellent passivation (comparable to AISI 304 and 316L SS), with the *Mixed-solvent EG* one having an even lower passive current. However, after the first oxide formation peak, it is clear that a second additional maximum (starting at around -0.1 V *vs.* Ag/AgCl) is present mainly in the *Mixed-solvent EG* case. This second peak has been observed in many different stainless steels. Although the cause of this peak is still not well understood, some explanations have been proposed so far [125]:

1. surface nickel enrichment during pre-polarisation exposure
2. oxidation of absorbed hydrogen from cathodic pre-treatment
3. preferential attack along phase or grain boundaries of ferrite and martensite

Looking also at both microstructure and XPS composition values (Table 6.2), it seems the only differences among the electrodeposited coatings are the decrease in carbon and the increase in nickel content. The latter could be the cause for the decrease of the passive current because of a higher chromium to iron ratio. An increase in nickel is known to lower the stability of the passive layer in sulphuric acid solutions [153], which could explain why the second anodic peak is enhanced for the *Mixed-solvent EG* as-deposited case. Also, we observed in Chapter 5 a lowering in the HER when FeCrNi coatings were produced using a EG-based electrolyte. This may lead to a decrease in hydroxides/hydrides present within the passive oxide layer, changing the passivation of the film. Regarding the annealed case, the anodic oxide formation peak is much higher and wider with respect to the as-deposited counterparts, probably incorporating the dissolution peak corresponding to Fe(II) species. Even though

thermal post-treatment produces coatings with a thicker oxide layer, passivation of such films is poorer, as the passive current is at least one order of magnitude higher than the as-deposited cases. This could be due to the nanocrystalline microstructure of the annealed coating and because of the segregation of chromium oxide at the grain boundaries (as described previously in Chapter 3). It is known that grain boundaries are preferential sites for oxidation/dissolution because of many concurrent factors which are typically favoured in these locations [29]. Segregation of some compounds (such as carbides) with consequently depletion of chromium can lead to intergranular corrosion. Also, in steels, defected oxides and non-homogeneities are typically linked to poor corrosion resistance (localised corrosion). In case of amorphous coatings, in certain corrosive environments, both the homogeneity in composition and the absence of grain boundaries are important factors explaining the better corrosion resistance [30]. Amorphous steel 304 was found to have improved corrosion resistance to pitting than the crystalline counterpart [32, 33].

6.1.4 Bio-compatibility

Bio-compatibility of cells on the surface of FeCrNi electrodeposits from Mixed-solvent EG electrolyte (as-deposited and annealed) was evaluated by quantifying LDH release into the medium (Figure 6.5). The release of LDH is correlated with membrane damages and therefore, to cytotoxicity of the investigated material. All as-deposited coatings present similar results, even though the content of chromium varies from 27 to 32 wt%. The values are rather low and comparable to austenitic stainless steel 304. Whereas, annealed electrodeposited films show a lowering in LDH release, which values are similar or even lower than the one from AISI 316L. This behaviour is most probably correlated with the increase in the chromium oxide layer thickness by annealing process. Instead, by comparing the results of the as-deposited coatings from *Mixed-solvent EG* electrolyte showed here with the ones from *Standard aqueous* solution (Chapter 3), it seems that the lower amount of carbon content within the films is not a critical factor for achieving good bio-compatibility.

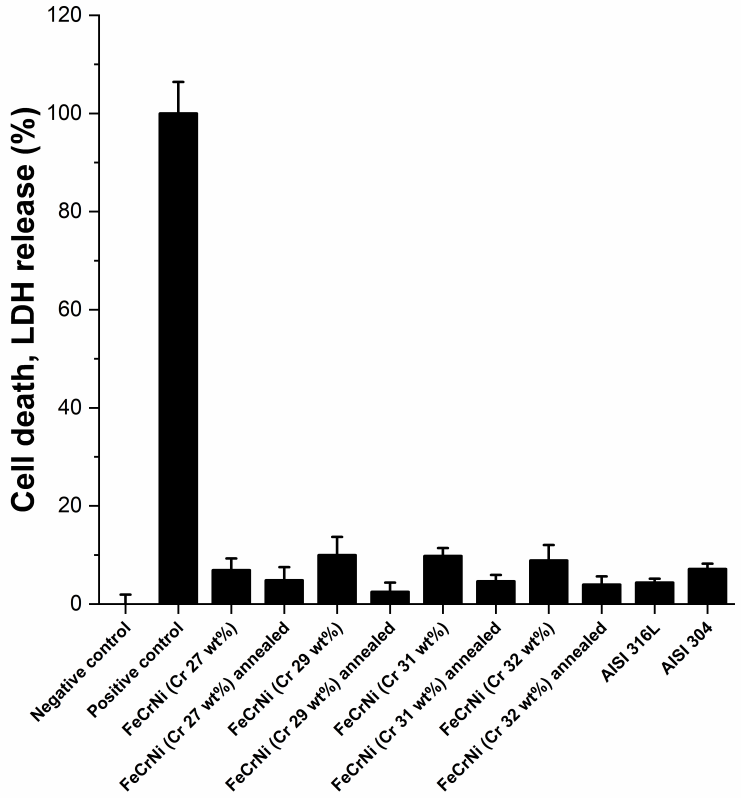

Figure 6.5 – Cytotoxicity tests with LDH assay for electrodeposited FeCrNi films (as-deposited and annealed) obtained using a *Mixed-solvent EG* electrolyte, AISI 304 and AISI 316L.

6.1.5 Magnetic behaviour

Magnetic measurements (*via* SQUID VSM) were performed on both as-deposited and annealed FeCrNi electrodeposited films produced using a *Mixed-solvent EG* electrolyte. The major objective was to investigate the magnetic behaviour of the coatings in function of both coatings' composition, characterised by a lower carbon incorporation with respect to the all-aqueous counterpart, and microstructure variation from amorphous/ultra-fine grained (as-deposited samples) to nanocrystalline (annealed samples). Figure 6.6 depicts the measured hysteresis loops for the various electrodeposited FeCrNi coatings.

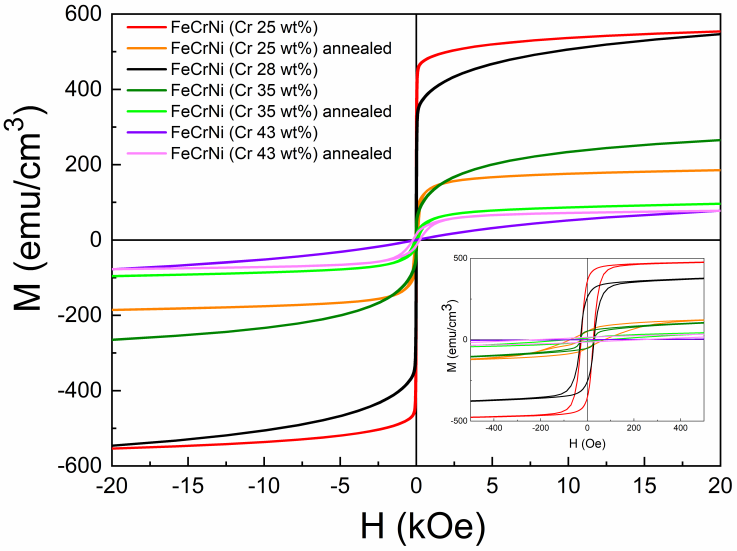

Figure 6.6 – Hysteresis loops measured at room temperature for: electrodeposited FeCrNi coatings obtained from a *Mixed-solvent EG* electrolyte with different chromium contents (as-deposited and annealed), metallurgical AISI 304 and 316L SS.

In Chapter 3, we showed that electrodeposited FeCrNi coatings from a *Standard aqueous* electrolyte were ferromagnetic as opposed to metallurgical austenitic stainless steel which is non-magnetic. Also here, the materials exhibit soft ferromagnetic behaviour, having small coercivities and quite large saturation magnetisation values. Therefore, changing the electrolyte used (all-aqueous or mixed-solvent EG), which leads to a variation in incorporated impurities (carbon and hydrogen -based) and probably in morphology, is not a critical parameter for achieving magnetic properties in FeCrNi electrodeposits. For the as-deposited samples, the saturation magnetisation (M_S) decreases drastically when increasing the chromium content from 25 to 43 wt% (Figure 6.7a). This behaviour (also mentioned in Chapter 3) is in agreement with studies on FeCr-based metallic glasses in which there is a competition between Fe-Fe ferromagnetic exchange interactions and Fe-Cr anti-ferromagnetic ones.

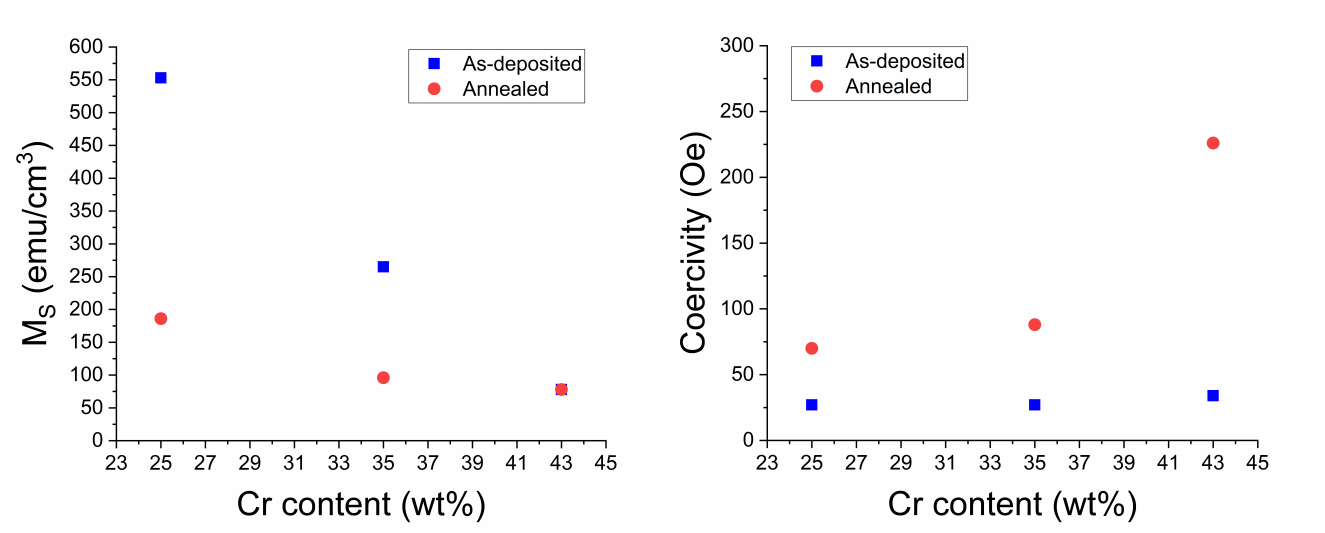

(a) (b)

Figure 6.7 – Extrapolated magnetic properties of electrodeposited FeCrNi coatings (as-deposited and annealed) obtained using a *Mixed-solvent EG* electrolyte, as a function of chromium content: (a) saturation magnetisation and (b) coercivity.

Looking at the as-deposited/annealed pairs, we observe a decrease in saturation magnetisation in almost all annealed cases (Figure 6.7a). Such behaviour can be associated with the complexity of the material, dictated by variation in microstructure and composition (*i.e.* metals, oxides and impurities). Especially when annealed, FeCrNi electrodeposits present different crystalline structures in which α-Fe (bcc) and γ-Fe (fcc) metallic phases coexist together with iron and chromium oxides and carbon-based impurities. Upon annealing, the increase in oxides (which are typically anti-ferromagnetic compounds [154]) and the transition in microstructure (from amorphous meta-stable α-Fe to nano-crystalline γ-Fe [155]) could be some of the reasons for the diminishing of saturation magnetisation. Moreover, the difference in as-deposited/annealed M_S is becoming less marked with the increase in chromium content, probably because of the anti-ferromagnetic contribution of metallic chromium becoming dominant with respect to the oxide one. Instead, the extrapolated coercivity values (Figure 6.7b) show a clear trend: annealing coatings with higher amounts of chromium results in materials with enhanced coercivities. Such behaviour could also be related to the above-mentioned hypothesis. Both the variation in microstructure and metals/oxides composition are influencing the material's ability to withstand an external magnetic field (*i.e.* retaining its magnetisation).

6.1.6 Mechanical properties

The mechanical properties of the analysed materials were investigated by nanoindentation tests, comparing FeCrNi electrodeposits (as-deposited and annealed) obtained from different electrolytes, *i.e. Standard aqueous* and *Mixed-solvent EG*, and with different chromium contents. Table 6.3 shows the results of these tests.

Table 6.3 – Mechanical properties from nanoindentation tests: elastic modulus (E), hardness (H) and maximum penetration depth of the tip as measured on the surface for the electrodeposited FeCrNi films produced from aqueous solution and mixed-solvent electrolytes, both as-deposited and annealed.

	E (GPa)	H (GPa)	Maximum tip penetration depth (nm)
Standard aqueous as-deposited (Cr 28wt%)	171 ± 5	8.3 ± 0.4	206 ± 4
Standard aqueous annealed (low Cr 25wt%)	93 ± 9	5.1 ± 0.5	273 ± 12
Standard aqueous annealed (high Cr 35wt%)	238 ± 5	12.2 ± 0.5	171 ± 3
Mixed-solvent EG as-deposited (Cr 29wt%)	114 ± 9	4.1 ± 0.5	286 ± 17
Mixed-solvent EG annealed (low Cr 25wt%)	229 ± 5	9.8 ± 0.2	185 ± 2
Mixed-solvent EG annealed (high Cr 35wt%)	96 ± 2	6.7 ± 0.2	244 ± 3
AISI 316L	198 ± 7	3.7 ± 0.4	-
Fe-15Cr-15Ni (at%) singlecrystal (fcc) [156]	156 ± 11	1.46 ± 0.02	-

For coatings in the as-deposited state (amorphous/ultra-fine grained), it was observed that the *Standard aqueous* solution produced a coating exhibiting higher hardness and elastic modulus values compared to the one obtained from the mixed-solvent electrolyte. The maximum penetration depths of the indenter tip did not exceed 300 nm in these measurements, thus probing primarily the mechanical behaviour of the bulk material. Earlier tests (XPS measurements) had revealed that the oxide layer thickness is below 50 nm. XPS chemical composition (Section 6.1.2) shows that the *Standard aqueous* as-deposited coating in-depth contains roughly twice as much carbon as the *Mixed-solvent EG* one. In both coatings the carbon is bonded to chromium in a carbide-like fashion, hence leading to an overall high hardness [113] and explaining the improved

hardness of the former coating (all-aqueous electrolyte) when compared with the latter (mixed-solvent electrolyte). These results are comparable with the one measured for metallurgical AISI 316L and with a single crystal (fcc) Fe-15Cr-15Ni alloy [156].

In addition, two FeCrNi electrodeposits (for each electrolyte type) with different chromium composition (low Cr 25wt% and high Cr 35wt% contents) have been annealed and tested both on the surface and in-depth (after 50 min sputtering time). Surface and in-depth tests (here only the surface results are listed in Table 6.3) did not show any difference. Moreover, from the results in Table 6.3, it can be observed that there is no systematic trend of hardness or elastic modulus with the average chromium content for annealed coatings. This is also valid when comparing annealed and as-deposited samples within the same electrolyte type.

From a previous study in our group [112], microstructure and mechanical properties in FeCrNi electrodeposits seemed to be linked to the inverse Hall-Petch relationship [28]. In this theory, hardness is increasing by decreasing the grain size (classical Hall-Petch region), then reaching a maximum limit around 10 to 100 nm (stationary cross-over regime), followed by a constant decrease when moving towards amorphous materials (inverse Hall-Petch). However, the inverse Hall-Petch relationship cannot solely explain the differences in hardness observed here.

Comparing the results among the various annealed FeCrNi electrodeposits, hardness and elastic modulus are much higher for the following cases: *Standard aqueous* with high chromium content (Cr 35wt%) and *Mixed-solvent EG* with low chromium content (Cr 25wt%). Looking at XPS measurements (composition and fitting), the only difference among such samples is that coatings with high hardness contain nickel both at the surface (within the oxide layer) and in-depth (within the bulk). A possible explanation is that when larger amount of nickel are present, it is more likely to have a predominant austenitic phase making the material harder. In fact, nickel and chromium are known to be stabilising elements for the microstructure of austenitic stainless steel, the former for γ-ferrite (austenite) phase and the latter for α-ferrite one [157, 158]. The material's hardness and other mechanical properties are generally affected by a combination of various factors, such as microstructure, chemical composition (metals and oxides) and distribution of elements/compounds.

As observed in APT results in Chapter 3, upon thermal treatment, the FeCrNi thin-film transformed into a much more complex material. Not only was there a change in microstructure passing from amorphous (as-deposited) to nanocrystalline (annealed), but further the composition and distribution of the present elements were affected. First of all, weakly bonded compounds (*i.e.* carbon and hydrogen based) degassed the material. Then, an increase in the oxide contribution with respect to the metallic ones (mainly for chromium and iron)

was observed because of the high amount of free oxygen which was present within the as-deposited coatings. Moreover, chromium and chromium oxide together with carboxyl moieties were segregating along the grain boundaries, while nickel was mostly distributed within the grains and iron was present everywhere. Some hypothesis for the variation in hardness upon annealing for the FeCrNi electrodeposits can be explained taking into account also the above-mentioned results. Depletion of chromium within the grain with concurrent augmenting of chromium oxide segregated at the grain boundaries may be a cause of lower hardness. Concurrently, the presence of nickel in higher amounts within the grain may be beneficial for hardening the material by retaining the austenitic phase (higher nickel to chromium ratio). Moreover, elastic properties are known to be very sensitive even to small changes in porosity, which are likely to happen also in such FeCrNi electrodeposits.

In conclusion, we could show that with both electrolytes it was possible to electrodeposit FeCrNi coatings exhibiting good mechanical performances and having properties comparable to standard metallurgical steels. The mechanisms explaining why some of these electrodeposits have higher hardness and elastic modulus than others are not fully understood yet and need further investigation. Nevertheless, such results are all in all promising for applying such electrodeposited material for future applications in the bio-medical sector.

6.2 Summary

Electrodeposited FeCrNi coatings obtained from two different electrolytes, *i.e.* aqueous and mixed-solvent EG, together with austenitic SS, were characterised and compared in terms of many material properties. In this comparison, a comprehensive set of analysis was used in order to investigate the correlation between composition, microstructure and material properties. The results are the following:

- The microstructure of the FeCrNi electrodeposits is independent of the used electrolyte. As-deposited coatings are amorphous/ultrafine-grained (tendency to α-Fe phase), whereas annealed ones are nanocrystalline with a predominant γ-Fe phase (austenite) and a secondary less intense α-Fe phase.

- Chemical composition and oxidation states confirm that the main difference in as-deposited FeCrNi coatings is the lowering of carbon inclusion when a mixed-solvent electrolyte is used. Moreover, independently of the electrolyte used, annealed films show dissimilarities within the oxide thick layer even though the bulk composition is similar. In some coatings nickel is also present in the oxide layer.

- Anodic LSV of the electrodeposits depicts that the as-deposited *Mixed-solvent EG* coating present similar corrosion resistance compared to the all-aqueous counterpart (comparable to austenitic SS), except for the presence of a rather high second anodic peak at approx. -0.1 V *vs.* Ag/AgCl. Many factors can be associated to this phenomena, but most probably the higher presence of nickel in the *Mixed-solvent EG* case is lowering the stability of the passive layer. Instead, passivation of the annealed coating is poorer, which can be correlated to the complex microstructure/composition of such material. In fact, chromium oxide tends to segregate at the grain boundaries, leaving the grains to be a favourable site for dissolution.

- Bio-compatibility results, evaluated by cytotoxicity tests, show that *Mixed-solvent EG* as-deposited coatings have similar LDH release (quantification of cell death) to austenitic SS. Comparing as-deposited and annealed cases, the latter have always a lower cell death in %, which can be associated to the thickening of the oxide layer during thermal treatment.

- Hysteresis loops demonstrate that also in case of a *Mixed-solvent EG* electrolyte, the produced coatings are soft magnetic. In the as-deposited cases, the saturation magnetisation decreases with the increase of chromium content. Whereas, comparing as-deposited and annealed electrodeposits, thermal treatment causes a decrease in M_S for low chromium films and an increase in coercivity for high chromium coatings. This behaviour may be

related to two competing contribution arising from the annealing process: variation in microstructure and metal/oxide composition.

- Nanoindentation tests of all FeCrNi electrodeposits revealed that the as-deposited coating produced using a *Standard aqueous* electrolyte has higher hardness and elastic modulus with respect to the *Mixed-solvent EG* case, which can be associated with the decrease in carbon-based impurities and therefore, the decrease in carbide-like compounds within the coating. Instead, the results for annealed coatings with different bulk concentration do not show any correlation in terms of electrolyte type or films chromium content. Very high hardness and elastic modulus is found in thermal treated coatings in which the nickel content is distributed both close to the surface and in-depth. The mechanisms behind such behaviour are not clear, however an hypothesis can be that coatings with a larger contribution from austenitic phase with respect to ferrite one (due to more austenitic favourable elements such as nickel, carbon and nitrogen) have higher hardness and resistance to deformation.

Conclusions and future work

Conclusions

In this research, the core objectives were to study the electrodeposition of Fe-CrNi from a 'green' Cr(III)-based electrolyte, obtaining a material similar in properties to metallurgical austenitic SS, in order to achieve coatings and micro- and nanocomponents for bio-medical -oriented applications.

This was achieved as in the following:

1. **electrodeposition mechanisms *vs.* material properties**

    - The electrodeposition process of this ternary system (from aqueous solution) was investigated comprehensively by employing different characterisation techniques, comparing results both at macro and micro-nano scale levels. The evolution of microstructure (from amorphous to nanocrystalline) in correlation to film composition and elemental 3D spatial distribution was achieved for coatings produced with the help of different anode materials and thermal post-treatment. The influence of Cr(III) and glycine in terms of coating atomic contents was evaluated for films in which both the applied current density and electrolyte composition were varied. These results, together with a thorough analysis on metals speciation/complexation allowed us to propose various Cr(III)-based electroreduction mechanisms. Glycine was oxidising at the anode producing carbon-based moieties. Instead, Cr(III)-glycine electrochemistry at the cathode led to weakly bonded carboxyl molecules and Cr-hydroxides/hydrides present within the coatings, which were the main factors responsible for the amorphisation process. In addition, from those outcomes it was possible to observe segregation and distribution of impurities, oxides and metals with respect to microstructure variation. Upon annealing, CrOx was preferentially segregated at the grain boundaries and was associated to carbon-based precipitates, whereas within the grains metallic Fe-Cr-Ni were mostly present.
      The as-deposited material was found to be a composite, mainly formed by a matrix of metallic Fe-Cr-Ni, then by chromium organometallic compounds, oxides (CrOx and FeOx) and carbon-based impurities.

2. **deposition parameters *vs.* material properties**

- The material properties of the as-deposited coatings (from an all-aqueous electrolyte) were evaluated in dependence of morphology and composition variations, and then compared to metallurgical austenitic steels. Current density, thus overpotential, was the main parameter affecting the electrodeposits, varying mainly their chromium content. At highly negative potential iron and nickel were in the diffusion limited region, whereas chromium in the charge-transfer/mixed region. Regardless of the amount of chromium, the as-deposited coatings were all amorphous with a slight tendency to ultrafine-grained α-Fe phase. The FeCrNi electrodeposits with chromium content around 24-29 wt% (effective metallic Cr 17 at% from XPS) showed good passivation in acidic media similar to standard metallurgical AISI SS. Bio-compatibility, measured by cytotoxicity tests, was comparable for both electrodeposits and austenitic steels. The coatings were found to have tuneable soft-magnetic behaviour in dependence of the amount of chromium: saturation magnetisation increased from zero up to 662 emu cm^{-3} by varying the chromium content from 34 to 4 wt%. However, tribological tests (dry friction conditions) revealed that the material was hard but rather brittle, producing various ruptures of the electrodeposit along the wear tracks. Here, the main issues were correlated to strong HER leading to low deposition efficiencies, brittleness and porosity, therefore making the electrodeposition of such material inside miniaturised templates extremely challenging.

- In order to overcome some of the understood issues of such electrochemical system, different improvements were addressed, finding the use of a mixed-solvent electrolyte as the best solution. A mixed-solvent electrolyte composed of ethylene glycol (EG) was investigated and compared to the all-aqueous one, showing similar Cr(III)-glycine complexation, but higher deposition efficiency because of the reduced impact of the HER at the cathode during plating, therefore lessening porosity and brittleness.
  Afterwards, a comparison of the material's properties was pursued for electrodeposited FeCrNi coatings: as-deposited (amorphous) and annealed (nano-crystalline) produced from both studied electrolytes (all-aqueous and mixed-solvent), and then also including metallurgical austenitic SS. This investigation was done in order to correlate electrolyte type, coatings' chemical composition/microstructure/morphology, to other characteristic properties, *i.e.* corrosion resistance, biocompatibility, magnetic and mechanical properties.
  Similar results, with little variations, were obtained in terms of corrosion

resistance, bio-compatibility and magnetic response, regardless of the electrolyte used. The mechanical tests showed that all as-deposited coatings had very high hardness (up to 8.3 GPa) and young modulus (up to 171 GPa) which was dependent on the amount of incorporated carbon-based impurities, whereas the variation in mechanical behaviour for annealed films was not completely explained.

3. **architecture design *vs.* material properties**

   - The last objective was to study the way to obtain micro- nanocomponents made of FeCrNi from electrodeposition process, which could be advantageous for creating MEMS/NEMS with tunable properties in order to be adopted for innovative bio-medical/micro-robotics applications. The EG-based mixed-solvent electrolyte was found to be an effective and feasible solution for obtaining FeCrNi micro- and nanocomponents *via* template assisted electrodeposition. For the first time, FeCrNi nanotubes (NTs) and nanowires (NWs) were achieved by electroplating into AAO templates: high applied current density resulted in NTs, whereas low current density in compact NWs with homogeneous composition along the wire length. This deposition phenomenon could be explained and compared well with kinetic and growth models present in literature for single metals electrodeposited into nano-moulds. In addition, FeCrNi micro-pillars were created by electroplating inside UV-LIGA moulds combining mixed-solvent electrolyte and cyclic CV-like deposition (sweeping the potential in the Fe-Cr-Ni electroreduction window), avoiding the delamination of moulds during plating caused by the combination of HER and under-deposition.

Future work and outlook

The electrodeposition of FeCrNi coatings from a mixed-solvent EG Cr(III)-based electrolyte was shown to be promising for decreasing the impact of HER, and thus to be a valid solution for depositing inside micro- and nanotemplates. However, some of the material properties are not fully understood yet, needing further investigation. In particular, the next step would be to study more in details the relations between mechanical properties, composition/microstructure/-morphology of the coatings by combining XRD phase analysis, EBSD and TEM techniques. Then, performing corrosion measurements in other medium (*e.g.* chlorine-based) would be beneficial to observe better other types of corrosion, such as pitting. Eventually, a future work could be the addition of molybdenum in the electrolyte (therefore in the final material) in order to improve the material's corrosion resistance, *i.e.* for pitting corrosion (although, making the studied system even more complex).

Moreover, because of time issue, it was not possible to analyse the material properties of miniaturised components like FeCrNi NWs/NTs and micro-pillars. In the future, it would be interesting to further investigate the relation between architecture design (*i.e.* minimum dimension and geometry), microstructure and other material properties. This could be done by analysing more sophisticated micro- nanocomponents and/or with different architectures (*e.g.* multi-layers), in which size effects and interfaces play an important role with respect to the final material properties at such micro- nano scales. Finally, it would be great to compare those results with the ones obtained for electrodeposited FeCrNi coatings.

A Supporting information

A.1 Electrodeposition of FeCrNi films: role of impurities and electroreduction mechanisms

A.1.1 Anode role investigation

Morphology

Pictures of the various samples (Figure A.1) show the variation in colour due to the use of different anode material in both as-deposited and annealed cases.

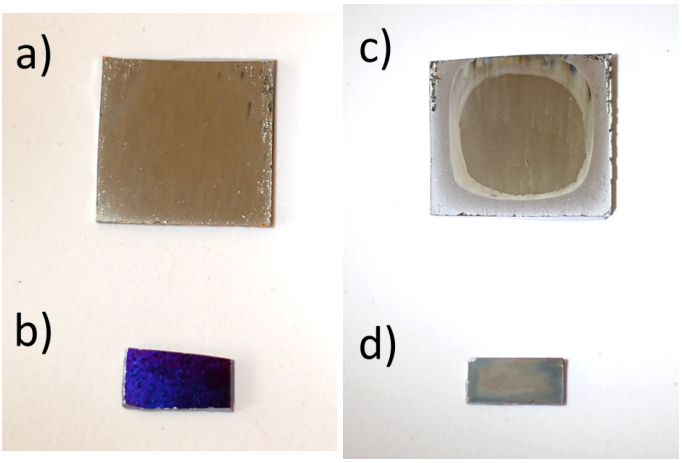

Figure A.1 – Pictures of electrodeposited FeCrNi coatings: *Pt anode* cases (a) as-deposited and (b) annealed; *Ni anode* cases (c) as-deposited and (d) annealed.

X-ray photoelectron spectroscopy (XPS)

The signal from the *Pt anode* and *Ni anode* as-deposited samples are similar, therefore they possess comparable peak fittings.

At surface level, the carbon C 1s signal can be divided into three peaks (Figure A.2a and A.3a), *i.e.* C-C and/or C-H at 284.8 eV, C-OH at 286.4 eV and C=O groups at 288.6 eV. The oxygen O 1s peak at 529.5 eV is attributed to metal oxides. The transition at 531.3 eV may be associated to carboxylic (C-OH, -COOH) and/or hydroxyl (-OH; metal hydroxides) groups, whereas the peak at 532.5 eV may be linked to carbonyl groups (C=O). The spectral components of Fe $2p_{3/2}$ possess BEs of 709.5, 711.7 and 714.8 eV. The first and third BE values may be attributed to iron oxide (FeO) and its satellite peaks, while the second transition matches iron in hydroxide form (FeOOH). The chromium Cr $2p_{3/2}$ signal

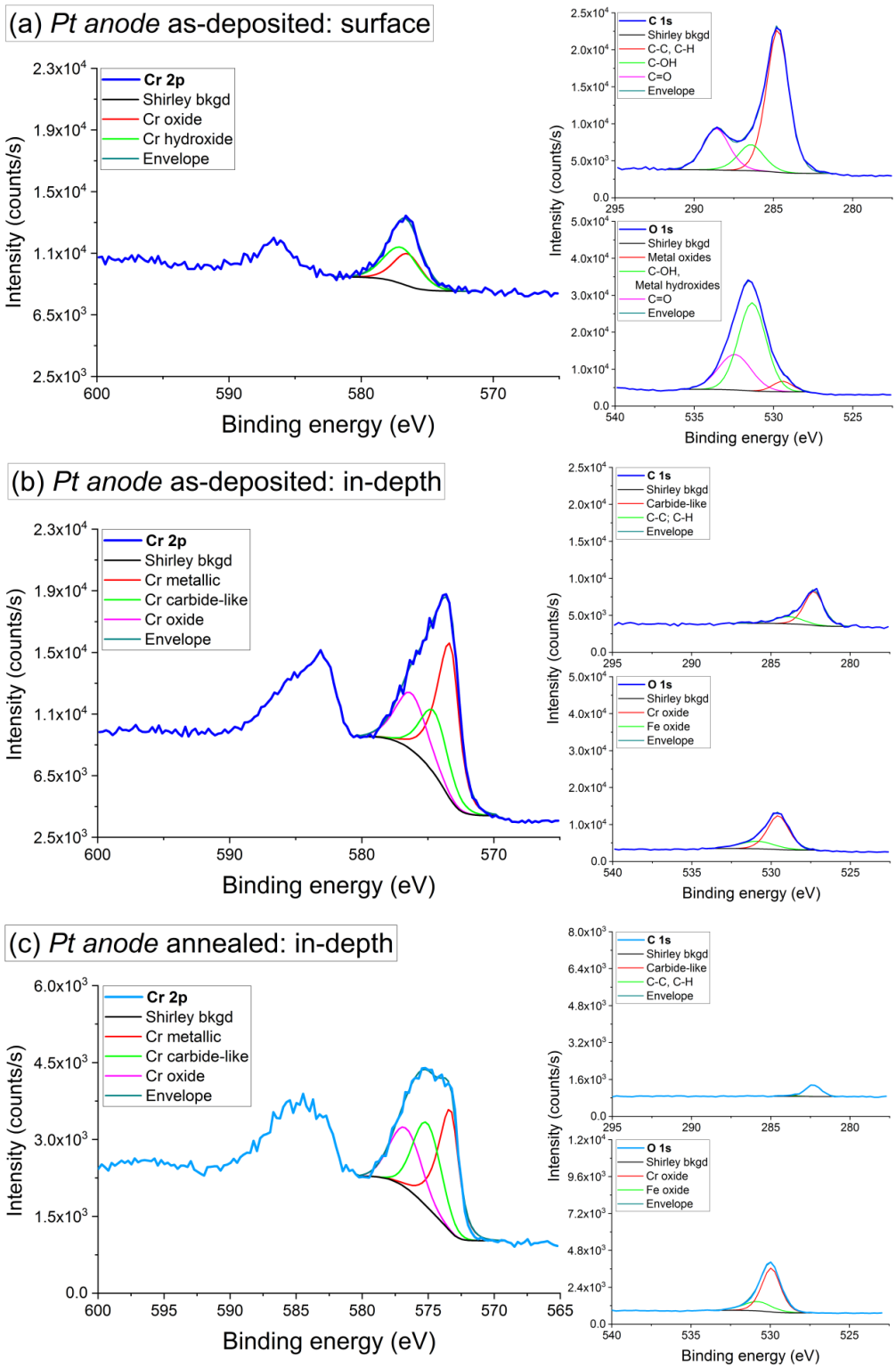

Figure A.2 – Cr 2p, C 1s and O 1s XPS fitted spectra of electrodeposited *Pt anode* FeCrNi film: (a) surface and (b) in-depth (approx. 50 min sputtering) contributions of the as-deposited sample; (c) in-depth (approx. 50 min sputtering) results of the annealed case.

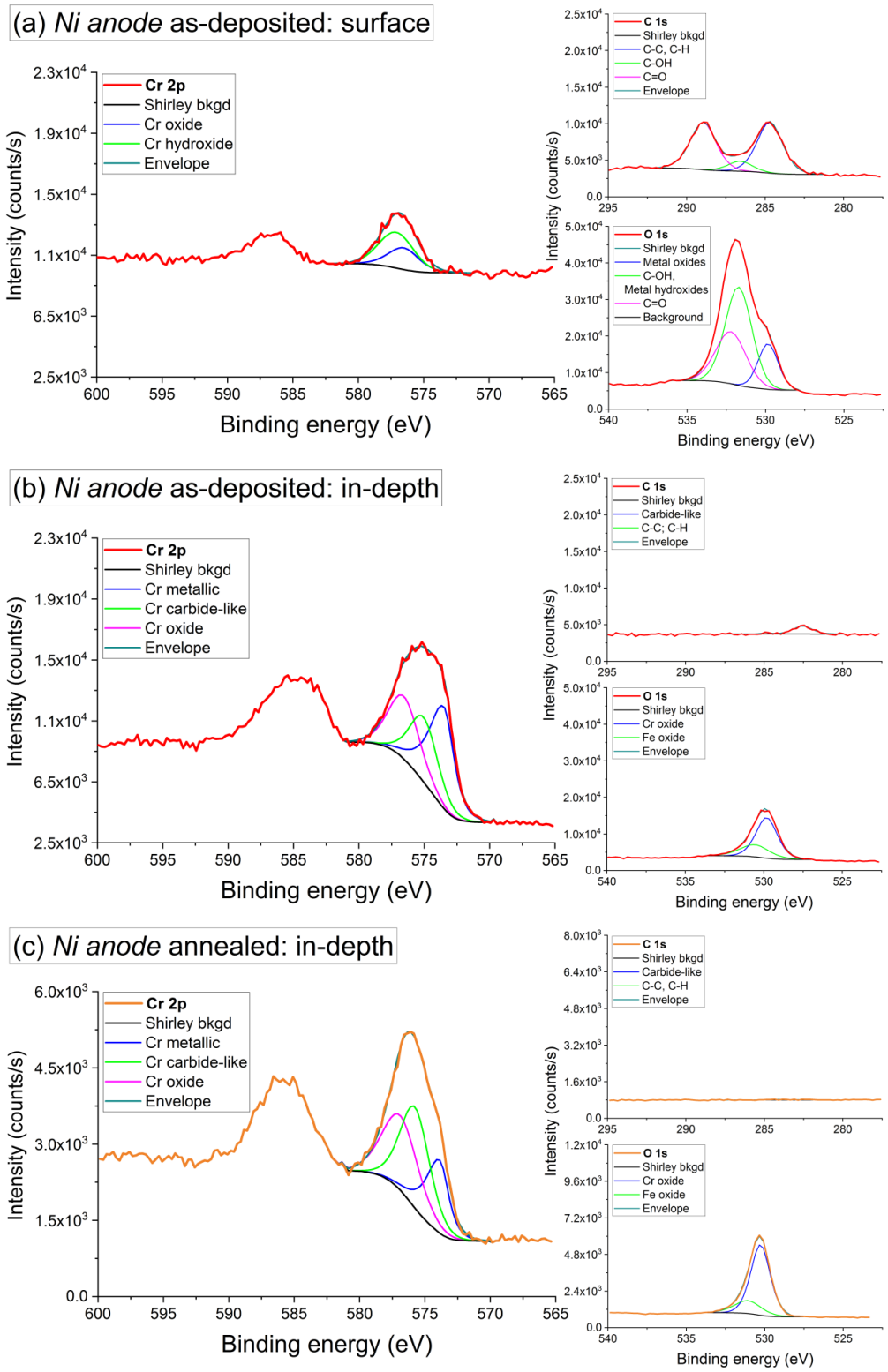

Figure A.3 – Cr 2p, C 1s and O 1s XPS fitted spectra of electrodeposited *Ni anode* FeCrNi film: (a) surface and (b) in-depth (approx. 50 min sputtering) contributions of the as-deposited sample; (c) in-depth (approx. 50 min sputtering) results of the annealed case.

(Cr 2p spectra in Figure A.2a and A.3a) can be deconvoluted into two major peaks, *i.e.* at 576.2 eV and ≈ 577 eV corresponding to Cr_2O_3 and $Cr(OH)_3$, respectively [159]. Interestingly, only the *Ni anode* FeCrNi coating exhibits a distinguishable Ni $2p_{3/2}$ signal on the surface (figure not shown), attributed to nickel oxide, with two main peaks at 853.4 and 856.0 eV and two broad satellites at 860.5 and 863.8 eV [160]. In depth of the coating (Figure A.2b and A.3b), the O 1s spectral components can be fitted assuming two contributions. The first, located at 529.7 eV, is assigned to chromium oxide, whereas the second at 530.6 eV may be associated with iron oxide. The well-resolved C 1s peak at 282.5 eV may be associated to chromium carbide (Cr_3C_2) [118] or a carbide-like metallic mixture. This is partially confirmed by the Cr $2p_{3/2}$ spectra, in which three peaks fit the signal at BEs of 573.4, 574.6 and 576.3 eV, corresponding to metallic chromium, carbide-like bond (Cr-C) and chromium oxide (most probably Cr_2O_3), respectively. However, it is difficult to separate the two contributions as the chromium carbides and oxides are so close to one another. Even though the amount of nitrogen within the coating is minimal, a peak is still registered at 396.7 eV, most probably associated with chromium nitride (CrN) [161] or nitride-like bond to chromium (Cr-N). In contrast, the chemical state of iron is mainly metallic with a well-defined peak at 706.5 eV and a small convoluted peak at approx. 711 eV, possibly linked to magnetite (Fe_3O_4). Likewise, Ni $2p_{3/2}$ core-level XPS spectra present a typical metallic peak fitting (BE at 852.1 eV and two satellites at 856.6 and 858.6 eV). After annealing, the samples surfaces were heavily cracked and damaged, probably caused by the occurrence of hydrogen degassing and crack expansion. For this reason, the XPS spectra were only evaluated after sputtering, in-depth of the coating. In the case of the *Pt anode* FeCrNi film, all elements have similar peak fitting as in the as-deposited sample, however, with different intensities (Figure A.2c). The overall oxidation signals (oxide and carbide-like) increased and became comparable to the metallic signals. Here, the contribution of nitrogen is weak, however the BE at 396.2 eV may correspond to a nitride-like bonding. In contrast, the annealed *Ni anode* FeCrNi film shows neither carbon nor nitrogen peaks. The remaining elements (*i.e.* Fe, Cr, Ni and O) have identical peak fitting as for the as-deposited counterpart, although the metallic chromium signal (Figure A.3c) is rather low in comparison to the enhanced contribution from oxide and carbide-like states.

Table A.1 shows the atomic weights for the different elements as a function of their oxidation state, evaluated in-depth of the coating (approx. 50 min sputtering time). The Fe to O stoichiometric ratio is approx. 3 to 4 in all cases, which confirms that the iron oxide is in the Fe_3O_4 form. It is difficult to put forward definite conclusions regarding chromium, due to complex peak fitting. For the oxide, in all cases the Cr to O proportion is 1:3, which is in contrast with both fitting of Cr 2p and O 1s, stating chromium oxide is in the Cr_3C_2 form. Instead, chromium to carbon stoichiometric ratio (Cr:C) considering carbide-like contributions, shows

Table A.1 – Atomic weight of Fe-Cr-Ni-O-C-N in function of oxidation states from XPS peaks fitting of electrodeposited FeCrNi: *Pt anode* and *Ni anode*, as-deposited and annealed films, analysed in-depth.

Sample	Fe (at%)		Cr (at%)		Ni (at%)		O (at%)		C (at%)		N (at%)	
Pt anode as-dep.	Fe met. Fe ox.	34.5 3.3	Cr met. Cr-C Cr ox.	8.0 3.9 3.9	Ni met.	11.7	Cr ox. Fe ox.	12.4 4.4	Carbide-like Cr-C, C-H	12.5 3.9	Nitride-like	1.5
Ni anode as-dep.	Fe met. Fe ox.	31.5 3.7	Cr met. Cr-C Cr ox.	6.5 4.4 4.6	Ni met.	21.0	Cr ox. Fe ox.	15.8 6.4	Carbide-like Cr-C, C-H	3.9 0.3	Nitride-like	1.9
Pt anode annealed	Fe met. Fe ox.	32.2 3.8	Cr met. Cr-C Cr ox.	9.3 7.8 6.2	Ni met.	10.3	Cr ox. Fe ox.	16.7 5.3	Carbide-like Cr-C, C-H	6.0 0.5	Nitride-like	1.9
Ni anode annealed	Fe met. Fe ox.	22.0 4.5	Cr met. Cr-C Cr ox.	5.9 9.9 8.9	Ni met.	14.6	Cr ox. Fe ox.	26.1 6.5	Carbide-like Cr-C, C-H	0.5 0.3	Nitride-like	0.8

much broader variations: *Pt anode* as-deposited (C16.4 at%) Cr:C is 1:3, *Pt anode* annealed (C6.5 at%) Cr:C is 1:1, *Ni anode* as-deposited (C4.2 at%) Cr:C is 1:1 and *Ni anode* annealed (C0.8 at%) Cr:C is 20:1. These differences may also be associated to a partial superimposition of the Cr-C contribution with the chromium oxide one, making the presence of Cr_3C_2 more probable. Nevertheless, the material can still be considered as stainless steel-like FeCrNi, having metallic stoichiometric proportion (Fe:Cr:Ni) similar to austenitic stainless steel.

A.1.2 Investigation of Cr(III) complexation

X-ray photoelectron spectroscopy (XPS)

In terms of oxidation states from XPS analysis in-depth, the *Standard* electrolyte cases are similar to the previously described *Pt anode* sample. From Table A.2, it can be seen that current density amplification only affects metal contributions, mainly chromium, passing from 5.9 to 10.1 at% from lower to higher applied current density and does not affect the carbide and oxide contributions. For the coating obtained from the *No Cr-Glycine* bath, no visible peaks were registered for the carbon and nitrogen signals and the oxygen O 1s spectral component was fitted with a low intensity peak at BE of 530.6 eV, associated to iron oxide (magnetite or hematite). Nickel is present in metal form, the Fe 2p spectra with respect to the *Standard* electrolyte sample shows that the metal contribution slightly decreases, whereas the oxide is more pronounced (BE at 711.5 eV). When comparing the *No Cr* and *No Cr-Glycine* electrolyte films, spectra quantifications show that the glycine addition causes an increase in oxygen O 1s peak intensity (linked to iron oxides) and the carbon C 1s signal once more

Appendix A. Supporting information

Table A.2 – Atomic weight of Fe-Cr-Ni-O-C-N in function of oxidation states from XPS peaks fitting of electrodeposited FeCrNi: from *Standard*, *No Cr-Glycine* and *No-Cr* electrolytes, analysed in-depth.

Sample	Fe (at%)		Cr (at%)		Ni (at%)		O (at%)		C (at%)		N (at%)	
Standard (-60 mA cm^{-2})	Fe met. Fe ox.	37.1 3.8	Cr met. Cr-C Cr ox.	5.9 2.8 4.0	Ni met.	18.1	Cr ox. Fe ox.	11.3 4.9	Carbide-like C-C, C-H	10.8 0.4	Nitride-like	0.9
Standard (-80 mA cm^{-2})	Fe met. Fe ox.	37.1 4.0	Cr met. Cr-C Cr ox.	10.1 2.8 4.2	Ni met.	11.9	Cr ox. Fe ox.	11.3 5.9	Carbide-like C-C, C-H	9.2 1.9	Nitride-like	1.4
No Cr-Glycine (-80 mA cm^{-2})	Fe met. Fe ox.	20.8 7.7			Ni met.	68.8	Fe ox.	2.1	C-C, C-H	0.6		
No Cr (-80 mA cm^{-2})	Fe met. Fe ox.	32.9 9.8			Ni met.	39.1	Fe ox.	2.1	Carbide-like C-C, C-H	1.9 0.7	N	0.6

fits with a carbide peak (BE at 282.7 eV). It was observed that, iron and nickel $2p_{3/2}$ peaks are affected the most by the glycine addition (Table A.2), where the first increased (both metallic and oxide contributions) and the second significantly decreased.

Complexation study and chemical equilibrium diagrams

When taking into account the bath acidic pH ($\approx$ 1) and the dissociation constants of various molecules, the existing ions, not including metals, could possibly be:

- ammonium ($NH_4^+ \rightleftharpoons NH_3 + H^+$; pK_a = 9.25) [162]
- sodium (Na^+), chloride ($HCl \rightleftharpoons Cl^- + H^+$; pK_a = -5.9) [163]
- glycine cation $GlyH_2$ ($NH_3^+CH_2COOH \rightleftharpoons NH_2CH_2COOH + H^+$; pK_a = 2.34) [164]
- formaldehyde ($CH_2O \rightleftharpoons CHO^- + H^+$; pK_a = 13.27) [164]
- formic acid ($HCOOH \rightleftharpoons HCOO^- + H^+$; pK_a = 3.75) [164]

However, when considering the complex stability constants of metals and electrolytes ligand ions, monoligand Cr(III)-glycine complexation is favoured [50] ($log\beta$ = 8.4) [165] with respect to Fe(II) ($log\beta$ = 4.3) [165, 166] and Ni(II) ($log\beta$ = 6.2) [165] glycine complexes due to the bath preparation process [112]. In the presence of formic acid and/or carboxylate ions, these molecules are likely to complex with Ni(II) ($log\beta$ = 3.2) [167] and Fe(II) ($log\beta$ = 2.6) [167], however not with Cr(III) ($log\beta$ = 1.9) [168] as it is already linked to glycine.

In aqueous solution, the studied transition metal ions (*i.e.* Fe, Cr and Ni) are stable and take the form of hydrate complexes within the considered pH range, unless previously complexed by ligand molecules. However, hydrolysis is a common reaction when pH and/or temperature are increasing: for example, a rise in pH of above 5 at the cathode can lead to the formation of $Ni(OH)^+$ ($log\beta$ = 4.1) [169] and $Fe(OH)^+$ ($log\beta$ = 4.5) [169] hydroxides ions [40]. It is unlikely that Cr(III)-glycine complex will undergo hydrolysis, due to the low stability constant of Cr(III)-hydroxides ($Cr^{3+} \rightleftharpoons Cr(OH)^{2+} + H^+$; $log\beta$ = -4.2) [38], however this Cr(III)-hydroxo equilibrium can be shifted to the right at higher pH values at the cathode.

Chemical equilibrium diagrams extrapolated from Medusa software show that for the *No Cr* electrolyte with an ionic strength (I) of 2.79 M (Figure A.4a), Ni-glycine and iron hydroxides complexes are favoured when pH increases at the cathode surface. However, in case of *No Cr-Glycine* bath with I equal to 2.59 M (Figure A.4b), as expected, the most probable complexes to form with the increase in pH are nickel and iron hydroxides.

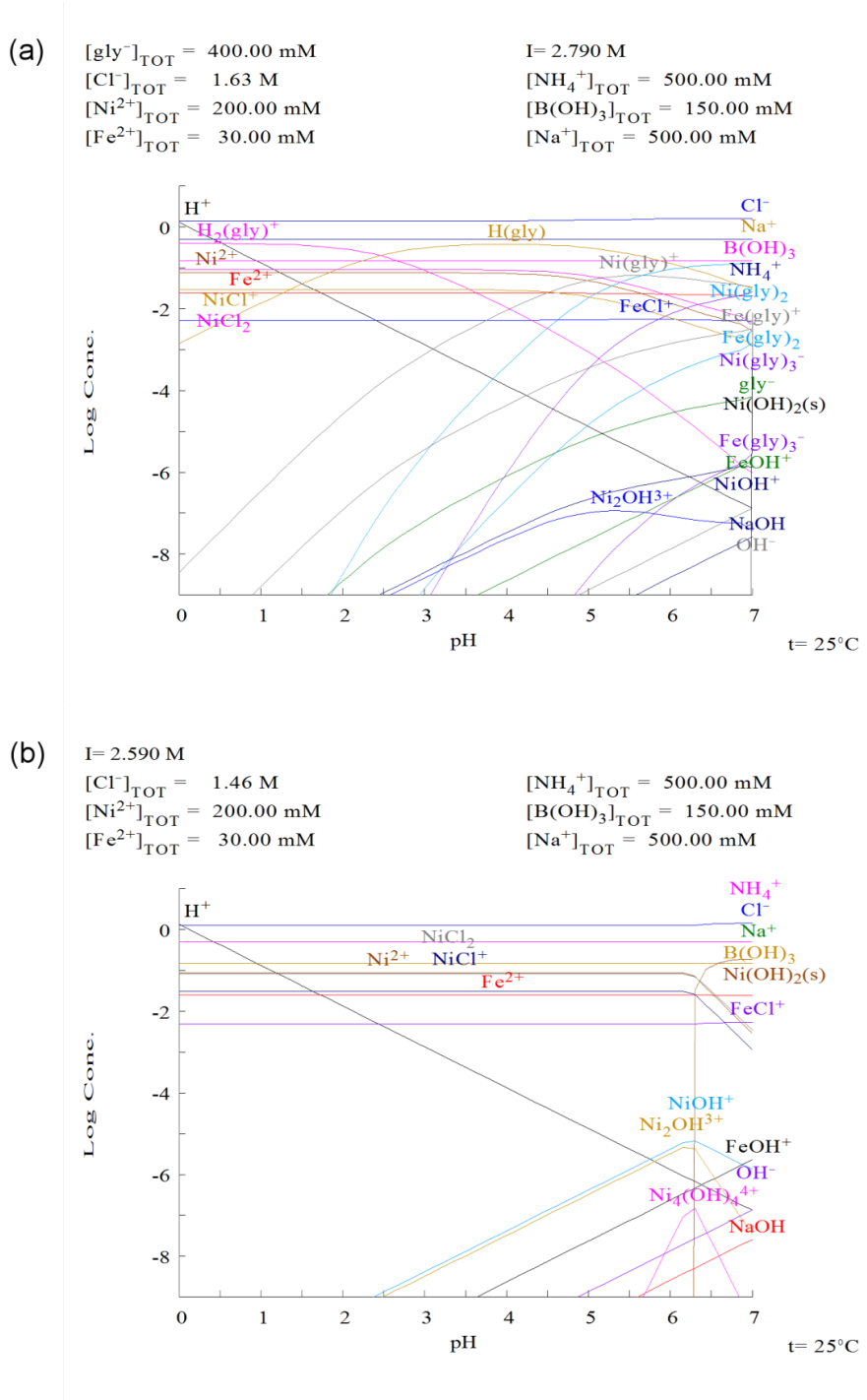

Figure A.4 – Chemical equilibrium diagrams obtained from Medusa software for (a) No Cr and (b) No Cr-Glycine electrolytes.

UV-vis absorbance spectra

The UV-vis absorption spectra were compared for the FeCrNi electrolytes (both fresh and galvanostatically aged) and the commercial chromium baths (Figure A.5). All FeCrNi electrolytes display similar peaks at wavelengths of λ_1 = 407 nm and λ_2 = 576 nm, corresponding to Cr(III) complexed with glycine [143, 144], confirming the results from Section A.1.2. A third contribution towards the UV region of the spectra ($\lambda_3 \approx$ 326 nm) seems to appear only after aging the solution using a platinum anode. Fresh commercial decorative trivalent chromium bath exhibits two maxima at 421 and 586 nm, which were identified as Cr(III) complexed with some other organic compounds (*e.g.* formic acid [170], oxalate [143], polyethylene glycol [141]) and these peaks are similar to the ones from FeCrNi, however, slightly shifted towards longer wavelengths. In comparison, hard hexavalent chromium bath shows a clear peak at 349 nm corresponding to Cr(VI) ions, as observed in other literature works [171–173]. The vicinity of this Cr(VI) contribution with respect to FeCrNi *Pt anode* aged electrolyte local maximum (λ_3) could denote the presence of Cr(VI) ions inside the FeCrNi solution, although the wavelength difference from Cr(VI) and FeCrNi λ_3 maxima is rather large ($\Delta\lambda \approx$ 25 nm). Another explanation is that aging leads to the formation of additional compounds inside the electrolyte, mainly uncomplexed glycine, which can oxidise at the anode to form formic acid or other carboxyl molecules. These compounds could be responsible for the increase in absorbance in the near UV region [174].

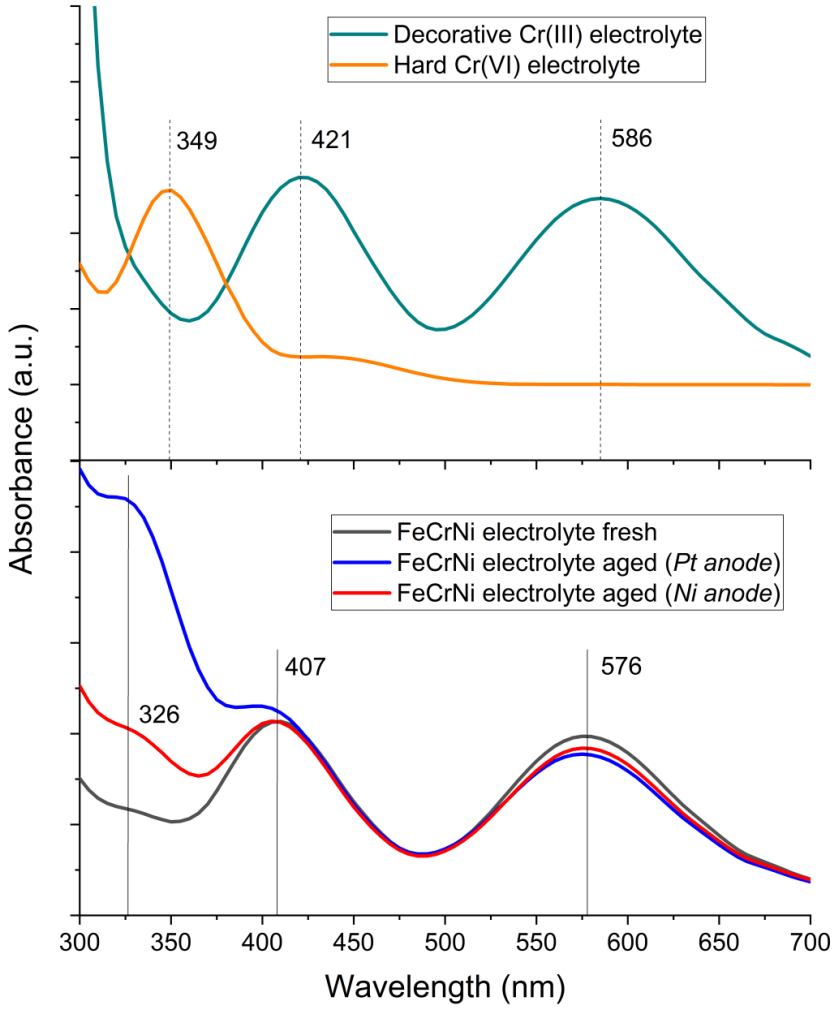

Figure A.5 – UV-vis absorption spectra of: (bottom) FeCrNi electrolytes and (top) commercial decorative trivalent and hard hexavalent chromium baths.

Bibliography

[1] D Clark, D Wood, and U Erb. Industrial applications of electrodeposited nanocrystals. *Nanostructured Materials*, 9(1):755–758, 1997.

[2] Mitsuo Niinomi. *Metals for biomedical devices*. Elsevier, 2010.

[3] Hendra Hermawan, Dadan Ramdan, and Joy RP Djuansjah. Metals for biomedical applications. In *Biomedical engineering-from theory to applications*. InTech, 2011.

[4] Kaufui V Wong and Aldo Hernandez. A review of additive manufacturing. *ISRN Mechanical Engineering*, 2012, 2012.

[5] Masayoshi SAWADA, Hayato KITA, and Masayuki SHIBUYA Kazuyoshi FUJISAWA. Development of austenitic stainless steel sheets for microfabrication.

[6] Usama M Attia and Jeffrey R Alcock. A review of micro-powder injection moulding as a microfabrication technique. *Journal of Micromechanics and microengineering*, 21(4):043001, 2011.

[7] RD Srivastava and RC Mukerjee. Electrodeposition of binary alloys: an account of recent developments. *Journal of Applied Electrochemistry*, 6(4):321–331, 1976.

[8] D Landolt. Electrodeposition science and technology in the last quarter of the twentieth century. *Journal of The Electrochemical Society*, 149(3):S9–S20, 2002.

[9] Jason Tam, Gino Palumbo, and Uwe Erb. Recent advances in superhydrophobic electrodeposits. *Materials*, 9(3):151, 2016.

[10] Alexander B Tesler, Philseok Kim, Stefan Kolle, Caitlin Howell, Onye Ahanotu, and Joanna Aizenberg. Extremely durable biofouling-resistant metallic surfaces based on electrodeposited nanoporous tungstite films on steel. *Nature communications*, 6:8649, 2015.

[11] Tetsuya Osaka, Madhav Datta, and Yosi Shacham-Diamand. *Electrochemical nanotechnologies*. Springer Science & Business Media, 2009.

[12] Paul Morisset, JW Oswald, CR Draper, R Pinner, and RA Ehrhardt. Chromium plating, 1955.

[13] European Parliament and European Chemicals Agency. Commission Regultion (EU) no 438/2013. *Official Journal of the European Union*, 57(1272), 2013.

[14] Abner Brenner. *Electrodeposition of alloys: principles and practice*. Elsevier, 2013.

[15] NV Myung, DY Park, M Schwartz, K Nobe, H Yang, CK Yang, and JW Judy. Electrodeposited hard magnetic thin films for mems applications. *Proc. Electrochem. Soc*, 20:29, 2000.

[16] LT Romankiw. A path: from electroplating through lithographic masks in electronics to liga in mems. *Electrochimica acta*, 42(20-22):2985–3005, 1997.

[17] Milan Paunovic and Mordechay Schlesinger. *Fundamentals of electrochemical deposition*. Wiley-Interscience, 2006.

[18] H Gerischer. Kinetik der elektrolytischen abscheidung und auflösung von metallen in wässriger lösung. *Electrochimica Acta*, 2(1-3):1–18, 1960.

[19] Tohru Watanabe. *Nano plating-microstructure formation theory of plated films and a database of plated films*. Elsevier, 2004.

[20] Mordechay Schlesinger and Milan Paunovic. *Modern electroplating*, volume 55. John Wiley & Sons, 2011.

[21] Thomas F Fuller and John N Harb. *Electrochemical engineering*. John Wiley & Sons, 2018.

[22] Giovanni Zangari. Electrodeposition of alloys and compounds in the era of microelectronics and energy conversion technology. *Coatings*, 5(2):195–218, 2015.

[23] Fernando Carlos Alvira, L Ponce Cabrera, Y Peñaloza Mendoza, ML Martinez Ricci, and F Videla. Pulsed laser deposition of pbte under monopulse and multipulse regime. *Optics and Lasers in Engineering*, 90:284–290, 2017.

[24] TC Franklin. Some mechanisms of action of additives in electrodeposition processes. *Surface and Coatings Technology*, 30(4):415–428, 1987.

[25] L Oniciu and L Mureşan. Some fundamental aspects of levelling and brightening in metal electrodeposition. *Journal of applied electrochemistry*, 21(7):565–574, 1991.

[26] Y Tsuru, M Nomura, and FR Foulkes. Effects of boric acid on hydrogen evolution and internal stress in films deposited from a nickel sulfamate bath. *Journal of Applied Electrochemistry*, 32(6):629–634, 2002.

[27] Niels Hansen. Hall–petch relation and boundary strengthening. *Scripta Materialia*, 51(8):801–806, 2004.

[28] Julia R Greer. Nanotwinned metals: It's all about imperfections. *Nature materials*, 12(8):689–690, 2013.

[29] A John Sedriks. *Corrosion of stainless steel*. John Wiley & Sons, 1996.

[30] Farzad Nasirpouri. *Electrodeposition of Nanostructured Materials*. Springer, 2017.

[31] M Kraack, H Boehni, W Muster, and J Patscheider. Influence of molybdenum on the corrosion properties of stainless steel films. *Surface and Coatings Technology*, 68:541–545, 1994.

[32] WB Nowak. Microcrystalline/amorphous iron alloy films for corrosion-resistant coatings. *Materials Science and Engineering*, 23(2-3):301–305, 1976.

[33] RB Inturi and Z Szklarska-Smialowska. Localized corrosion of nanocrystalline 304 type stainless steel films. *Corrosion*, 48(5):398–403, 1992.

[34] Daheum Kim, D-Y Park, BY Yoo, PTA Sumodjo, and NV Myung. Magnetic properties of nanocrystalline iron group thin film alloys electrodeposited from sulfate and chloride baths. *Electrochimica Acta*, 48(7):819–830, 2003.

[35] H Gleiter. Nanostructured materials: basic concepts and microstructure. *Acta materialia*, 48(1):1–29, 2000.

[36] VS Protsenko and FI Danilov. Chromium electroplating from trivalent chromium baths as an environmentally friendly alternative to hazardous hexavalent chromium baths: comparative study on advantages and disadvantages. *Clean Technologies and Environmental Policy*, 16(6):1201–1206, 2014.

[37] S Mahdavi and SR Allahkaram. Composition, characteristics and tribological behavior of cr, co–cr and co–cr/tio 2 nano-composite coatings electrodeposited from trivalent chromium based baths. *Journal of Alloys and Compounds*, 635:150–157, 2015.

[38] NV Mandich. Chemistry & theory of chromium deposition: Part 1–chemistry. *Plating and surface finishing*, 84(5):108–115, 1997.

[39] H Dahms and IM Croll. The anomalous codeposition of iron-nickel alloys. *Journal of the Electrochemical Society*, 112(8):771–775, 1965.

[40] Wendy C Grande and Jan B Talbot. Electrodeposition of thin films of nickel-iron. *Journal of the Electrochemical Society*, 140(3):669–681, 1993.

[41] Michael Matlosz. Competitive adsorption effects in the electrodeposition of iron-nickel alloys. *Journal of the Electrochemical Society*, 140(8):2272–2279, 1993.

[42] V Protsenko and Fr Danilov. Kinetics and mechanism of chromium electrodeposition from formate and oxalate solutions of cr (iii) compounds. *Electrochimica Acta*, 54(24):5666–5672, 2009.

[43] Anil Baral and Robert Engelken. Modeling, optimization, and comparative analysis of trivalent chromium electrodeposition from aqueous glycine and formic acid baths. *Journal of the electrochemical society*, 152(7):C504–C512, 2005.

[44] FI Danilov and VS Protsenko. Kinetics and mechanism of chromium electroplating from cr (iii) baths. *Protection of Metals*, 37(3):223–228, 2001.

[45] SH White and UM Twardoch. The chemistry and electrochemistry associated with the electroplating of group via transition metals. *Journal of applied Electrochemistry*, 17(2):225–242, 1987.

[46] YB Song and D-T Chin. Current efficiency and polarization behavior of trivalent chromium electrodeposition process. *Electrochimica Acta*, 48(4):349–356, 2002.

[47] S Survilienė, O Nivinskienė, A Češunienė, and A Selskis. Effect of cr (iii) solution chemistry on electrodeposition of chromium. *Journal of Applied Electrochemistry*, 36(6):649–654, 2006.

[48] DR Gabe. The role of hydrogen in metal electrodeposition processes. *Journal of Applied Electrochemistry*, 27(8):908–915, 1997.

[49] Zenmi Tu, Zhelong Yang, Jingshuang Zhang, Mao-Zhong An, and Wen-Llang Li. Cathode polarization in trivalent chromium plating. *Plating and Surface Finishing*, 80:79–79, 1993.

[50] J McDougall, M El-Sharif, and S Ma. Chromium electrodeposition using a chromium (iii) glycine complex. *Journal of applied electrochemistry*, 28(9):929–934, 1998.

[51] J-C Kang, SB Lalvani, and CA Melendres. Electrodeposition and characterization of amorphous fe-ni-cr-based alloys. *Journal of applied electrochemistry*, 25(4):376–383, 1995.

[52] MR El-Sharif, A Watson, and CU Chisholm. The sustained deposition of thick coatings of chromium/nickel and chromium/nickel/iron alloys and their properties. *Transactions of the IMF*, 66(1):34–40, 1988.

[53] Feng Wang and Tohru Watanabe. Preparation and characterization of the electrodeposited fe–cr alloy film. *Materials Science and Engineering: A*, 349(1):183–190, 2003.

[54] M El-Sharif, J McDougall, and CU Chisholm. Electrodeposition of thick chromium coatings from an environmentally acceptable chromium (iii)-glycine complex. *Transactions of the IMF*, 77(4):139–144, 1999.

[55] M Ghorbani, A Dolati, R Ghasempour, et al. The effect of the cr and mo on the physical properties of electrodeposited ni–fe alloy films. *Journal of alloys and compounds*, 386(1):43–46, 2005.

[56] AG Dolati, M Ghorbani, and A Afshar. The electrodeposition of quaternary fe–cr–ni–mo alloys from the chloride-complexing agents electrolyte. part i. processing. *Surface and Coatings Technology*, 166(2):105–110, 2003.

[57] Lijian Xu, Jingjing Du, Shuxun Ge, Nongyue He, and Song Li. Preparation and characterization of nanocrystalline fe–ni–cr alloy electrodeposits on fe substrate. *Journal of applied electrochemistry*, 39(5):713–717, 2009.

[58] Daniel G Marangoni, Richard S Smith, and Sharon G Roscoe. Surface electrochemistry of the oxidation of glycine at pt. *Canadian Journal of Chemistry*, 67(5):921–926, 1989.

[59] Machu Willibald and Ghandour Mohamed Fathi Mahm El. Electrodepositing stainless steel coatings on metal surfaces, June 11 1963. US Patent 3,093,556.

[60] Malcolm J Law. Electrodeposition of chromium and chromium bearing alloys, September 9 1986. US Patent 4,610,763.

[61] Pamela Polinski and John Paulina. Stainless steel electrolytic coating, March 17 2003. US Patent App. 10/389,836.

[62] Grégoire Genolet and Hubert Lorenz. Uv-liga: From development to commercialization. *Micromachines*, 5(3):486–495, 2014.

[63] Chantal Khan Malek and Volker Saile. Applications of liga technology to precision manufacturing of high-aspect-ratio micro-components andsystems: a review. *Microelectronics journal*, 35(2):131–143, 2004.

[64] TE Buchheit, SH Goods, PG Kotula, and PF Hlava. Electrodeposited 80ni–20fe (permalloy) as a structural material for high aspect ratio microfabrication. *Materials Science and Engineering: A*, 432(1):149–157, 2006.

[65] Patrik Schürch, Laszlo Pethö, Jakob Schwiedrzik, Johann Michler, and Laetitia Philippe. Additive manufacturing through galvanoforming of 3d nickel

microarchitectures: Simulation-assisted synthesis. *Advanced Materials Technologies*, 3(12):1800274, 2018.

[66] Patrik Schürch, Rajaprakash Ramachandramoorthy, Laszlo Pethö, Johann Michler, and Laetitia Philippe. Additive manufacturing by template-assisted 3d electrodeposition: Nanocrystalline nickel microsprings and microspring arrays. *Applied Materials Today*, page 100472, 2019.

[67] Hong-Bo Sun and Satoshi Kawata. *Two-Photon Photopolymerization and 3D Lithographic Microfabrication*, pages 169–273. Springer Berlin Heidelberg, Berlin, Heidelberg, 2004.

[68] En-Shinn Wu, James H Strickler, William R Harrell, and Watt W Webb. Two-photon lithography for microelectronic application. In *Optical/Laser Microlithography V*, volume 1674, pages 776–782. International Society for Optics and Photonics, 1992.

[69] L Philippe and J Michler. A kinetic model enabling controlled electrosynthesis of stacked metallic nanotubes and nanowires. *Small*, 4(7):904–907, 2008.

[70] L Philippe, N Kacem, and J Michler. Electrochemical deposition of metals inside high aspect ratio nanoelectrode array: Analytical current expression and multidimensional kinetic model for cobalt nanostructure synthesis. *The Journal of Physical Chemistry C*, 111(13):5229–5235, 2007.

[71] Jaime Martín, Cristina V Manzano, and Marisol Martín-González. In-depth study of self-ordered porous alumina in the 140–400 nm pore diameter range. *Microporous and Mesoporous Materials*, 151:311–316, 2012.

[72] Jaime Martín, Cristina V Manzano, Olga Caballero-Calero, and Marisol Martín-González. High-aspect-ratio and highly ordered 15-nm porous alumina templates. *ACS applied materials & interfaces*, 5(1):72–79, 2012.

[73] Cristina V Manzano, J Martín, and Marisol S Martín-González. Ultra-narrow 12 nm pore diameter self-ordered anodic alumina templates. *Microporous and Mesoporous Materials*, 184:177–183, 2014.

[74] CV Manzano, JP Best, JJ Schwiedrzik, A Cantarero, J Michler, and L Philippe. The influence of thickness, interpore distance and compositional structure on the optical properties of self-ordered anodic aluminum oxide films. *Journal of Materials Chemistry C*, 4(32):7658–7666, 2016.

[75] A Saedi and M Ghorbani. Electrodeposition of ni–fe–co alloy nanowire in modified aao template. *Materials Chemistry and Physics*, 91(2-3):417–423, 2005.

[76] Hui Pan, Binghai Liu, Jiabao Yi, Cheekok Poh, Sanhua Lim, Jun Ding, Yuanping Feng, CHA Huan, and Jianyi Lin. Growth of single-crystalline ni and co nanowires via electrochemical deposition and their magnetic properties. *The Journal of Physical Chemistry B*, 109(8):3094–3098, 2005.

[77] Jian Qin, Josep Nogués, Maria Mikhaylova, Anna Roig, Juan S Munoz, and Mamoun Muhammed. Differences in the magnetic properties of co, fe, and ni 250- 300 nm wide nanowires electrodeposited in amorphous anodized alumina templates. *Chemistry of materials*, 17(7):1829–1834, 2005.

[78] Wagner de Oliveira da Rosa, Laura G Vivas, Kleber Roberto Pirota, Agustina Asenjo, and M Vázquez. Influence of aspect ratio and anisotropy distribution in ordered coni nanowire arrays. *Journal of Magnetism and Magnetic Materials*, 324(22):3679–3682, 2012.

[79] S Thongmee, HL Pang, J Ding, JB Yi, and JY Lin. Fabrication and magnetic properties of metal nanowires via aao templates. In *2008 2nd IEEE International Nanoelectronics Conference*, pages 1116–1120. IEEE, 2008.

[80] I Dobosz, W Gumowska, and M Czapkiewicz. Magnetic properties of co-fe nanowires electrodeposited in pores of alumina membrane. *Archives of Metallurgy and Materials*, 58(3):663–671, 2013.

[81] D Li and E Podlaha. Template-assisted electrodeposition of fe-ni-co nanowires: Effects of electrolyte ph and sodium lauryl sulfate. *Journal of The Electrochemical Society*, 164(13):D843–D851, 2017.

[82] NB Chaure and JMD Coey. Fabrication and characterization of electrodeposited co1- xcrx nanowires. *Journal of magnetism and magnetic materials*, 303(1):232–236, 2006.

[83] K Maleki and Z Alemipour. Electrodeposition and characterization of nicr alloy nanowires. *Applied Physics A*, 123(6):397, 2017.

[84] M Najafi, Z Alemipour, I Hasanzadeh, A Aftabi, and S Soltanian. Influence of annealing temperature, electrolyte concentration and electrodeposition conditions on magnetic properties of electrodeposited co-cr alloy nanowires. *Journal of Superconductivity and Novel Magnetism*, 28(1):95–101, 2015.

[85] Klaus Stefan Drese. Design rules for electroforming in the liga process. *Journal of the Electrochemical Society*, 151(6):D39–D45, 2004.

[86] SK Griffiths, RH Nilson, A Ting, RW Bradshaw, WD Bonivert, and Jill M Hruby. Modeling electrodeposition for liga microdevice fabrication. *Microsystem technologies*, 4(2):98–101, 1998.

[87] Mohamed Gad-el Hak. *The MEMS handbook*. CRC press, 2001.

[88] S Mehdizadeh, JO Dukovic, PC Andricacos, LT Romankiw, and HY Cheh. The influence of lithographic patterning on current distribution: A model for microfabrication by electrodeposition. *Journal of the Electrochemical Society*, 139(1):78–91, 1992.

[89] S Valizadeh, JM George, Peter Leisner, and Lars Hultman. Electrochemical deposition of co nanowire arrays; quantitative consideration of concentration profiles. *Electrochimica Acta*, 47(6):865–874, 2001.

[90] Daniil A Bograchev, Vladimir M Volgin, and Alexey D Davydov. Simple model of mass transfer in template synthesis of metal ordered nanowire arrays. *Electrochimica Acta*, 96:1–7, 2013.

[91] Julia R Greer, Warren C Oliver, and William D Nix. Size dependence of mechanical properties of gold at the micron scale in the absence of strain gradients. *Acta Materialia*, 53(6):1821–1830, 2005.

[92] William D Nix. Mechanical properties of thin films. *Metallurgical and Materials Transactions A*, 20(11):2217–2245, 1989.

[93] Shoso Shingubara. Fabrication of nanomaterials using porous alumina templates. *Journal of Nanoparticle Research*, 5(1):17–30, 2003.

[94] Bobomurod Hamrakulov, KIM In-Soo, MG Lee, and BH Park. Electrodeposited ni, fe, co and cu single and multilayer nanowire arrays on anodic aluminum oxide template. *Transactions of Nonferrous Metals Society of China*, 19:s83–s87, 2009.

[95] W Schwarzacher, OI Kasyutich, PR Evans, MG Darbyshire, Ge Yi, VM Fedosyuk, F Rousseaux, E Cambril, and D Decanini. Metal nanostructures prepared by template electrodeposition. *Journal of magnetism and magnetic materials*, 198:185–190, 1999.

[96] Evin Gultepe, Dattatri Nagesha, Srinivas Sridhar, and Mansoor Amiji. Nanoporous inorganic membranes or coatings for sustained drug delivery in implantable devices. *Advanced drug delivery reviews*, 62(3):305–315, 2010.

[97] Sang Jun Son, Xia Bai, and Sang Bok Lee. Inorganic hollow nanoparticles and nanotubes in nanomedicine: Part 1. drug/gene delivery applications. *Drug Discovery Today*, 12(15):650–656, 2007.

[98] Sang Jun Son, Jonathan Reichel, Bo He, Mattan Schuchman, and Sang Bok Lee. Magnetic nanotubes for magnetic-field-assisted bioseparation, biointeraction, and drug delivery. *Journal of the American Chemical Society*, 127(20):7316–7317, 2005.

[99] J Zhang, MD Baró, E Pellicer, and J Sort. Electrodeposition of magnetic, superhydrophobic, non-stick, two-phase cu–ni foam films and their enhanced performance for hydrogen evolution reaction in alkaline water media. *Nanoscale*, 6(21):12490–12499, 2014.

[100] Muhammad A Zeeshan, Roman Grisch, Eva Pellicer, Kartik M Sivaraman, Kathrin E Peyer, Jordi Sort, Berna Özkale, Mahmut S Sakar, Bradley J Nelson, and Salvador Pané. Hybrid helical magnetic microrobots obtained by 3d template-assisted electrodeposition. *Small*, 10(7):1284–1288, 2014.

[101] DR Gabe and JM West. Internal stress and cracking in electrodeposited chromium. *Transactions of the IMF*, 40(1):197–204, 1963.

[102] Laetitia Philippe, C Heiss, and J Michler. Electroplating of stainless steel. *Chemistry of Materials*, 20(10):3377–3384, 2008.

[103] Margarita Zakharova, Vitor Vlnieska, Heike Fornasier, Martin Börner, Tomy dos Santos Rolo, Jürgen Mohr, and Danays Kunka. Development and characterization of two-dimensional gratings for single-shot x-ray phase-contrast imaging. *Applied Sciences*, 8(3):468, 2018.

[104] Saulius Gražulis, Daniel Chateigner, Robert T Downs, AFT Yokochi, Miguel Quirós, Luca Lutterotti, Elena Manakova, Justas Butkus, Peter Moeck, and Armel Le Bail. Crystallography open database–an open-access collection of crystal structures. *Journal of applied crystallography*, 42(4):726–729, 2009.

[105] N Fairley. Casaxps: Spectrum processing software for xps, aes and sims; casa software ltd., uk, 2005.

[106] Michael Nastasi, James W Mayer, and Yongqiang Wang. *Ion beam analysis: fundamentals and applications*. CRC Press, 2014.

[107] Katherine P Rice, Yimeng Chen, Robert M Ulfig, Dan Lenz, Joseph Bunton, Mike van Dyke, and David J Larson. Atom probe tomography with the easier to operate eikos™. *Microscopy and Microanalysis*, 23(S1):42–43, 2017.

[108] Ignasi Puigdomenech. Hydra/medusa chemical equilibrium database and plotting software. *KTH Royal Institute of Technology*, 2004.

[109] Tongfan Sun and Amyn S Teja. Density, viscosity, and thermal conductivity of aqueous ethylene, diethylene, and triethylene glycol mixtures between 290 k and 450 k. *Journal of Chemical & Engineering Data*, 48(1):198–202, 2003.

[110] Warren Carl Oliver and George Mathews Pharr. An improved technique for determining hardness and elastic modulus using load and displacement sensing indentation experiments. *Journal of materials research*, 7(6):1564–1583, 1992.

[111] HM Ledbetter and MW Austin. Effects of carbon and nitrogen on the elastic constants of aisi type 304 stainless steel. *Materials Science and Engineering*, 70:143–149, 1985.

[112] Madoka Hasegawa, Songhak Yoon, Gaylord Guillonneau, Yucheng Zhang, Cédric Frantz, Christoph Niederberger, Anke Weidenkaff, Johann Michler, and Laetitia Philippe. The electrodeposition of fecrni stainless steel: microstructural changes induced by anode reactions. *Physical Chemistry Chemical Physics*, 16(47):26375–26384, 2014.

[113] George E Totten. *Steel heat treatment: metallurgy and technologies*. CRC press, 2006.

[114] S Ghaziof, MA Golozar, and K Raeissi. Characterization of as-deposited and annealed cr–c alloy coatings produced from a trivalent chromium bath. *Journal of Alloys and Compounds*, 496(1-2):164–168, 2010.

[115] Enrico Bertero, Cristina V Manzano, Eva Pellicer, Jordi Sort, Robert M Ulfig, Stefano Mischler, Johann Michler, and Laetitia Philippe. 'green'cr (iii)–glycine electrolyte for the production of fecrni coatings: electrodeposition mechanisms and role of by-products in terms of coating composition and microstructure. *RSC Advances*, 9(44):25762–25775, 2019.

[116] Enrico Bertero, Madoka Hasegawa, Samuel Staubli, Eva Pellicer, Inge K Herrmann, Jordi Sort, Johann Michler, and Laetitia Philippe. Electrodeposition of amorphous fe-cr-ni stainless steel alloy with high corrosion resistance, low cytotoxicity and soft magnetic properties. *Surface and Coatings Technology*, 349:745–751, 2018.

[117] Fu Su Yen, Wei Chien Chen, Janne Min Yang, and Chen Tsung Hong. Crystallite size variations of nanosized fe2o3 powders during γ-to α-phase transformation. *Nano Letters*, 2(3):245–252, 2002.

[118] K Petkov, V Krastev, and Ts Marinova. Xps analysis of thin chromium films. *Surface and interface analysis*, 18(7):487–490, 1992.

[119] JL Jordan, CA Kovac, JF Morar, and RA Pollak. High-resolution photoemission study of the interfacial reaction of cr with polyimide and model polymers. *Physical Review B*, 36(3):1369, 1987.

[120] Herbert H Uhlig. Passivity in metals and alloys. *Corrosion science*, 19(11):777–791, 1979.

[121] Norio Sato. An overview on the passivity of metals. *Corrosion science*, 31:1–19, 1990.

[122] C-OA Olsson and D Landolt. Passive films on stainless steels—chemistry, structure and growth. *Electrochimica acta*, 48(9):1093–1104, 2003.

[123] C Calinski and H-H Strehblow. Iss depth profiles of the passive layer on fe/cr alloys. *Journal of the Electrochemical Society*, 136(5):1328–1331, 1989.

[124] S Haupt and H-H Strehblow. A combined surface analytical and electrochemical study of the formation of passive layers on fecr alloys in 0.5 m h2so4. *Corrosion Science*, 37(1):43–54, 1995.

[125] L Felloni, S Sostero Traverso, GL Zucchini, and GP Cammarota. Investigation on the second anodic current maximum on the polarization curves of commercial stainless steels in sulphuric acid. *Corrosion Science*, 13(10):773–789, 1973.

[126] MS El-Basiouny and Shiro Haruyama. The polarization behaviour of fecr alloys in acidic sulphate solutions in the active region. *Corrosion Science*, 16(8):529–540, 1976.

[127] CD Kim and BE Wilde. Influence of cathodic pretreatment on theanodic dissolution kinetics of stainless steels in dilute acid media. *Corrosion science*, 10(10):735–744, 1970.

[128] J Porcayo-Calderon, M Casales-Diaz, VM Salinas-Bravo, and L Martinez-Gomez. Corrosion performance of fe-cr-ni alloys in artificial saliva and mouthwash solution. *Bioinorganic chemistry and applications*, 2015, 2015.

[129] S Atalay, H Gencer, and VS Kolat. Magnetic entropy change in fe 74- x cr x cu 1 nb 3 si 13 b 9 (x= 14 and 17) amorphous alloys. *Journal of non-crystalline solids*, 351(30):2373–2377, 2005.

[130] Yu Boliang, JMD Coey, M Olivier, and JO Ström-Olsen. Onset of magnetism in iron-chromium glasses. *Journal of applied physics*, 55(6):1748–1750, 1984.

[131] Eva Pellicer, Aïda Varea, Salvador Pané, Bradley J Nelson, Enric Menéndez, Marta Estrader, Santiago Surinach, Maria Dolors Baró, Josep Nogués, and Jordi Sort. Nanocrystalline electroplated cu–ni: metallic thin films with enhanced mechanical properties and tunable magnetic behavior. *Advanced functional materials*, 20(6):983–991, 2010.

[132] Shekhar Bhansali and Abhay Vasudev. *MEMS for biomedical applications*. Elsevier, 2012.

[133] Vyacheslav Protsenko, Lina Bobrova, and Felix Danilov. Trivalent chromium electrodeposition using a deep eutectic solvent. *Anti-Corrosion Methods and Materials*, 65(5):499–505, 2018.

[134] Gabriele Panzeri, Matteo Tresoldi, Luca Nobili, and Luca Magagnin. Electrodeposition of znni alloys from ethylene glycol/choline chloride based ionic liquid. *ECS Transactions*, 75(15):627–632, 2016.

[135] Andrea R Kim and Ramana G Reddy. Cobalt electrodeposition from cobalt chloride using urea and choline chloride ionic liquid: Effect of temperature, applied voltage, and cobalt chloride concentration on current efficiency and energy consumption. In *Applications of Process Engineering Principles in Materials Processing, Energy and Environmental Technologies*, pages 97–114. Springer, 2017.

[136] Andrew P Abbott, Azeez A Al-Barzinjy, Paul D Abbott, Gero Frisch, Robert C Harris, Jennifer Hartley, and Karl S Ryder. Speciation, physical and electrolytic properties of eutectic mixtures based on crcl 3· 6h 2 o and urea. *Physical Chemistry Chemical Physics*, 16(19):9047–9055, 2014.

[137] Wojciech Simka, Dagmara Puszczyk, and Ginter Nawrat. Electrodeposition of metals from non-aqueous solutions. *Electrochimica Acta*, 54(23):5307–5319, 2009.

[138] CU Chisholm. An initial study of deposition and codeposition of nickel and chromium from non-aqueous electrolytes. *Transactions of the IMF*, 47(1):134–141, 1969.

[139] DJ Levy and WR Momyer. Electrodeposition of chromium and nickel-chromium from amide solvents. *Journal of The Electrochemical Society*, 118(10):1563–1570, 1971.

[140] Shoba Jayakrishnan, Malathy Pushpavanam, and BA Shenoi. Electrodeposition from organic solutions of metals that are difficult to deposit from aqueous solutions. *Surface Technology*, 13(3):225–240, 1981.

[141] Nguyen Van Phuong, Sik Chol Kwon, Joo Yul Lee, Jun Ho Lee, and Kyu Hwan Lee. The effects of ph and polyethylene glycol on the cr (iii) solution chemistry and electrodeposition of chromium. *Surface and Coatings Technology*, 206(21):4349–4355, 2012.

[142] Enrico Bertero, Cristina V Manzano, Gerhard Bürki, and Laetitia Philippe. Stainless steel-like fecrni nanostructures via electrodeposition into aao templates using a mixed-solvent cr (iii)-based electrolyte. *Materials & Design*, page 108559, 2020.

[143] S Surviliene, A Češūnienė, A Selskis, and R Butkienė. Effect of cr (iii)+ ni (ii) solution chemistry on electrodeposition of crni alloys from aqueous oxalate and glycine baths. *Transactions of the IMF*, 91(1):24–31, 2013.

[144] Baosong Li, An Lin, Xu Wu, Yeming Zhang, and Fuxing Gan. Electrodeposition and characterization of fe–cr–p amorphous alloys from trivalent chromium sulfate electrolyte. *Journal of Alloys and Compounds*, 453(1-2):93–101, 2008.

[145] JianBin Zhang, PengYan Zhang, Kai Ma, Fang Han, GuoHua Chen, and XiongHui Wei. Hydrogen bonding interactions between ethylene glycol and water: density, excess molar volume, and spectral study. *Science in China Series B: Chemistry*, 51(5):420–426, 2008.

[146] Homer B Klonis and Edward L King. Kinetic and equilibrium studies of ethylene glycol-chromium (iii) species in acidic ethylene glycol-water solutions. *Inorganic Chemistry*, 11(12):2933–2938, 1972.

[147] Jacques Buffle, Zeshi Zhang, and Konstantin Startchev. Metal flux and dynamic speciation at (bio) interfaces. part i: critical evaluation and compilation of physicochemical parameters for complexes with simple ligands and fulvic/humic substances. *Environmental science & technology*, 41(22):7609–7620, 2007.

[148] Tohru Ishitani, Kaoru Umemura, Tsuyoshi Ohnishi, Toshie Yaguchi, and Takeo Kamino. Improvements in performance of focused ion beam cross-sectioning: aspects of ion-sample interaction. *Microscopy*, 53(5):443–449, 2004.

[149] Michael D Uchic and Dennis M Dimiduk. A methodology to investigate size scale effects in crystalline plasticity using uniaxial compression testing. *Materials Science and Engineering: A*, 400:268–278, 2005.

[150] Carmen M Lauener, L Petho, Ming Chen, Yuan Xiao, Johannes Michler, and Jeffrey M Wheeler. Fracture of silicon: Influence of rate, positioning accuracy, fib machining, and elevated temperatures on toughness measured by pillar indentation splitting. *Materials & Design*, 142:340–349, 2018.

[151] Ming Chen, Juri Wehrs, Johann Michler, and Jeffrey M Wheeler. High-temperature in situ deformation of gaas micro-pillars: Lithography versus fib machining. *Jom*, 68(11):2761–2767, 2016.

[152] Lucille A Giannuzzi et al. *Introduction to focused ion beams: instrumentation, theory, techniques and practice*. Springer Science & Business Media, 2004.

[153] Richard Lawrence Beauchamp. *Polarization characteristics of high-purity iron-rich iron-chromium-nickel alloys in sulfuric acid solutions*. PhD thesis, The Ohio State University, 1966.

[154] Daniel Khomskii. *Transition metal compounds*. Cambridge University Press, 2014.

[155] J Childress, Sy_Hwang Liou, and CL Chien. Ferromagnetism in metastable 304 stainless steel with bcc structure. *Journal of applied physics*, 64(10):6059–6061, 1988.

[156] YZ Xia, Hongbin Bei, YF Gao, Dhiraj Catoor, and Easo P George. Synthesis, characterization, and nanoindentation response of single crystal fe–cr–ni alloys with fcc and bcc structures. *Materials Science and Engineering: A*, 611:177–187, 2014.

[157] PL Ferrandini, CT Rios, AT Dutra, MA Jaime, PR Mei, and R Caram. Solute segregation and microstructure of directionally solidified austenitic stainless steel. *Materials Science and Engineering: A*, 435:139–144, 2006.

[158] Shigeo Fukumoto and Wilfried Kurz. The δ to γ transition in fe-cr-ni alloys during laser treatment. *ISIJ international*, 37(7):677–684, 1997.

[159] K Asami and K Hashimoto. The x-ray photo-electron spectra ofseveral oxides of iron and chromium. *Corrosion Science*, 17(7):559–570, 1977.

[160] NS McIntyre, S Sunder, DW Shoesmith, and FW Stanchell. Chemical information from xps—applications to the analysis of electrode surfaces. *Journal of Vacuum Science and Technology*, 18(3):714–721, 1981.

[161] Okio Nishimura, Katsumasa Yabe, and Masaya Iwaki. X-ray photoelectron spectroscopy studies of high-dose nitrogen ion implanted-chromium: a possibility of a standard material for chemical state analysis. *Journal of electron spectroscopy and related phenomena*, 49(3):335–342, 1989.

[162] Douglas Dalzell Perrin, Boyd Dempsey, and Eldon Perey Serjeant. *pKa prediction for organic acids and bases*, volume 1. Springer, 1981.

[163] Douglas Dalzell Perrin. Dissociation contants of inorganic acids and bases in aqueous solution. *Pure and Applied Chemistry*, 20(2):133–236, 1969.

[164] Eldon Percy Serjeant and Boyd Dempsey. *Ionisation constants of organic acids in aqueous solution*, volume 23. Pergamon, 1979.

[165] T Kiss, I Sovago, and A Gergely. Critical survey of stability constants of complexes of glycine. *Pure and applied chemistry*, 63(4):597–638, 1991.

[166] DD Perrin. The stability of complexes of ferric ion and amino-acids. *Journal of the Chemical Society*, pages 3125–3128, 1958.

[167] Robert M Smith and Arthur E Martell. Critical stability constants, enthalpies and entropies for the formation of metal complexes of aminopolycarboxylic acids and carboxylic acids. *Science of the total environment*, 64(1-2):125–147, 1987.

[168] J Szynkarczuk, I Drela, and J Kubicki. Electrochemical behaviour of chromium (iii) in the presence of formic acid—i. *Electrochimica Acta*, 34(3):399–403, 1989.

[169] Robert Martin Smith and Arthur Earl Martell. *Critical stability constants: inorganic complexes*, volume 4. Springer, 1976.

[170] Zhixiang Zeng, Yaling Sun, and Junyan Zhang. The electrochemical reduction mechanism of trivalent chromium in the presence of formic acid. *Electrochemistry Communications*, 11(2):331–334, 2009.

[171] Marie-Christine Fournier-Salaün and Philippe Salaün. Quantitative determination of hexavalent chromium in aqueous solutions by uv-vis spectrophotometer. *Central European Journal of Chemistry*, 5(4):1084–1093, 2007.

[172] S Goeringer, NR De Tacconi, CR Chenthamarakshan, and K Rajeshwar. Reduction of hexavalent chromium by copper. *Journal of applied electrochemistry*, 30(8):891–897, 2000.

[173] Metin Celebi, Mehmet Yurderi, Ahmet Bulut, Murat Kaya, and Mehmet Zahmakiran. Palladium nanoparticles supported on amine-functionalized sio2 for the catalytic hexavalent chromium reduction. *Applied Catalysis B: Environmental*, 180:53–64, 2016.

[174] Yan Gao and Yunhong Zhang. Formation and photochemical investigation of brown carbon by hydroxyacetone reactions with glycine and ammonium sulfate. *RSC advances*, 8(37):20719–20725, 2018.

Curriculum Vitae

Curriculum Vitae

Enrico Bertero

Genossenweg 3
3012 Bern
+41 77 927 82 29
enrico.bertero@outlook.com

"Success is not final, failure is not fatal: it is the courage to continue that counts."

Winston Churchill

Strengths

- Electrochemistry
- Materials characterisations
- Micro-nano fabrication
- Open minded; team worker
- Willing to travel; fluent in English

Key skills

- **Materials science/Nanotechnology**

  Fabrication: Deposition/Growing (Electrodeposition, Thermal oxidation, CVD, Thermal evaporation, Sputtering) Lithography (Optical, Electronic, Ionic), Etching (Wet and Dry); UV LIGA; Cleanroom facility

  Characterisation: SEM, FIB, Optical microscopy, XPS, XRD, XRF, APT, Tribometer, Profilometer, UV-vis spectrophotometer

  Electrochemistry: Fundamentals, Electrodeposition, (galvanostatic, potentiostatic, pulse-plating), Analytical methods (e.g. linear sweep voltammetry LSV, CV, chrono methods, RDE, titration)

- **Analog and Digital design:** Full-custom and Semi-custom design

Experience

2016-present

Empa (Thun) – EPFL (Lausanne)
Ph.D. on electrochemistry, materials science and technology
Early-Stage Researcher - EU Horizon 2020 (**SELECTA** ITN programme)

- 'Green' Cr(III)-based electrodeposition of stainless steel-like FeCrNi: synthesis, mechanisms, material properties of films and micro-nanocomponents for bio-medical applications
- Supervisors: Dr. L. Philippe (Empa), Dr. S. Mischler (EPFL)

03/2015-09/2015

CERN (Geneva)
Internship

- Design of the Power-On Reset circuit in the front-end ASIC (VFAT3) for the readout of GEMs detectors in the CMS at CERN
- Supervisors: Dr. P. Aspell (CERN), Prof. A. Koukab (EPFL), Prof. C.F. Pirri (POLITO)

06/2014-08/2014

INRIM (Turin - Italy)
Internship

- Realisation and characterisation of nanoSQUID based on Josephson junctions
- Supervisors: Dr. N. De Leo (INRIM), Prof. C.F. Pirri (POLITO)

2012

INPG (Grenoble - France)
Summer school in Micro-Nanotechnologies (6 ECTS)

- Lab work in Cleanroom (Solar cell processing)

Education

2013-2015

Master's Degree in Micro & Nanotechnology for ICTs (109/110)
Joint program POLITO (Italy), INPG (France), EPFL (Switzerland)

2009-2012

Bachelor's Degree in Physics Engineering (110/110)
Politecnico di Torino (Turin - Italy)

2004-2009

High-school Diploma in Computer Science (90/100) - IIS "G. Vallauri" (Italy)

Languages

Italian	Native language
English	Good (C1 – IELTS 7.0)
French	Elementary level (A1)
German	Elementary level (A1)

IT skills

MS Outlook / IE	very good user skills
MS Word	very good user skills
MS Excel	very good user skills
MS PowerPoint	very good user skills
Adobe Photoshop	good skills
Latex	good skills

CasaXPS	XPS fitting software
IVAS	APT software
Hydra-Medusa	speciation software
Comsol	multi-physics simulation software

Programming languages C/C++, Visual Basic

Extracurricular activities

Volunteer	EXPO 2015 - EU pavilion
Sports/Interests	football/swimming/running/hiking and keen reader

References

Dr. Laetitia Philippe (Empa)
+41 58 765 6249
laetitia.philippe@empa.ch

Dr. Stefano Mischler (EPFL)
+41 21 693 29 54
stefano.mischler@epfl.ch

Research

Publications

E. Bertero et al., Stainless steel-like FeCrNi nanostructures via electrodeposition into AAO templates using a mixed-solvent Cr(III)-based electrolyte, Materials & Design, 2020, **190**, 108559.

E. Bertero et al., 'Green' Cr(III)-glycine electrolyte for the production of FeCrNi coatings: electrodeposition mechanisms and role of by-products in terms of coating composition and microstructure, RSC Advances, 2019, **9**, 25762–25775.

E. Bertero et al., Electrodeposition of amorphous Fe-Cr-Ni stainless steel alloy with high corrosion resistance, low cytotoxicity and soft magnetic properties, Surface & Coatings Technology, 2018, **349**, 745–751.

Disseminations

Conferences

- Oral, ISE 70th Annual Meeting 2019, FeCrNi stainless-steel electrodeposition of coatings and micro-nano components from a 'green' Cr(III)-based mixed solvent electrolyte, Durban, South Africa (04-09 August 2019)
- Oral, SMT33, Electrodeposited FeCrNi stainless steel-like films from a 'green' Cr(III)-based electrolyte: material properties overview and investigation of impurities' incorporation, Naples, Italy (26-28 June 2019)
- Oral, EUROCORR2018, Electrodeposited FeCrNi stainless steel-like films: influence of impurities and microstructure on corrosion resistance, Krakow, Poland (09-13 September 2018)
- Oral, EMRS Spring Meeting 2018, Soft-magnetic electrodeposited FeCrNi stainless steel-like films with high corrosion resistance and low cytotoxicity, Strasbourg, France (18-22 June 2018)

EPFL / EMPA

- Course, CCMX Advanced Course "Inorganic particle synthesis by precipitation: from nanoparticles to self-organised mesocrystals and from theory to practice", EPFL, Switzerland (1 ECTS) (25-27 March 2018)
- Course, CCMX Winter school "Surface science: fundamentals, properties and selected applications", Kandersteg, Switzerland (2 ECTS) (27 January - 1 February 2019)
- Course, CCMX ScopeM Advanced Course "Combining structural & analytical investigations of matter at the micro-, nano- and atomic scale", ETH Zurich, Switzerland (2 ECTS) (5-8 November 2018)
- Course, e-MINDS COST action MP1407 "Electrochemical processing methodologies and corrosion protection for device and system miniaturisation", Siófok, Hungary (26-30 March 2018)
- Poster, EMPA PhD Symposium 2017 "Standing on the shoulder of giants", EMPA Dübendorf, Switzerland (13 November 2017)
- Course, Metrohm "Electrochemistry in corrosion research", Zofingen, Switzerland (1 ECTS) (7-9 November 2017)
- Course, CCMX Winter school "Additive manufacturing of metals and the material science behind it", Kandersteg, Switzerland (2 ECTS) (29 January - 3 February 2017)
- Poster, EMPA PhD Symposium 2017 "Decipher Science", EMPA Dübendorf, Switzerland (14 November 2016)
- Course, Electrochemistry for materials technology, EPFL, Switzerland (2 ECTS) (Winter semester 2016)
- Course, Tribology, EPFL, Switzerland (2 ECTS) (Winter semester 2016)
- Seminars, Advances in Materials, EPFL, Switzerland (Winter semester 2016)

EU Horizon 2020 (**SELECTA** ITN programme)

- Oral, Winter School "Gateway to industry: from materials to devices. Practical aspects", University of Cambridge, Cambridge, UK (4 ECTS) (7-12 January 2018)
- Poster, Summer School "Gateway to academics: materials modelling for target applications", University of Ioannina, Ioannina, Greece (5 ECTS) (3-7 September 2017)
- Oral, Mid-term review meeting and Workshop "Bridging innovation and entrepreneurship with sustainable materials development", Chalmers University of Technology, Goteborg, Sweden (4 ECTS) (5-9 December 2016)
- Oral, Workshop "Micro and nano-electrodeposition for MEMS/NEMS and micro/nano-robotic platforms. Overview of lithography methods. Impact to society", Happy Plating, Wiener Neustadt, Austria (3 ECTS) (29-31 August 2016)

International framework

EU Horizon 2020 (**SELECTA** ITN programme)

- Secondment, Magnetic measurements by VSM and elemental analysis by XPS of FeCrNi electrodeposited coatings, Autonomous University of Barcelona, Bellaterra, Spain (8 May - 2 July 2017)
- Secondment, Tribology measurements in dry friction condition on FeCrNi electrodeposited films, Vilnius University, Vilnius, Lithuania (14-30 October 2016)